Title
Combining theory and experiment in Pt-based catalysts design for energy conversion

Author
Huang, Jin

Publication Date
2021

Peer reviewed|Thesis/dissertation

UNIVERSITY OF CALIFORNIA

Los Angeles

Combining theory and experiment in Pt-based catalysts design for energy conversion

A dissertation submitted in partial satisfaction of the requirements

for the degree Doctor of Philosophy in Materials Science and Engineering

By

Jin Huang

2021

ABSTRACT OF THE DISSERTATION

Combining theory and experiment in Pt-based catalysts design for energy conversion

by

Jin Huang

Doctor of Philosophy in Materials Science and Engineering

University of California, Los Angeles, 2021

Professor Yu Huang, Chair

Energy crisis and climate change are the imminent challenges faced by mankind that demand instant solutions in replacing fossil fuels with alternative clean energy sources. To meet this demand, the hydrogen fuel cell industry has witnessed tremendous growth within the past decade. However, the broad dissemination of proton-exchange membrane fuel cells (PEMFCs) is still limited by the high cost originated from the high loading of platinum-group metals (PGM) based catalysts to accelerate the sluggish oxygen reduction reaction (ORR) at the cathode. Therefore, it is central to design high-performance ORR catalysts and validate their performance in the membrane electrode assembly (MEA).

In the first chapter of my dissertation, by combining theoretical modeling and experimental observations, we developed a binary experimental descriptor (BED) that directly correlates with the calculated oxygen binding energy ΔE_O on Pt-alloy catalyst surface. The BED captures both the strain and Pt-transition metal coupling contributions based on experimental parameters extracted

from X-ray absorption spectroscopy. This leads to an experimentally validated Sabatier plot wherein the BED can be used to predict not only the catalytic activity but also the stability of a wide range of Pt-alloy ORR catalysts. Based on the BED, we further designed an ORR catalyst wherein high activity and stability are simultaneously achieved.

The second chapter is an extension of the first chapter, in which I demonstrated that tetrahedral PtCuNi catalysts, as an efficient multifunctional catalyst, did not only showed excellent ORR performance but also exhibited high methanol/ethanol oxidation reaction (MOR/EOR) performance, which can be potentially used in the direct methanol/ethanol fuel cells (DMFCs/DEFCs). By tailoring the surface composition, the optimal catalyst with a composition of $Pt_{56}Cu_{28}Ni_{16}$ showed a MOR and EOR specific activity (SA) of 14.0 ± 1.0 mA/cm^2 and 11.2 ± 1.0 mA/cm^2, respectively; and mass activity (MA) of 7.0 ± 0.5A/mg$_{Pt}$ and 5.6 ± 0.6 A/mg$_{Pt}$ for the MOR and EOR, respectively.

In the third chapter, I applied some highly promising ORR catalysts in MEA. In specific, I developed an ultralow Pt loading (total loading of 0.072 mg$_{Pt}$/cm^2) and high-performance MEA using ultrathin platinum-cobalt nanowires (PtCoNWs) as cathode catalysts. The PtCoNWs showed a high ECSA of 73.2 m^2/g$_{Pt}$ and achieved an unprecedented MA of 1.06 ± 0.14 A/mg$_{Pt}$ [0.9 $V_{iR\text{-}free}$] at the beginning of life (BOL) stage in MEA. This MA is 3.3 times that of the commercial Pt/C (0.32 A/mg$_{Pt}$) and far surpasses the Department of Energy (DOE) 2020 target (0.44 A/mg$_{PGM}$). The PtCoNWs reached a peak power density of 1016 mW/cm^2, outperforming the PtNWs (830 mW/cm^2) and Pt/C (773 mW/cm^2) with comparable Pt loading. After the AST, the PtCoNWs showed a respectable end of life (EOL) MA of 0.45 A/mg$_{Pt}$, remaining above the DOE 2020 BOL target.

In the last chapter, I tried to tailor the interfacial properties to further enhance the surface microkinetic. In brief, I developed a facile and controllable molecular surface

modification approach using dimethylformamide (DMF) to successfully improve the ORR performance of Pt-based catalysts. Significantly, our molecular dynamics (MD) simulations elucidated that DMF can disrupt interfacial water hydrogen-bonding networks, therefore allowing accelerated water exchange kinetics, facile O_2 transport towards Pt surface, increased interfacial oxygen concentration, and adsorption time (around twice compared to pure Pt(111) surface), justifying enhanced ORR activity. We further applied this approach to a model Pt-alloy catalysts (PtCuNi), which achieved an unprecedented SA of 21.8 ± 2.1 mA/cm^2 at 0.9 V versus the reversible hydrogen electrode (RHE), about 2.65 times improvement comparing to original PtCuNi catalysts, and nearly double previously reported the best value, leading to an ultrahigh MA of 10.7 ± 1.1 A/mg_{Pt}. Importantly, after 20,000 cycles of accelerated degradation tests (ADT), surface-modified PtCuNi showed even better SA and MA than the initial performance of original PtCuNi, suggesting the surface modification can also considerably extend the lifetime of the catalyst.

The dissertation of Jin Huang is approved.

Bruce Dunn

Jaime Marian

Philippe Sautet

Yu Huang, Committee Chair

University of California, Los Angeles

2021

Dedicated to my mother Chuntao Qiu

for her unconditional and unfailing love.

Table of Contents

List of Figures, Schemes, and Tables

Acknowledgments

The Ph.D. adventure at UCLA cannot be more challenging to me. But I am so lucky to have lots of people who helped me get through it. First and foremost, I would like to acknowledge my mentor, Prof. Yu Huang, for her great help and patient instructions throughout my Ph.D. career. As a talented scientist, her rigorous attitude towards science and the strict requirement to each research project benefit me a lot. In addition, she is a super supportive mentor who cares about not only my career development but also my Ph.D. life when I was down. It is her encouragement and supports that make me decide to pursue my future career in academia. She will always be a role model to me.

Secondly, I would like to thank my committee members, Prof. Bruce Dunn, Prof. Jaime Marian, and Prof. Philippe Sautet for their help on my Ph.D. qualification exam and final dissertation. I would also greatly thank Prof. Marian for choosing me as his TA, where I gained a lot of teaching experience. I would also like to thank Prof. Xiangfeng Duan who provided keen insights and wonderful inspirations to me and helped me solved scientific problems. I really enjoyed discussing with him.

Moreover, I would like to thank my collaborators Dr. Qingying Jia from Northeastern University, Dr. Alessandro Fortunelli and his colleagues Dr. Luca Sementa and Dr. Giovanni Barcaro from Italian national research council, Prof. William Andrew Goddard III from California Institute of Technology, Prof. Hendrik Heinz, and his postdoc Dr. Cheng Zhu from the University of Colorado Boulder, and Dr. Mingjie Xu from the University of California, Irvine. I really enjoyed working with these professional and talented scientists worldwide. I would also like to thank my colleagues whom I worked with. First, I would like to thank Dr. Mufan Li who instructed me on lots of experiments and taught me a lot about Ph. D. career when I just entered graduate school. Second, I would like to thank Bosi Peng, Zeyan Liu, Yang Liu for close collaboration on several

of my projects. Finally, I would like to thank Dr. Zipeng Zhao, Dr. Enbo Zhu, Dr. Chengzhang Wan, Dr. Zhihong Huang, Dr. Zhaoyang Lin, Dr. Sung-joon Lee, Dr. Chungsuk Choi, Dr. Michelle Flores, Dr. Yun-Chiao Huang, Dr. Huiying Shiu, Dr. Hao Wu. Dr. Chen Wang, Dr, Mingning Ding, Dr. Huilong Fei, Dr. Lele Peng, Haotian Liu, Peiqi Wang, Guangyan Zhong, Bocheng Cao, Jin Cai, Ao Zhang, and all other group members and collaborators.

I would also like to thank Prof. Rong Tu and Prof. Hong Li from Wuhan University of Technology, who helped me and cared for me during my Ph.D. career. They are also my undergraduate mentor who first encouraged me to pursue further study at UCLA.

Last but not the least, I would like to thank my mother for her unconditional and unfailing love. Without her support and faith in me, I would not be able to be there.

Chapter One is a version of [Submitted manuscript] Author list: Jin Huang, Luca Sementa, Zeyan Liu, Giovanni Barcaro, Miao Feng, Ershuai Liu, Li Jiao, Mingjie Xu, Denis Leshchev, Sungjoon Lee, Mufan Li, Chengzhang Wan, Enbo Zhu, Yang Liu, Bosi Peng, Xiangfeng Duan, William A. Goddard III, Alessandro Fortunelli, Qingying Jia, Yu Huang.

Chapter Two is a version of [*Nano Letters*, Jin Huang, Yang Liu, Mingjie Xu, Chengzhang Wan, Haotian Liu, Mufan Li, Zhihong Huang, Xiangfeng Duan, Xiaoqing Pan, and Yu Huang, 2019, 19, 8, 5431–5436. DOI: 10.1021/acs.nanolett.9b01937.

Chapter Three is a version of [Submitted manuscript] Author list: Jin Huang, Bosi Peng, Thomas Stracensky, Zeyan Liu, Ao Zhang, Mingjie Xu, Yang Liu, Zipeng Zhao, Xiangfeng Duan, Qingying Jia, and Yu Huang.

Chapter Four is a version of [manuscript under preparation]

VITA

Education

2016 B.Eng. in Inorganic Non-Metallic Materials Engineering, Wuhan University of Technology, Wuhan, China

Honor

2016 UCLA Departmental Fellowship

2020 Dissertation Year Fellowship

Selected Publications (7 out of 15)

1. **Huang, J.**, Liu, Y., Xu, M., Wan, C., Liu, H., Li, M., Huang, Z., Duan, X., Pan, X.; Huang, Y., (2019). PtCuNi tetrahedra catalysts with tailored surfaces for efficient alcohol oxidation. *Nano Lett* 19, 5431-5436.

2. Zhang, C., **Huang, J.** (co-first), Tu, R., Zhang, S., Yang, M., Li, Q., Shi, J., Li, H., Zhang, L., Goto, T., et al., (2018). Transfer-free growth of graphene on Al2O3 (0001) using a three-step method. *Carbon* 131, 10-17.

3. Lee, S.-J., Lin, Z., Huang, J., Choi, C. S., Chen, P., Liu, Y., Guo, J., Jia, C., Wang, Y., Wang, L., et al., (2020). Programmable devices based on reversible solid-state doping of two-dimensional semiconductors with superionic silver iodide. *Nat. Electron.* 3, 630-637.

4. Li, M., Duanmu, K., Wan, C., Cheng, T., Zhang, L., Dai, S., Chen, W., Zhao, Z., Li, P., Fei, H., et al., (2019). Single-atom tailoring of platinum nanocatalysts for high-performance multifunctional electrocatalysis. *Nat. Catal.* 2, 495-503.

5. Zhao, Z., Liu, H., Gao, W., Xue, W., Liu, Z., Huang, J., Pan, X.; Huang, Y., (2018). Surface-engineered PtNi-O nanostructure with record-high performance for electrocatalytic hydrogen evolution reaction. *J. Am. Chem. Soc.* 140, 9046-9050.

6. Zhao, Z., Chen, C., Liu, Z., Huang, J., Wu, M., Liu, H., Li, Y.; Huang, Y., (2019). Pt-based nanocrystal for electrocatalytic oxygen reduction. *Adv. Mater.* 31, 1808115.

7. Zhu, E., Yan, X., Wang, S., Xu, M., Wang, C., Liu, H., Huang, J., Xue, W., Cai, J., Heinz, H., et al., (2019). Peptide-assisted 2-D assembly toward free-floating ultrathin platinum nanoplates as effective electrocatalysts. *Nano Lett.* 19, 3730-3736.

Chapter 1. Introduction

1.1 Catalysis for energy conversion and fuel cell

Energy crisis and climate change are the imminent challenges faced by mankind that demand instant solutions in replacing fossil fuels with alternative clean energy sources. The development of renewable energy has provided a huge potential to address the challenges. For the past decade, we have seen the dropping price of renewable energy. For example, the average cost is only 4 cents per kWh for wind and 3.4 cents per kWh for solar photovoltaics[1]. This attracting renewable energy is a game-changer to sustainable energy future. To achieve a sustainable energy system, it is highly desirable to store or convert excessive electricity[2]. In addition to storing electricity in the batteries, converting them into chemicals including hydrogen, hydrocarbon product, and ammonia provides more diverse pathways, which can be used in different sectors. Among miscellaneous energy conversion applications, proton-exchange membrane fuel cells (PEMFCs) represent an attractive and sustainable power generation technology in automotive applications with zero emission[3,4]. Recently, Toyota has released the second generation of Toyota Mirai which can achieve a maximum driving mileage of 402 miles per fill. Compared to current battery electrical vehicles (BEVs), PEMFC vehicles show considerable advantage with shorter refuel time and longer driving range, which is due to the intrinsic high specific energy of hydrogen as the energy storage medium[4]. Besides, with higher specific energy, the vehicle weight will not increase with miles. Fuel cell is also environmentally friendly because it used a solid electrolyte and catalysts inside can be easily recycled.

Hydrogen fuel cell industry has witnessed tremendous growth within the past decade. As illustrated in Figure 1.1, hydrogen is oxidized at the anode, and protons transport through the proton-exchange membrane, react with oxygen to form water, thus generate electricity. However,

oxygen reduction reaction (ORR), as the rate-determining step (RDS), significantly slows down the overall reaction kinetics. Therefore, a large amount of precious platinum-group metals (PGM) based catalysts are needed to accelerate sluggish ORR, which limits the broad dissemination of PEMFCs. To date, Pt-based catalysts account for more than 40% cost of fuel cell stacks[5]. To this end, it is central to improve the mass activity (MA) of Pt (the catalytic activity per unit mass of Pt).

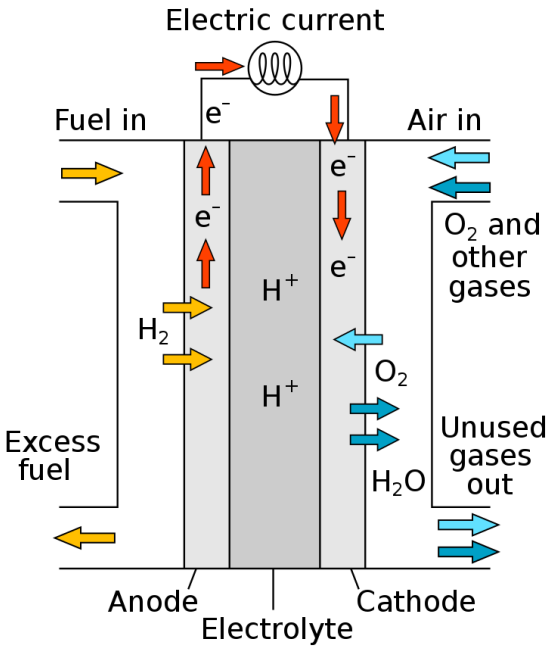

Figure 1.1. The schematic diagram and working principal of proton-exchange membrane fuel cells (PEMFCs). Adapted from https://en.wikipedia.org/wiki/Fuel_cell.

1.2 Oxygen reduction reaction (ORR)

Fundamentally, MA is the product of the electrochemically active surface area (ECSA) that is directly related to nanostructures and specific activity (SA) that represents the intrinsic

activity. The ECSA of catalysts is related to the nanostructures and morphologies. While the intrinsic/specific activity (SA) of catalysts is related to the reaction barrier of each reaction step. According to the associative mechanism (Figure 1.2) and the scaling relation[6], the binding energy of OH* and OOH* are all linear to that of the O*, which leads to the final "volcano plot" (Figure 1.3) with the x-axis as the O* binding energy and y-axis as the activity[7,8]. Furthermore, it has been proposed that the OOH* formation or the O_2* dissociation is the RDS for the right-slope catalysts, while the OH* desorption and further water formation is the RDS for the left-slope catalysts. For example, pure Pt binds O* too strong, which leads to sluggish OH* desorption.

Alloying Pt with transition metal M (M = Ni, Co, Fe, Cu, etc.) can induce strain effect[9] and ligand effect[10,11]. Both can lower the d-band center, thereby modulation the O binding energy and improve the ORR kinetics. Alternatively, tailoring the average coordination number can also modulate the O binding energy, achieving better activity for specific concave sites[12,13]. The above effects provide guidance to the ORR catalyst design.

$$O_2 + * \longrightarrow O_2*$$
$$O_2* + H^+ + e^- \longrightarrow OOH*$$
$$OOH* + H^+ + e^- \longrightarrow H_2O + O*$$
$$O* + H^+ + e^- \longrightarrow OH*$$
$$OH* + H^+ + e^- \longrightarrow H_2O + *$$

Figure 1.2. ORR associative mechanism, *represents the active site at the metal surface.

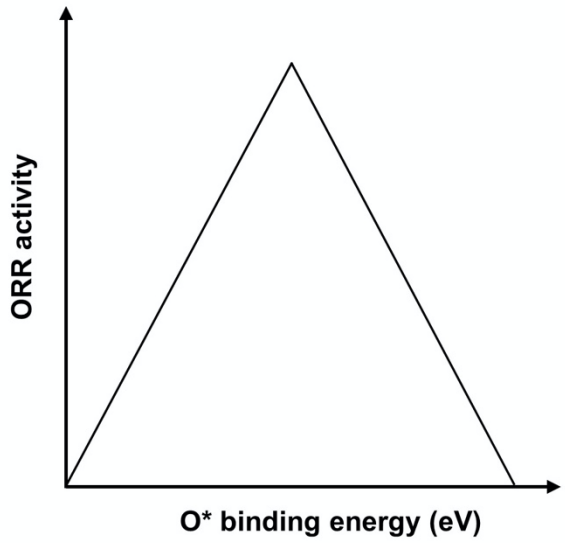

Figure 1.3. Illustration of ORR volcano plot, showing that the O* binding energy should be neither too strong nor too weak.

1.3 Direct methanol/ethanol fuel cells and relevant reactions

In addition to PEMFCs, direct methanol/ethanol fuel cells (DMFCs/DEFCs)[14] are also of great significance among energy conversion devices. Compared with hydrogen-powered fuel cells, DMFCs/DEFCs use cheaper and more available fuels that can be generated from biomass, which are of the higher energy density per volume as well as better stability.

Although acid electrolyte represents the most prevalent working electrolyte for the hydrogen fuel cells due to the well-developed proton exchange membrane, the acid-based DMFCs/DEFCs are often plagued with methanol/ethanol crossover, which can seriously poison platinum-based catalyst that is necessary for the cathodic ORR in the acidic conditions[15]. Thanks to newly developed anion-exchange membrane[16-18], using anti-poisoning non-platinum group metal (non-PGM) catalysts for cathodic ORR reaction[19,20] and operating fuel cells at high temperature are possible[18]. However, the anodic methanol oxidation reaction (MOR) and ethanol

oxidation reaction (EOR) are the rate-determining steps, which also required Pt-based catalysts to speed up the reaction. In my research, I also tried to explore the MOR/EOR performance for those highly promising Pt-based nanocatalysts.

1.4 References

1. Lazard. <https://www.lazard.com/perspective/levelized-cost-of-energy-and-levelized-cost-of-storage-2020/> (2020).

2. Seh, Z. W. *et al.* Combining theory and experiment in electrocatalysis: Insights into materials design. *Science* **355**, eaad4998 (2017).

3. Kodama, K., Nagai, T., Kuwaki, A., Jinnouchi, R. & Morimoto, Y. Challenges in applying highly active Pt-based nanostructured catalysts for oxygen reduction reactions to fuel cell vehicles. *Nat. Nanotechnol.* **16**, 140-147 (2021).

4. Fan, J. *et al.* Bridging the gap between highly active oxygen reduction reaction catalysts and effective catalyst layers for proton exchange membrane fuel cells. *Nat. Energy* **6**, 475-486 (2021).

5. Kongkanand, A. & Mathias, M. F. The priority and challenge of high-power performance of low-platinum proton-exchange membrane fuel cells. *J. Phys. Chem. Lett.* **7**, 1127-1137 (2016).

6. Stephens, I. E. L., Bondarenko, A. S., Grønbjerg, U., Rossmeisl, J. & Chorkendorff, I. Understanding the electrocatalysis of oxygen reduction on platinum and its alloys. *Energy Environ. Sci.* **5**, 6744-6762 (2012).

7. Nørskov, J. K. *et al.* Origin of the overpotential for oxygen reduction at a fuel-cell cathode. *J. Phys. Chem. B* **108**, 17886-17892 (2004).

8. Greeley, J. *et al.* Alloys of platinum and early transition metals as oxygen reduction electrocatalysts. *Nat. Chem.* **1**, 552-556 (2009).

9. Escudero-Escribano, M. *et al.* Tuning the activity of Pt alloy electrocatalysts by means of the lanthanide contraction. *Science* **352**, 73-76 (2016).

10. Kitchin, J. R., Nørskov, J. K., Barteau, M. A. & Chen, J. G. Role of strain and ligand effects in the modification of the electronic and chemical properties of bimetallic surfaces. *Phys. Rev. Lett.* **93**, 156801 (2004).

11. Stamenkovic, V. R. *et al.* Improved oxygen reduction activity on $Pt_3Ni(111)$ via increased surface site availability. *Science* **315**, 493-497 (2007).

12. Calle-Vallejo, F. *et al.* Why conclusions from platinum model surfaces do not necessarily lead to enhanced nanoparticle catalysts for the oxygen reduction reaction. *Chem. Sci.* **8**, 2283-2289 (2017).

13. Calle-Vallejo, F. *et al.* Finding optimal surface sites on heterogeneous catalysts by counting nearest neighbors. *Science* **350**, 185-189 (2015).

14. Li, X. L. & Faghri, A. Review and advances of direct methanol fuel cells (DMFCs) part I: Design, fabrication, and testing with high concentration methanol solutions. *J. Power Sources* **226**, 223-240 (2013).

15. Badwal, S. P. S., Giddey, S., Kulkarni, A., Goel, J. & Basu, S. Direct ethanol fuel cells for transport and stationary applications - A comprehensive review. *Appl. Energy* **145**, 80-103 (2015).

16. Katzfuss, A., Gogel, V., Jorissen, L. & Kerres, J. The application of covalently cross-linked BrPPO as AEM in alkaline DMFC. *J. Membr. Sci.* **425**, 131-140 (2013).

17. Varcoe, J. R. *et al.* Anion-exchange membranes in electrochemical energy systems. *Energy Environ. Sci.* **7**, 3135-3191 (2014).

18. Wang, J. H. *et al.* Poly(aryl piperidinium) membranes and ionomers for hydroxide exchange membrane fuel cells. *Nat. Energy* **4**, 392-398 (2019).

19. Bezerra, C. W. B. *et al.* A review of Fe-N/C and Co-N/C catalysts for the oxygen reduction reaction. *Electrochim. Acta* **53**, 4937-4951 (2008).

20. Yang, L. *et al.* Unveiling the high-activity origin of single-atom iron catalysts for oxygen reduction reaction. *Proc. Natl. Acad. Sci. U. S. A.* **115**, 6626-6631 (2018).

Chapter 2. Development of binary experimental descriptor and experimental Sabatier plot

2.1 Introduction

While the theoretical descriptor, ΔE_O, has been widely acknowledged as a useful descriptor at the QM level, its experimental analogue has met very limited success, which severely limits the efficient development of high-performing Pt-based nanocatalysts. For example, strain in Pt-alloys has been routinely adopted as a plausible experimental descriptor for ORR activity[1-3]. However, strain alone is insufficient to predict the ORR activity of Pt-alloy nanocatalysts[4,5]. Meanwhile, the ligand effect[6] and local atomic coordination[7], which describes the contributions from both composition and atomic coordination distribution to ΔE_O and hence Pt-alloy to catalytic activities, have rarely been investigated or accounted for experimentally as they are almost unattainable in experiments. Moreover, the ever-evolving structure and composition of catalysts during catalysis[8,9] adds to the challenge of identifying simple experimentally tangible descriptors that can capture the key contributing factors predicted in theory[6,10,11]. These persisting issues have plagued the development of high-performing ORR catalysts and signify the need for an experimental tangible descriptor to predict both the activity and stability of these catalysts.

To date, the developments of highly active and stable Pt-alloy nanocatalysts have largely relied on anecdotal discoveries[12-14]. While oxygen binding energy ΔE_O (oxygen binding energy to the catalyst surface) has been frequently used as a theoretical descriptor for predicting the activity, there is not known descriptor for predicting the durability of the catalysts. For the rapid development of ORR catalysts with simultaneously high activity and stability, it is essential to develop experimental descriptors to guide the practical catalyst design. The theoretical descriptor, ΔE_O has been widely acknowledged as a useful descriptor at the quantum mechanics (QM) level, however, its experimental analogue has met very limited success despite intensive efforts over the

past several decades, which has practically limited the rapid development of high-performing ORR catalysts.

We now report the development of a binary experimental descriptor (BED) that correlates directly with calculated ΔE_o on Pt-alloy catalysts and demonstrate for the first time that an experimental Sabatier plot can be used to predict both the activity and stability of the ORR catalysts. In brief, based on the design and experimental and theoretical analyses of the atomic structure-function relation of two classes of PtNi catalysts, we formulated an experimental descriptor BED that fully accounts for the experimentally observed ORR activities of the Pt-alloys based on the experimentally tangible value [-0.13Strain (%) + 0.1ΔAF]. Specifically, strain is represented by the average Pt-Pt bond length from extended X-ray absorption fine structure (EXAFS), and the asymmetry factor (AF) in the Pt-L_3 X-ray absorption near edge structure (XANES) spectra of Pt-alloys represents Pt-transition metal coupling effect from the local atomic mixing and coordination. Our computational studies confirmed that this BED can accurately reflect calculated ΔE_o on the Pt-alloy catalyst surface, leading to an identify function with high fidelity. Based on the new BED, we designed a PtNiCo catalyst located at the top right of the experimental Sabatier plot, which can simultaneously deliver a superior SA and robust stability. Specifically, the designed PtNiCo catalysts demonstrated high SA of 10.7 ± 1.4 mA/cm^2 with only 8% loss of ECSA and 12% loss of MA after 20,000 cycles of accelerated degradation tests (ADT), filling in the blank in the ORR catalyst design space. More importantly, high catalytic activity and stability were also validated in the membrane assembled electrodes (MEA) representing applicability in practical fuel cells.

2.2 Methods

2.2.1 Experimental methods

Materials and chemicals

Platinum(II) acetylacetonate ($Pt(acac)_2$, 97%), nickel(II) acetylacetonate ($Ni(acac)_2$, 95%), cobalt (II) acetylacetonate ($Co(acac)_2$, 97%), copper (II) acetylacetonate ($Cu(acac)_2$, 97%), perchloric acid ($HClO_4$, 70%, PPT Grade), glucose, benzoic acid (C_6H_5COOH, ≥99.5%), oleylamine [OAm; $CH_3(CH_2)_7CH{=}CH(CH_2)_7CH_2NH_2$, >70%], 1-octadecene [ODE; $CH_2{=}CH(CH_2)_{15}CH_3$; technical grade, >90%], 5 wt % Nafion were all purchased from Sigma-Aldrich. Commercial Pt/C catalyst (20 wt% Pt, and particle size 2 to 5 nm), Pt/C catalyst (10%), and Pt/C catalyst (40%) were purchased from Alfa Aesar. N, N-dimethylformamide (DMF, ≥99.8%), ethanol (200 proof), cyclohexane (C_6H_{12}; analytical reagent, >99.5%) were obtained from EMD Millipore and Decon. Acetone (≥99.5%) and isopropanol (≥99.5%) were purchased from Fisher Scientific. All reagents were used as received without further purification. Carbon black (Vulcan XC-72) was received from Carbot Corporation and annealed in 280 ℃ air before used. The deionized water (18 MΩ/cm) was obtained from an ultra-pure purification system (Milli-Q advantage A10).

Preparation of parent Pt-alloy (p-Pt-alloy) catalysts

In a typical synthesis of parent $Pt_{45}Ni_{55}$ catalysts (p-$Pt_{45}Ni_{55}$), In a typical synthesis, 10 mg of $Pt(acac)_2$, 20 mg of $Ni(acac)_2$, and 250 mg benzoic acid were added to a 10 mL of carbon black suspended DMF solution (total 30 mg carbon black) in a 25 mL glass vial. The vial was then capped and ultrasonic processed for 10 minutes, followed by heating with magnetic stirring in an oil bath at 160 ℃ for 12 hours. After the reaction, the vial was cooled down to room temperature, the p-$Pt_{45}Ni_{55}$ catalyst was obtained by centrifugation and washed with isopropanol/acetone

mixture several times. The resulting p-$Pt_{45}Ni_{55}$ catalysts were further dried in a vacuum dryer for future usage. The synthesis of p-$Pt_{41}Ni_{54}Co_5$ octahedra is similar to the synthesis of p-$Pt_{45}Ni_{55}$ catalysts, except for an additional 5 mg $Co(acac)_2$ precursor was added.

Preparation of slow-dealloyed Pt-alloy (sd-Pt-alloy) catalysts

First, 200 mg p-Pt-alloy catalysts were dissolved with 150 mL DMF in a 250 mL 3-neck flask and sonicated for 20 minutes. Then, the 3-neck flask with magnetic stirring was put into the oil bath and heated to 120 ℃. The solution was purged with air and refilled with DMF for maintaining a constant level of solution. After 1 to 7 days, the sample was collected by using a pipette and centrifugation and washed with isopropanol/acetone mixture several times. The resulting sd-Pt-alloy was further dried in a vacuum dryer for future usage.

Preparation of fast-dealloyed Pt-alloy (fd-Pt-alloy) catalysts

The preparation of fast dealloyed Pt-alloy catalysts (fd-Pt-alloy) was achieved by annealing parent Pt-alloy catalysts in the air at 120 ℃ for 2 hours to mimic the annealing condition of sd-Pt-alloy catalysts. Then, the annealed catalysts were dealloyed in 0.5 M H_2SO_4 at 80 °C for 2 hours. The sample was collected by centrifugation and then washed with deionized water several times till the pH is equal to neutral. The resulting fd-Pt-alloy catalysts were further dried in a vacuum dryer for future usage.

Preparation of tetrahedra PtCuNi (tetra-PtCuNi) catalysts

The synthesis of tetrahedra PtCuNi (tetra-PtCuNi) catalysts is based on a previous report[15]. In a typical preparation of tetra-$Pt_{77}Cu_{15}Ni_8$ catalysts, $Pt(acac)_2$ (20 mg), $Cu(acac)_2$ (6 mg), $Ni(acac)_2$ (6 mg), glucose (135 mg), OAm (3 ml), and ODE (2 ml) were added into a vial (volume, 35 ml). After the vial had been capped, the mixture was ultrasonicated for 1 hour. The resulting homogeneous mixture was then purged with carbon monoxide (CO) for 5 minutes and heated from

room temperature to 170 °C in 0.5 hours and kept at 170 °C for 12 hours in an oil bath with stirring. After cooling to room temperature, the colloidal products were collected by centrifugation and washed with cyclohexane/ethanol (v/v = 1:5) mixture two times. For the syntheses of tetra-$Pt_{65}Cu_{28}Ni_7$, all the conditions were similar to those of tetra-$Pt_{77}Cu_{15}Ni_8$ except by adding 12 mg $Ni(acac)_2$. The as-prepared tetra-PtCuNi catalysts were suspended in 20 mL cyclohexane/ethanol (v/v = 1:1) mixture. To load the sample onto carbon black, 20 mg of carbon black was added and sonicated for 2 hours. The resulting catalysts were collected by centrifugation and cleaned with cyclohexane/ethanol mixture, placed in an alumina boat, and annealed at 130 °C for 6 hours in Ar with a flow rate of 100 sccm in a home-build tube furnace to dry and get rid of the surfactant. The composition was determined by EDX after catalysts were activated.

Preparation of annealed p-Pt-alloy (p-Pt-alloy-AN) catalysts

The p-PtNi-AN and p-PtNiCo-AN catalysts were prepared by annealing the p-PtNi and p-PtNiCo catalysts in a homemade furnace at 700 °C for 2 hours with a mixture of gas flow (Ar : H2 = 300 sccm : 3 sccm).

Preparation of octahedral $Pt_{79}Ni_{15}Co_6$ (Oct-$Pt_{79}Ni_{15}Co_6$) catalysts

The synthesis of octahedral $Pt_{79}Ni_{15}Co_6$ (Oct-$Pt_{79}Ni_{15}Co_6$) catalysts is similar to the previous report[16]. In short, 10 mg of $Pt(acac)_2$, 5 mg of $Ni(acac)_2$, 5 mg of $Co(acac)_2$, and 65 mg benzoic acid were added to a 10 mL of carbon black suspended DMF solution (total 30 mg carbon black) in a 25 mL glass vial. The vial was then capped and ultrasonic processed for 20 minutes, followed by heating with magnetic stirring in an oil bath at 160 ℃ for 12 hours. After reaction, the vial was cooled down to room temperature. The Oct-$Pt_{79}Ni_{15}Co_6$ catalyst was obtained by centrifugation and washed with isopropanol/acetone mixture several times. The resulting catalyst was further dried in a vacuum dryer for future usage.

Structure and composition characterization

Powder X-ray diffraction (XRD) patterns were collected on a Panalytical X'Pert Pro X-ray Powder Diffractometer with Cu-Kα radiation. Low magnification Transmission electron microscopy (TEM) images were taken on a FEI T12 transmission electron microscope operated at 120 kV. High-resolution TEM images (HRTEM), energy-dispersive X-ray spectroscopy (EDX) line-scan file, and the high-angle annular dark-field scanning transmission electron microscope (HAADF-STEM) images were taken on JEM-ARM300F Grand ARM Transmission Electron Microscope operated at 300 kV. TEM samples were prepared by dropping ethanol dispersion of catalysts onto carbon-coated aluminum TEM grids. The Pt loading of catalysts was determined by the inductively coupled plasma atomic emission spectroscopy (ICP-AES). The Pt loading is determined before electrochemical measurement. The Pt loading is about 10.6 wt%. for p-Pt-alloys and about 9.5 wt% for sd-Pt-alloy and fd-Pt-alloys.

Electrochemical measurement

A three-electrode cell system was used to conduct all electrochemical tests. The working electrode was a glassy carbon rotating disk electrode (RDE) with a 0.196 cm^2 glassy carbon geometry area from Pine Instruments. The counter and reference electrodes are Pt wire and Ag/AgCl (1 M Cl^-), respectively. For activity measurement, Pt loadings were 7.85 $\mu g/cm^2$, 7.65 $\mu g/cm^2$, 5.65 $\mu g/cm^2$, 5.55 $\mu g/cm^2$ for p-$Pt_{45}Ni_{55}$, p-$Pt_{41}Ni_{54}Co_5$, sd-$Pt_{85}Ni_{15}$ and sd-$Pt_{84}Ni_{12}Co_4$ respectively. The Pt loading of fd-Pt-alloy and Pt/C catalysts were about 7.5 $\mu g/cm^2$ and 10 $\mu g/cm^2$, respectively. Cyclic voltammetry (CV) activations were performed in N_2-saturated 0.1 M $HClO_4$ electrolyte with a potential scan rate of 100 mV/s from 0.05 to 1.1 V vs. the reverse hydrogen electrode (RHE) until CV curves stabilized. ECSA determined by H_{upd} was calculated by integrating the hydrogen adsorption charge on the CV curve by taking a value of 210 $\mu C/cm^2$ for

the adsorption of a hydrogen monolayer. Double-layer correction was also applied. ORR was tested in an O_2-saturated 0.1 M $HClO_4$ electrolyte with a potential scan rate of 20 mV/s. The measurement temperature was set at 25 ℃ using a water bath 5-neck flask. The current density of the ORR polarization curves was iR-corrected. The ADT was performed at room temperature in O_2-saturated 0.1 M $HClO_4$ solutions by applying CV sweeps between 0.6 and 1.0 V versus RHE at a sweep rate of 100 mV/s.

Membrane electrode assembly (MEA) preparation and single fuel cell test

The single fuel cell performance of the catalysts as the cathode was tested at an 850e Fuel Cell Test System (scribner, USA). The MEA with an active area of 5.0 cm^2 were fabricated using the catalyst-coated membrane (CCM) method. The anode loading was set to be 0.025 mg_{Pt}/cm^2 (10% Pt/C, Alfa Aesar). Catalysts were incorporated into MEAs by direct spraying of a water/2-propanol based ink onto a Nafion HP membrane (from Fuel Cell Store) with desired loading (Cathode loading is 0.083 mg_{Pt}/cm^2). The mass activity was measured via measuring the current at 0.9 V (iR-free) under 150 kPa_{abs} H_2/O_2 (80°C, 100% RH, 835/2,000 sccm) with correction for measured H_2 crossover. The potential cycling accelerated stress tests (AST) were conducted by using the square wave method from 0.6 V to 0.95 V with 3 s hold time at each potential (150 kPa_{abs} H_2/N_2, 80°C, 100%RH, H_2/N_2 = 100/100 sccm).

X-ray absorption spectroscopy (XAS) data collection and analysis

The electrode inks for the XAS electrodes were composed of ethanol, 5 wt % Nafion solution, and catalyst powder. The ink was drop cast onto a carbon paper with a total catalyst loading of about 8 mg/cm^2. The ADT samples for XAS were cycled on the carbon paper for 20,000 cycles at room temperature in O_2-saturated 0.1 M $HClO_4$ solutions by applying CV sweep between 0.6 and 1.1 V versus RHE at a sweep rate of 100 mV/s. The XAS experiments were conducted at

room temperature in a previously described *in-situ* spectro-electrochemical half-cell in which a continuously O_2 purged 0.1 M $HClO_4$ aqueous solution was circulated[17], at the beamline ISS 6-BM and 8-ID in National Synchrotron Light Source II (NSLS-II) (Brookhaven National Laboratory, NY). Before transferred into the cell, the electrodes were conditioned in 0.1 M $HClO_4$ under vacuum for 40 minutes to remove surface oxides and contaminants. Potentiostatic control was maintained with an Autolab PGSTAT30 potentiostat (Metrohm USA, formerly Brinkman Instruments). Full range Pt L_3-edge, Co, Cu, and/or Ni K-edge spectra were taken at various static potentials along the anodic sweep of the CV. Data were collected on the same electrode in transmission mode at the Pt L_3-edge, and fluorescence mode at the Co, Ni, and Cu K-edge, with a Pt/Co/Ni/Cu reference foil positioned between the ionization chambers I2 and I3 as a reference. The voltage cycling limits were 0.05 to 1.00 V vs. RHE. Data collection was performed at the chosen potentials held during anodic sweeps. The electrode was fully cycled following each potential hold to clean the electrode surfaces after each potential hold. Typical experimental procedures were utilized with details provided in our previous work[18]. The data were processed and fitted using the Ifeffit−based Athena[19] and Artemis[20] programs. Scans were calibrated, aligned, and normalized with background removed using the IFEFFIT suite[21]. The χ(R) were modeled using single scattering paths calculated by FEFF6[22]. For convenience, examined catalysts were activated on the three-electrode system prior to XAS measurements.

Asymmetry factor (AF) descriptor

The asymmetry factor (AF) of the XANES peaks is calculated with the equation: AF = b/a, where:

b is the distance from the peak midpoint (perpendicularly from the peak highest point) to the trailing edge of the peak measured at 10% of peak height，

a is the distance from the leading edge of the peak to the peak midpoint.

The trailing edge is determined by taking the first derivative of the Pt L_3 XANES. For example, the trailing edge of the peak is chosen around 11576 eV for Pt/C and around 11577 eV for Pt-alloy catalysts, respectively. The corresponding intensity was then set as the peak bottom. The difference of the peak intensity and the above determined bottom intensity is the peak height. In the alloy case, we calculate the difference in AF with respect to pure Pt, i.e., Δ(asymmetry factor) of PtM: $\Delta AF = AF(PtM) - AF(Pt/C)$

The binary experimental descriptor (BED)

To quantitatively determine the relationship between ΔE_O and the binary experimental descriptor (BED) (i.e., to determine the relative weights in the combination of Strain (%) and ΔAF), we performed the linear fitting:

$$BED = A\big(Strain\ (\%)\big) + B(\Delta AF)$$

By fitting [$\Delta E_O^{(111)}$ - $\Delta E_O^{Pt(111)}$] with the BED enforcing the intercept (0, 0) and a one-to-one correspondence relationship, the optimal A and B are determined to be -0.13 and 0.1, respectively with high fidelity ($R^2 = 0.93$) and a low root-mean-square error (RMSE) of 0.03 eV (Fig. 2C), thus achieving a better fit than when using only the strain as a descriptor (fidelity of 0.82 and RMSE of 0.04 eV) (fig. S14).

So, our final binary descriptor is determined to be:

$$BED = [-0.13\big(Strain\ (\%)\big) + 0.1(\Delta AF)]$$

2.2.2 Computational methods

The XANES spectra were simulated by employing the FEFF9 code[22] which calculates the self-consistent multiple scattering from atomic targets whose scattering potential is obtained by overlapping free atom densities in the muffin tin approximation[23]. Using the FEFF9 code, we

calculated the Pt L_3-edge structure for several 147-atom cuboctahedral cluster models, both as averages over all atoms and simulated XANES spectra of individual Pt atoms are also reported.

Quantum-Mechanical (QM) density-functional theory (DFT) calculations were performed on PtNi clusters of up to 147 atoms in size. For each cluster model, full local geometry relaxation was performed starting from the geometry of Pt_{147}. We used the Quantum Espresso[24] suite of programs, the Perdew-Burke-Ernzerhof (PBE)[25] exchange-correlation functional and ultra-soft pseudopotentials[26]. Local geometry optimizations were performed spin unrestricted and employed the following numerical parameters: wave-function and charge-density cut-offs equal to 40 and 400 Ry, respectively, a simple cubic cell with side length of 20 a.u., a Gaussian smearing of the one-electron energy levels of 0.001 a.u., a convergence threshold for self-consistency equal to $0.5 \cdot 10^{-6}$ a.u., and a reciprocal space sampled at the Gamma point only. Geometries were considered to be converged when the forces on each atom became smaller than 0.001 a.u.

The models investigated in this work are based on a 147-atom cluster of cuboctahedral symmetry. Atoms in this cluster can be distinguished into 9 symmetry-equivalent groups or "orbits"[27]: (i) one atom at the centre, (ii) a first shell of 12 first-neighbours, (iii) 6 atoms on subsurface (100) facets, (iv) 24 atoms on subsurface (111) facets, (v) 12 atoms on subsurface vertexes, (vi) 8 atoms on (111) surface facets, (vii) 24 atoms on (100) surface facets, (viii) 48 atoms on surface edges, (ix) 12 atoms on surface vertexes. By differently distributing different numbers of Ni (or Co) atoms replacing Pt atoms in this cuboctahedral structural framework, after geometry relaxation we obtain clusters with varying composition and compositional order that model the stoichiometry and structural features of the different systems produced experimentally. We thus considered a pure-Pt Pt_{147}, two $Pt_{122}Ni_{25}$, one $Pt_{131}Ni_{16}$, one $Pt_{134}Ni_{13}$, one $Pt_{116}Ni_{31}$, and one $Pt_{122}Ni_{17}Co_8$ models. In detail: in the 'mixed' sd-$Pt_{122}Ni_{25}$, the 25 Ni atoms were distributed

in orbits (i) and (iv), therefore maximizing the number of Pt-Ni bonds. In the 'segregated' fd-$Pt_{122}Ni_{25}$, the same number of 25 Ni atoms were distributed in orbits (i), (ii) and (v). sd-$Pt_{122}Ni_{25}$ thus mimics an ordered arrangement of Ni in the cluster, as obtained via slow leaching together with atomic reordering of Ni into an energetically stable distribution, whereas fd-$Pt_{122}Ni_{25}$ mimics a more aggregated arrangement of Ni atoms in the structural framework, as obtained via fast leaching of the most peripheral Ni atoms.

By electrochemical ADT, further Ni is leached out of the clusters, that we model using two more clusters: in the 'mixed' sd-$Pt_{131}Ni_{16}$-ADT we started from sd-$Pt_{122}Ni_{25}$, depleted orbit (i) of Ni, and replaced one Ni atom with one Pt from each (111) sub-facet site i.e. orbit (iv) to obtain a still reasonably symmetric, strongly mixed and stable Ni distribution but a lower Ni content, while in the 'segregated' fd-$Pt_{134}Ni_{13}$-ADT we started from fd-$Pt_{122}Ni_{25}$ and depleted orbit (v) of Ni to obtain a strongly segregated and de-alloyed cluster. Finally, a sd-$Pt_{122}Ni_{17}Co_8$ model was built by replacing one Ni atom of sd-$Pt_{122}Ni_{25}$ with one Co from each subsurface (111) facet of orbit (iv) to obtain a cluster with the same number of dopant atoms as sd-$Pt_{122}Ni_{25}$ and fd-$Pt_{122}Ni_{25}$ for direct comparison as in the experimental particles: this cluster mimics a slow de-alloying process of a PtNiCo particle. For completeness, we also considered a $L1_0$-$Pt_{116}Ni_{31}$ cluster, in which the Ni atoms are distributed in the core according to a $L1_0$-bulk-like chemical ordering, i.e., with Pt and Ni alternating in (100) layers. Note that the stoichiometry of our cluster models tries to resemble the experimental one, given the constraints due to the smallness of our clusters. The geometry of these cluster models was fully relaxed at the DFT/PBE level, and then used to simulate XANES spectra with the FEFF9 code.

Finally, we calculated oxygen adsorption energies on various sites of the so-derived cluster models after full geometry relaxation as: $\Delta E_O = E(M_{147}\text{-}O) - E(M_{147}) - E(O_{gas\text{-}phase})$, where all

energies are taken at the corresponding equilibrium geometries. We considered the interaction of O adatoms both on the fcc(111) adsorption sites (as models of ORR mechanism to be related to ORR activity) and on vertex sites [as models of particle oxidation/degradation to be related to the stability of the clusters[28]]. In case of multiple possible adsorption sites inequivalent by symmetry, we took the average adsorption energy to build the plots.

In detail, the O-binding energy, ΔE_O, is calculated as:

$\Delta E_O = E(M_{147}\text{-}O) - E(M_{147}) - E(O_{gas\text{-}phase})$,

where M_{147} is the 147-atom Pt or Pt-alloy cluster model, $E(M_{147}\text{-}O)$ is the total energy of a cluster with O-binding on 147-atom Pt or 147-Pt-alloy cluster, $E(M_{147})$ is the total energy of the 147-atom Pt or 147-Pt-alloy cluster without adsorbates, $E(O_{gas\text{-}phase})$ is the total energy of an oxygen atom in the gas phase.

In the latter discussion, $\Delta E_O^{(111)}$ represents the average ΔE_O on the (111) sites of the 147-atom Pt-alloy cluster, $\Delta E_O^{Pt(111)}$ represents the average ΔE_O on the (111) site of the Pt_{147} cluster, $\Delta E_O^{(Vertex)}$ represents the ΔE_O on the vertex site of the 147-atom Pt-alloy cluster, $\Delta E_O^{Pt(Vertex)}$ represents the ΔE_O on the vertex site of the Pt_{147} cluster.

The mixing energy[27] of an A-B alloy is defined as:

$\Delta[N_A, N_B] = E_{alloy}[N_A, N_B] - N_A E_A[N]/N - N_B E_B[N]/N$

Where $E_{alloy}[N_A, N_B]$ is the energy of a nanoalloy cluster composed of N_A atoms of species A and N_B atoms of species B, $N = N_A + N_B$ is the total number of atoms in the cluster, $E_A[N]$ is the energy of a pure-A cluster of N atoms, $E_B[N]$ is the energy of a pure-B cluster of N atoms.

2.3 Results and discussion

Design and comparison of sd-PtNi and fd-PtNi catalysts

To deconvolute and understand the key experimental signatures leading to different activity and stability of Pt-alloy catalysts, we compare the catalysts with similar morphology and composition in order to discern the nuanced performance. We hence chose the concave octahedral PtNi catalysts with a commonly observed stable final composition of ca. $80\%_{atom}$ Pt and with a Pt-rich surface under electrochemical conditions[8,29,30]. We designed and compared the performance between the fast-dealloyed-PtNi octahedral catalysts obtained through aggressive acid dealloying of the PtNi octahedral catalysts, and the slow-dealloyed PtNi octahedral catalysts obtained through gradual dealloying in air-purged dimethylformamide (DMF). Both catalysts showed similar concaved octahedral morphology with similar composition after the electrochemical activation process (Figure 2.1a). To prepare the concave PtNi catalysts, the transition-metal-rich octahedral parent $Pt_{45}Ni_{55}$/C (p-$Pt_{45}Ni_{55}$) was first synthesized using a modified one-pot synthesis method reported previously[16]. The transmission electron microscopy (TEM) and high-angle annular dark-field scanning TEM (HAADF-STEM) images (Figure 2.1) of the p-$Pt_{45}Ni_{55}$ showed an octahedral shape with an average edge length of 7.0 ± 0.8 nm (Figure 2.2a) and an average lattice spacing of 0.212 nm according to the fast Fourier transform (FFT) diffraction pattern (inset of Figure 2.1c) and X-ray diffraction (XRD) results (Figure 2.3a). The p-$Pt_{45}Ni_{55}$ was then subject to either a slow-dealloying or a fast-dealloying process to obtain the slow-dealloyed-PtNi (sd-PtNi) or the fast-dealloyed-PtNi (fd-PtNi) catalysts, respectively. Both sd-PtNi and fd-PtNi showed a highly concaved morphology (Figure 2.1b, d) with a composition around $Pt_{85}Ni_{15}$ (Figures 2.4, 5b).

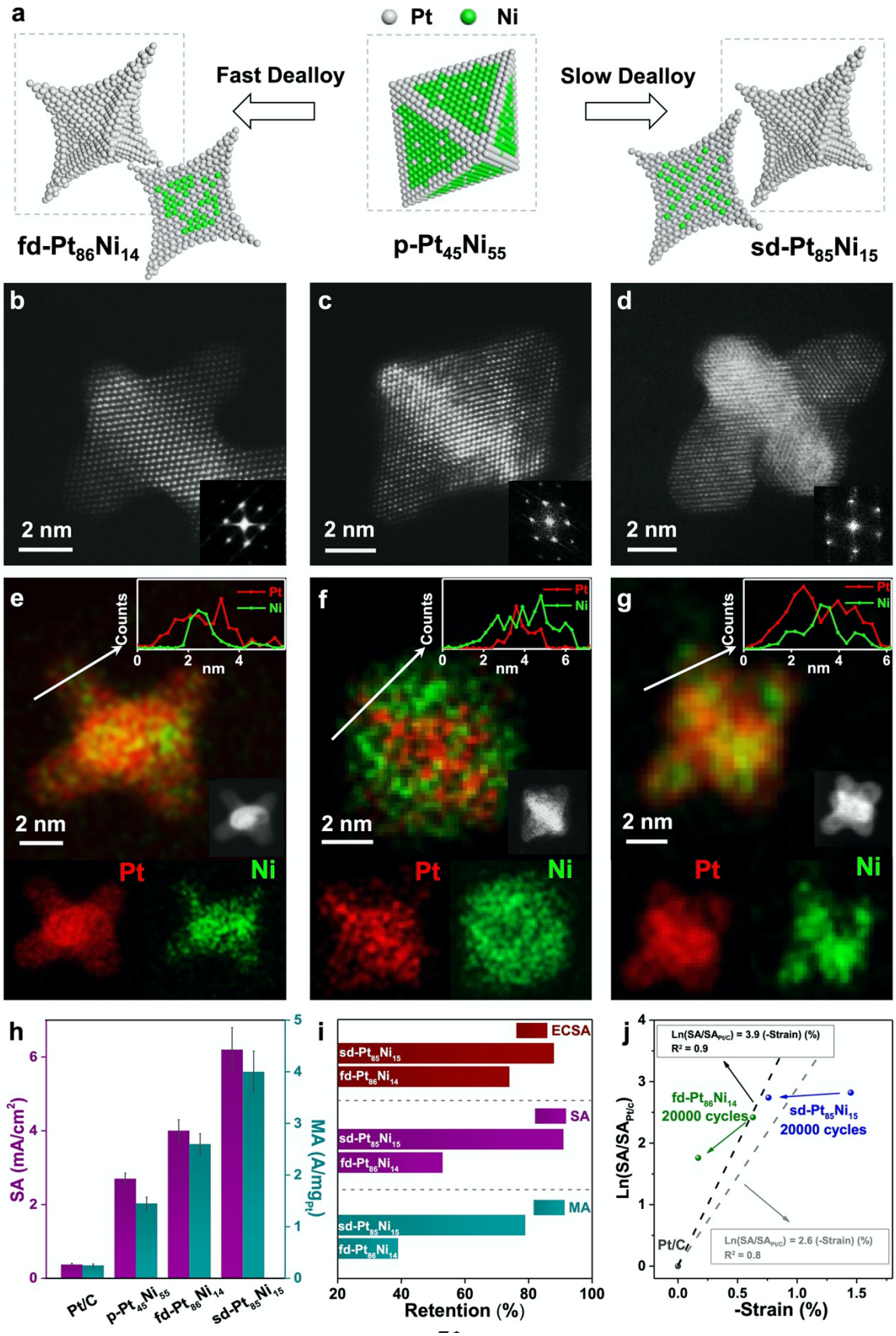
a
Pt
Ni
Fast Dealloy
Slow Dealloy
fd-Pt86Ni14
p-Pt45Ni55
sd-Pt85Ni15
b
c
d
2 nm
e
f
g
Counts
nm
Pt
Ni
h
SA (mA/cm2)
MA (A/mgPt)
Pt/C
p-Pt45Ni55
fd-Pt86Ni14
sd-Pt85Ni15
i
ECSA
SA
MA
Retention (%)
j
Ln(SA/SAPt/C) = 3.9 (-Strain) (%)
R2 = 0.9
fd-Pt86Ni14
20000 cycles
sd-Pt85Ni15
20000 cycles
Pt/C
Ln(SA/SAPt/C) = 2.6 (-Strain) (%)
R2 = 0.8
Ln(SA/SAPt/C)
-Strain (%)

Figure 2.1. Design and comparison of sd-PtNi and fd-PtNi catalysts. (**a**) Schematic illustration of the preparation of fd-PtNi catalyst and sd-PtNi catalyst from p-PtNi catalyst. (**b-d**) Representative high-resolution atomic HAADF-STEM images for fd-$Pt_{86}Ni_{14}$ (**b**), p-$Pt_{45}Ni_{55}$ (**c**), and sd-$Pt_{85}Ni_{15}$ (**d**), respectively. (**e-g**) Corresponding EDX mapping and line-scan profile analysis for fd-$Pt_{86}Ni_{14}$ (**e**), p-$Pt_{45}Ni_{55}$ (**f**), and sd-$Pt_{85}Ni_{15}$ (**g**). The insets in (**b-d**) are the corresponding FFT diffraction patterns. (**h**) Comparison of SAs and MAs of p-$Pt_{45}Ni_{55}$, fd-$Pt_{86}Ni_{14}$, sd-$Pt_{85}Ni_{15}$ catalysts at 0.9 V versus RHE. (**i**) Comparison of the retention of ECSA, SA, and MA of fd-$Pt_{86}Ni_{14}$ and sd-$Pt_{85}Ni_{15}$ catalyst at 0.9 V versus RHE, showing that sd-$Pt_{85}Ni_{15}$ has much better retention than fd-$Pt_{86}Ni_{14}$ in all aspects. (**j**) The linear relationship between Ln(SA/SA_{Pt}) and (-Strain %) of the catalysts. The black dashed line is fitted without sd-$Pt_{85}Ni_{15}$ before ADT, showing a better agreement ($R^2 = 0.9$) than the gray dashed line with sd-$Pt_{85}Ni_{15}$ before ADT ($R^2 = 0.8$), suggesting the strain alone cannot fully account for the observed difference in SA of all the catalysts.

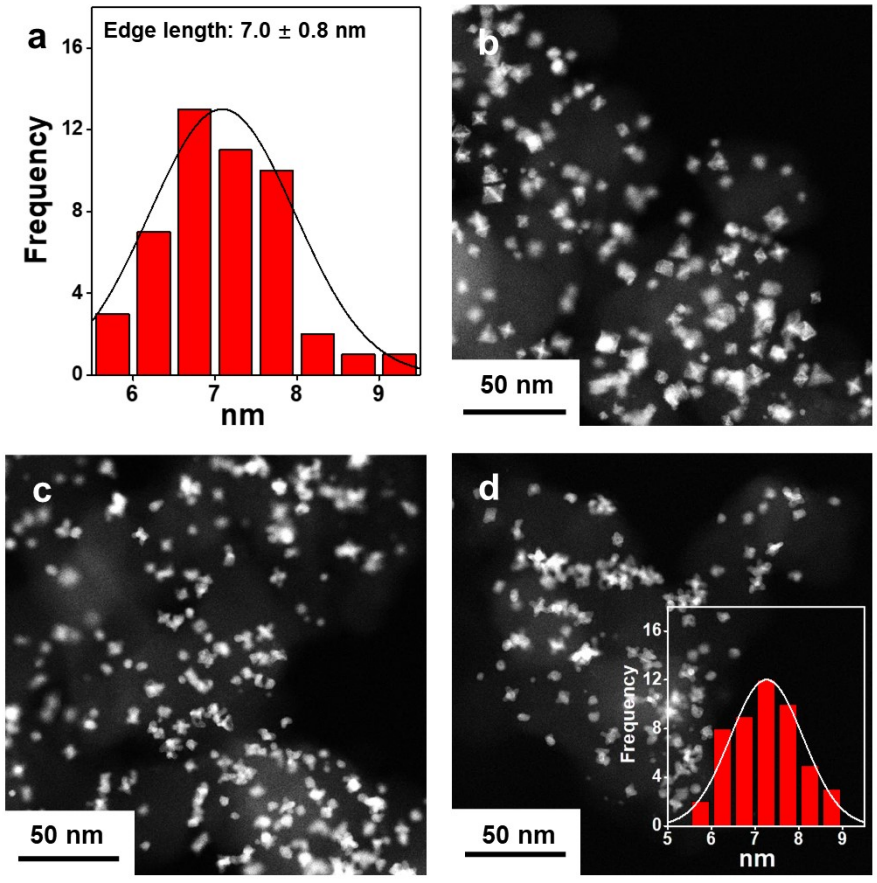

Figure 2.2. TEM analysis of sd-PtNi catalysts at different stages. (**a**) Size distribution of octahedral p-$Pt_{45}Ni_{55}$ catalysts. (**b-d**) Representative HAADF-STEM images for p-$Pt_{45}Ni_{55}$, sd-$Pt_{76}Ni_{24}$, and sd-$Pt_{85}Ni_{15}$, respectively. The inset of the panel (**d**) is the size distribution of sd-$Pt_{85}Ni_{15}$, diagonal distance is the longest distance between two diagonal branched tips.

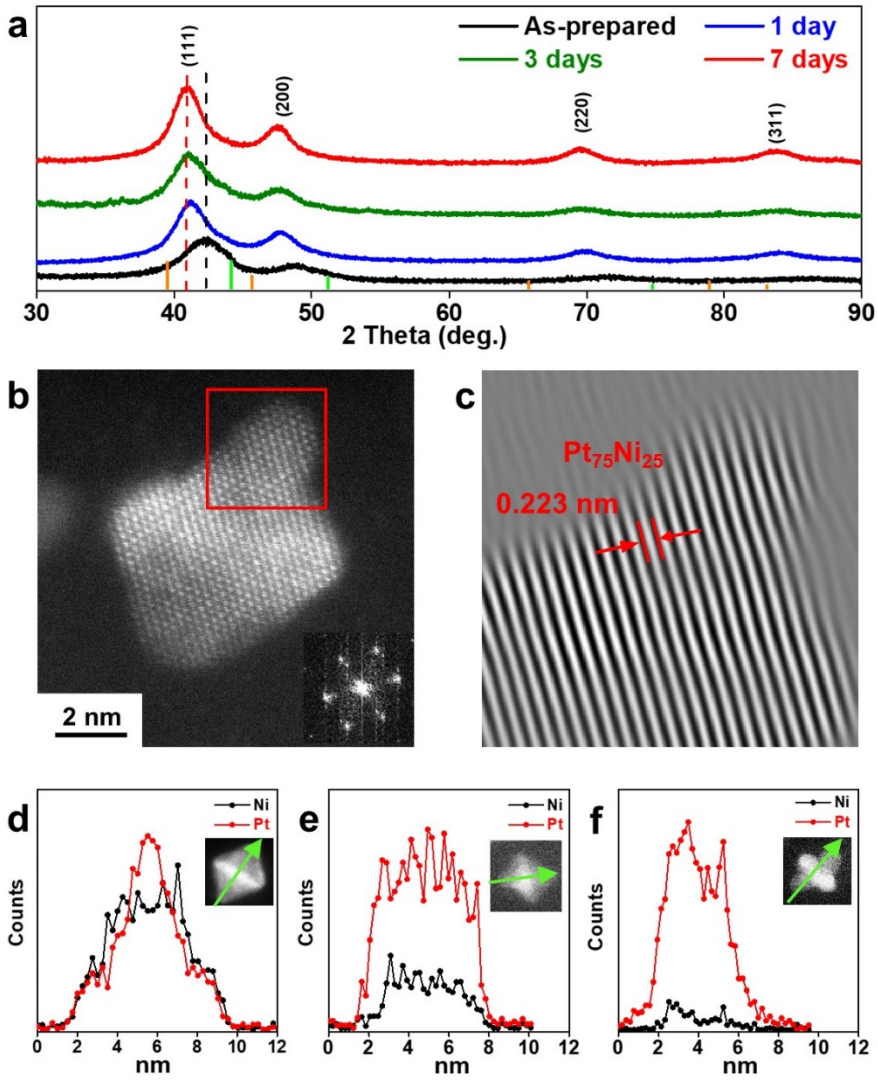

Figure 2.3. Structural characterization of sd-PtNi catalysts during the slow dealloying process. (**a**) XRD patterns of sd-PtNi catalysts at different dealloying time. Orange line and green line represent Pt [PDF #04-0802] and Ni [PDF #04-0850], respectively. (**b**) High-resolution atomic HAADF-STEM images of sd-$Pt_{76}Ni_{24}$ catalysts. (**c**) Corresponding inverse FFT images of sd-$Pt_{76}Ni_{24}$ catalysts (the red square region in the panel (**c**)). (**d-f**) Representative EDX line-scan profile for p-$Pt_{45}Ni_{55}$, sd-$Pt_{76}Ni_{24}$, and sd-$Pt_{85}Ni_{15}$, respectively. The insets of the (**d-f**) are the corresponding HAADF-STEM images.

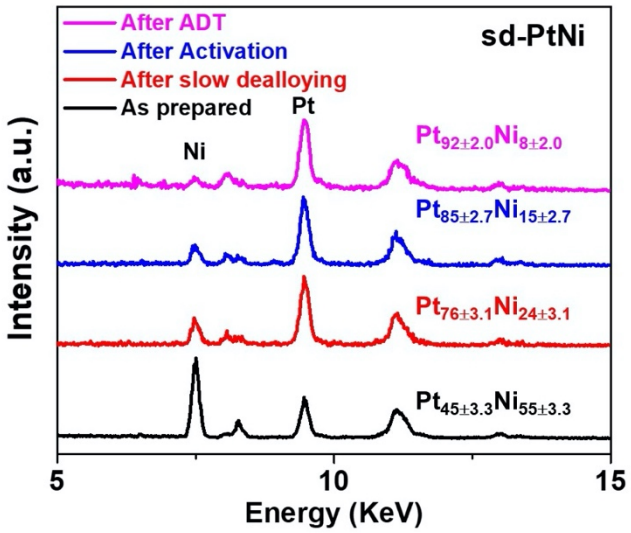

Figure 2.4. EDX compositional analysis of sd-PtNi catalysts at different stages. Each stage corresponds to p-$Pt_{45}Ni_{55}$ (black), sd-$Pt_{76}Ni_{24}$ (red), sd-$Pt_{85}Ni_{15}$ (blue), and sd-$Pt_{92}Ni_{8}$-ADT (pink), respectively.

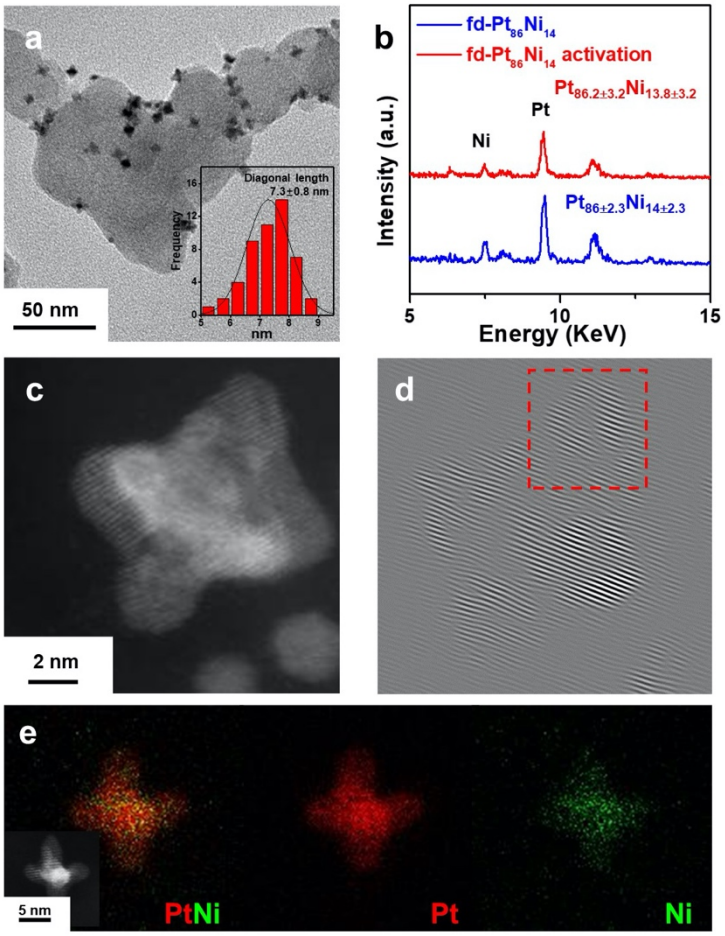

Figure 2.5. Structural and compositional analysis of the fd-$Pt_{86}Ni_{14}$ catalysts. (**a**) TEM of the fd-$Pt_{86}Ni_{14}$ catalysts before activation. (**b**) EDX composition analysis of the fd-$Pt_{86}Ni_{14}$ catalysts before and after activation, showing no obvious difference due to sufficient acid dealloying. (**c**) HAADF-STEM image of the fd-$Pt_{86}Ni_{14}$ catalysts. (**d**) Inverse fast Fourier transform (FFT) of the corresponding fd-$Pt_{86}Ni_{14}$ catalysts in the panel (**c**), showing similar Pt skin structure after fast acid dealloying. (**e**) EDX mapping results of the fd-$Pt_{86}Ni_{14}$ catalysts before activation.

To obtain sd-PtNi, the p-$Pt_{45}Ni_{55}$ catalysts were dispersed in DMF solution and heated to 120 °C under air purge to allow the slow dissolution of Ni. This slow process allowed additional time for the remaining atoms to rearrange themselves into a structure closer to equilibrium[31], achieving stable concave sd-PtNi catalysts. The changes in the structure and composition of octahedral sd-PtNi catalysts were traced by XRD over the course of the slow dealloying (Figure 2.3a). It was observed that the main XRD peaks shifted continuously towards low angles, indicating the lattice spacing relaxation due to transformation from Ni-rich alloys to Pt-rich alloys, and stabilized after three days of dealloying. The average (111) lattice spacing in the sd-PtNi shifted to 0.223 nm from 0.212 nm (Figure 2.3c), indicating a composition change from $Pt_{45}Ni_{55}$ to $Pt_{75}Ni_{25}$ based on the Vegard's law, which is consistent with the energy dispersive X-ray (EDX) results ($Pt_{45}Ni_{55}$ to $Pt_{76}Ni_{24}$) (Figure 2.4). TEM studies also revealed that the octahedra evolved to the concave octahedra after three days of dealloying (Figures 2.2c, 2.3b). The resulting sd-$Pt_{76}Ni_{24}$ further evolved to highly concaved sd-$Pt_{85}Ni_{15}$ after electrochemical activation according to EDX spectroscopy results (Figures 2.1d, 2.4). The EDX mapping and line-scan profile of sd-$Pt_{85}Ni_{15}$ showed a Pt skin of about 0.7 nm after the activation process (Figure 2.1g). The fd-$Pt_{86}Ni_{14}$ catalysts were obtained through a fast 0.5 M sulfuric acid leaching treatment of the p-$Pt_{45}Ni_{55}$. The resulting fd-$Pt_{86}Ni_{14}$ showed similar highly concaved morphology and similar composition to those of the sd-$Pt_{85}Ni_{15}$, together with a similar Pt-skin structure after electrochemical activation (Figures 2.1b, e, 2.5). In addition, the ECSA was determined to be 65 m^2/g_{Pt} for sd-$Pt_{85}Ni_{15}$ and 67

m^2/g_{Pt} for fd-$Pt_{86}Ni_{14}$, respectively. Both were comparable with that of commercial Pt/C (68 m^2/g_{Pt}, 20 wt% Pt, Alfa Aesar) and higher than that of p-$Pt_{45}Ni_{55}$ (52 m^2/g_{Pt}) (Figure 2.6a).

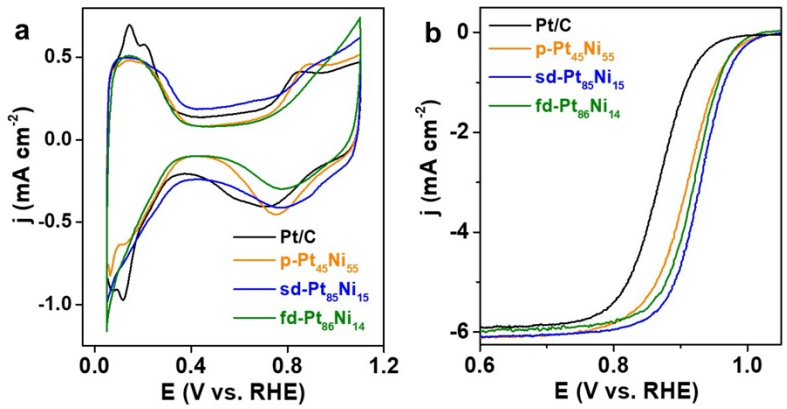

Figure 2.6. Electrochemical measurement of p-$Pt_{45}Ni_{55}$, sd-$Pt_{85}Ni_{15}$, and fd-$Pt_{86}Ni_{14}$ versus commercial Pt/C catalysts. (**a**) CVs of p-$Pt_{45}Ni_{55}$ (orange), sd-$Pt_{85}Ni_{15}$ (blue), and fd-$Pt_{86}Ni_{14}$ (olive) versus commercial Pt/C catalysts (black) recorded at room temperature in N_2-purged 0.1 M $HClO_4$ solution at a sweep rate of 100 mV/s from 0.05 to 1.1 V vs. RHE. (**b**) ORR polarization curves of p-$Pt_{45}Ni_{55}$ (orange), sd-$Pt_{85}Ni_{15}$ (blue), and fd-$Pt_{86}Ni_{14}$ catalysts (olive) in comparison to Pt/C catalysts (black). The ORR tests were measured in O_2-purged 0.1 M $HClO_4$ solution at a sweep rate of 20 mV/s from 0.05 to 1.1 V vs. RHE.

Despite the similarity in composition, highly concaved morphology, and Pt-skin, the ORR activity and stability of sd-$Pt_{85}Ni_{15}$ and fd-$Pt_{86}Ni_{14}$ catalysts showed considerable differences. The sd-$Pt_{85}Ni_{15}$ catalysts displayed a high SA of 6.2 ± 0.6 mA/cm^2 at 0.9 V versus RHE (Figure 2.1h, Figure 2.6b), which was much higher than those of fd-$Pt_{86}Ni_{14}$ (4.0 ± 0.3 mA/cm^2), p-$Pt_{45}Ni_{55}$ (2.7 ± 0.2 mA/cm^2), and commercial Pt/C (0.37 ± 0.04 mA/cm^2). The sd-$Pt_{85}Ni_{15}$ showed a high MA of 4.0 ± 0.4 A/mg_{Pt}, which was about 1.5 times that of fd-$Pt_{86}Ni_{14}$ (2.6 ± 0.2 A/mg_{Pt}), about 2.8 times that of p-$Pt_{45}Ni_{55}$ (1.4 ± 0.1 A/mg_{Pt}), and about 16.0 times that of Pt/C (0.25 ± 0.03 A/mg_{Pt}). Intriguingly, the durability of the sd-$Pt_{85}Ni_{15}$ and fd-$Pt_{86}Ni_{14}$ catalysts showed a more significant difference. After 20,000 cycles of ADT in O_2-saturated $HClO_4$, for sd-$Pt_{85}Ni_{15}$, the ECSA dropped by only 12%, SA dropped by 9%, and the MA dropped by only 21% (Figures 2.1i, 2.8). These

losses were much lower than those of the fd-$Pt_{86}Ni_{14}$ (47% in SA, 26% in ECSA, and 61% drop in MA) (Figure 2.8a, b), despite their similar composition and morphology. It was found that the composition of sd-$Pt_{85}Ni_{15}$ changed to sd-$Pt_{92}Ni_{8}$-ADT, and that of the fd-$Pt_{86}Ni_{14}$ changed to fd-$Pt_{95}Ni_{5}$-ADT (Figure 2.8d). Importantly, it was also found that sd-PtNi maintained the concave morphology after ADT without obvious size change (Figure 2.7c, d), whereas fd-PtNi transformed mostly into spherical nanoparticles (Figure 2.8c).

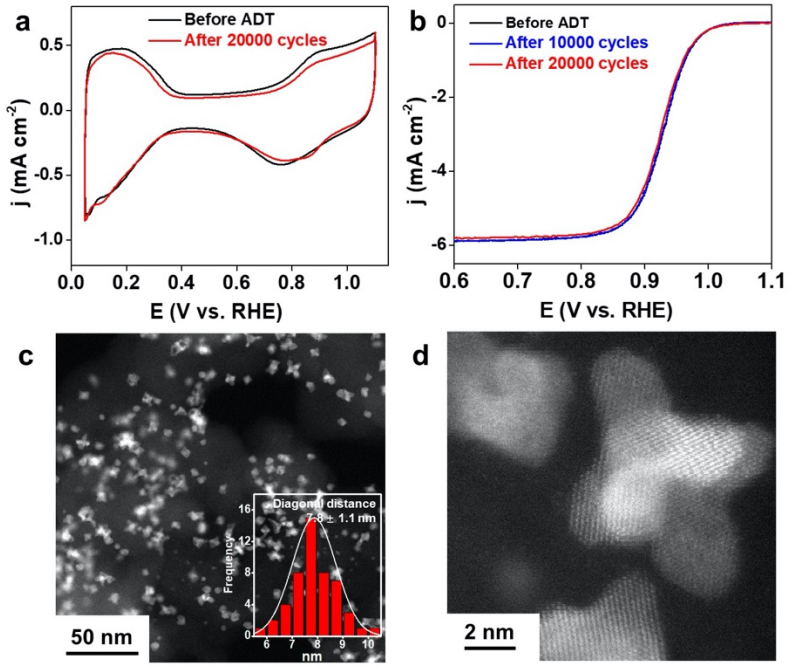

Figure 2.7. Electrochemical stability analysis of sd-$Pt_{85}Ni_{15}$ catalysts. (**a**) CV curves of sd-$Pt_{85}Ni_{15}$ catalysts before (black) and after 20,000 cycles ADT (red). (**b**) ORR polarization curves of sd-$Pt_{85}Ni_{15}$ catalysts before stability test (black), after 10,000 cycles ADT (blue), and after 20,000 cycles ADT (red). (**c, d**) Representative HAADF-STEM and high-resolution HAADF-STEM image of the sd-PtNi after 20,000 cycles ADT, the inset of the panel (**c**) is the size distribution of sd-PtNi after ADT, diagonal distance is the longest distance of two diagonal branched tips. The diagonal distance slightly increased from 7.2 nm to 7.8 nm without obvious growth for each branch, suggesting good structural and morphology stability.

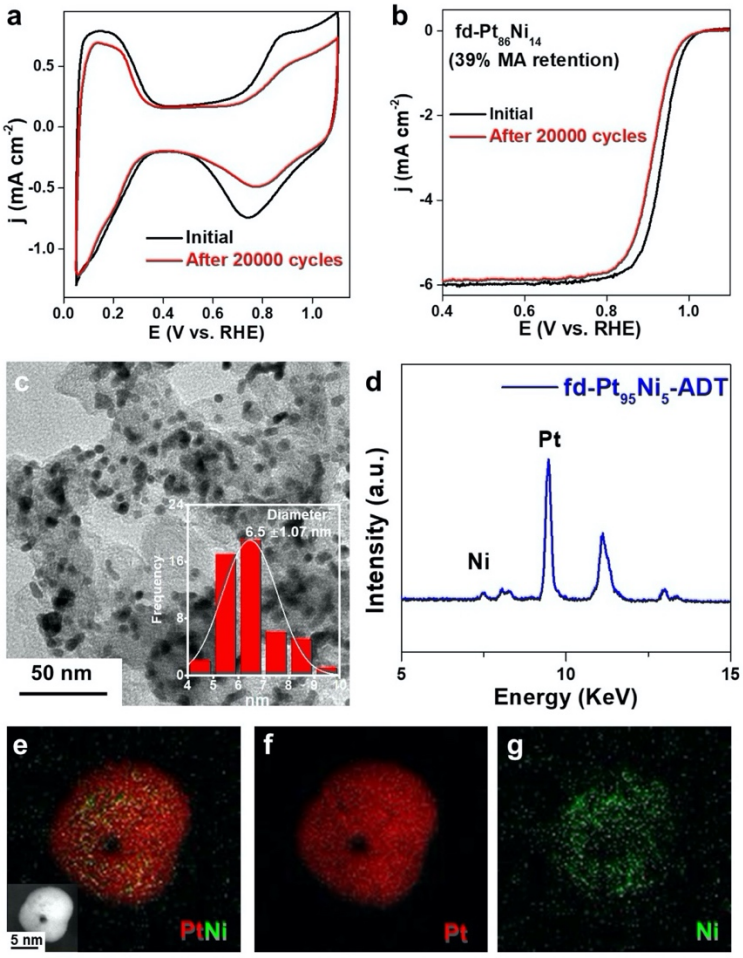

Figure 2.8. Electrochemical stability analysis of fd-$Pt_{86}Ni_{14}$. (**a**) CV curves of fd-$Pt_{86}Ni_{14}$ catalysts before (black) and after 20,000 cycles ADT (red). (**b**) ORR polarization curves of fd-$Pt_{86}Ni_{14}$ catalysts before (black) and after 20,000 cycles ADT (red). (**c**) TEM image of fd-$Pt_{86}Ni_{14}$ after 20,000 cycles ADT, the inset of panel (**c**) is the size distribution of fd-$Pt_{95}Ni_5$-ADT. (**d**) EDX spectrum of the fd-$Pt_{86}Ni_{14}$ after 20,000 cycles ADT. (**e-g**) EDX mapping results of fd-$Pt_{95}Ni_5$-ADT after 20,000 cycles ADT, the inset of panel (**e**) is the HRTEM.

Development of BED and the Sabatier plot

To understand the structural details that render sd-$Pt_{85}Ni_{15}$ superior in activity and stability to fd-$Pt_{86}Ni_{14}$, we performed *in-situ* X-ray absorption spectroscopy (XAS) studies. According to the *in-situ* EXAFS spectra at the Pt L_3-edge (Figure 2.9, Table 2.1), the Pt-Pt bond lengths of both sd-$Pt_{85}Ni_{15}$ (2.71 Å) and fd-$Pt_{86}Ni_{14}$ (2.73 Å) are shorter compared to

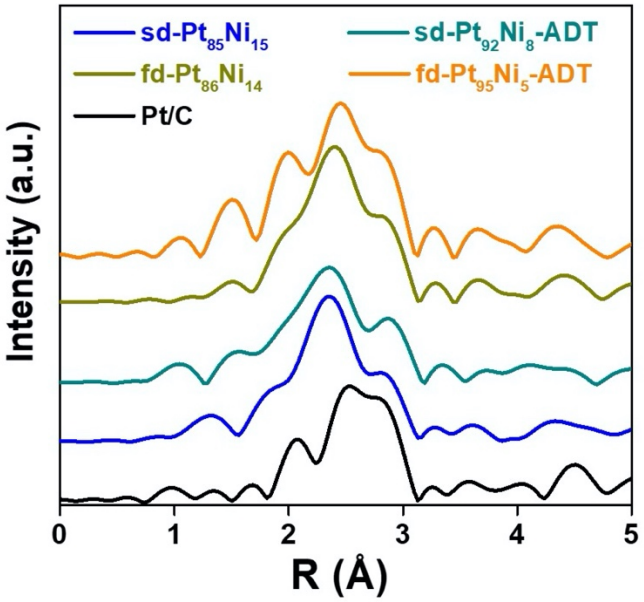

Figure 2.9. Experimental EXAFS results. *In-situ* EXAFS spectra at the Pt L_3-edge for sd-$Pt_{85}Ni_{15}$ (blue), fd-$Pt_{86}Ni_{14}$ (light brown), sd-$Pt_{92}Ni_8$-ADT (bright blue), fd-$Pt_{95}Ni_5$-ADT (orange), and Pt/C (black). *In-situ* data were collected in an O_2-purged 0.1 M $HClO_4$ electrolyte at 0.54 V versus RHE (double-layer potential region).

that of Pt/C (2.75 Å), resulting in strain and the improved SA over Pt/C. These results confirm that the Ni-induced compressive strain benefits the ORR activity. In addition, we found that after 20,000 cycles of ADT, the Pt-Pt bond lengths of sd-$Pt_{85}Ni_{15}$ and fd-$Pt_{86}Ni_{14}$ relaxed to 2.73 Å and 2.75 Å, respectively (Figure 2.1j, Table 2.1). This Pt-Pt bond length relaxation indicates further dealloying and structural reorganization during ADT, which leads to the decrease in SA. However, we observed that although sd-$Pt_{85}Ni_{15}$ experienced Pt-Pt bond relaxation (2.71 Å to 2.73 Å) after ADT, its SA was largely maintained (from 6.2 ± 0.6 mA/cm^2 to 5.6 ± 0.3 mA/cm^2) compared to that of fd-$Pt_{86}Ni_{14}$, whereas a Pt-Pt bond relaxation from 2.73 Å to 2.75 Å has led to a more drastic change in SA from 4.0 ± 0.3 mA/cm^2 to 2.1 ± 0.3 mA/cm^2. Intriguingly, after ADT, sd-$Pt_{92}Ni_8$-ADT showed a considerably higher SA (5.6 ± 0.3 mA/cm^2) compared to that of the fd-$Pt_{86}Ni_{14}$ before ADT (4.0 ± 0.3 mA/cm^2), despite the same Pt-Pt bond length of 2.73 Å. This observation suggests that the Pt strain alone cannot fully account for the observed change in SA

Table 2.1. Summaries of EXAFS fitting results of sd-Pt-alloys at the Pt L_3-edge and Ni K-edge. * The number in parentheses represents the statistical error and applies to the last digit.

Pt side			Pt-Pt scattering			Pt-M (M = Ni and/or Co) scattering		
	Stages	Composition	R_{Pt-Pt} (Å)	N_{Pt-Pt}	σ2 (Å^2)×10^{-3}	R_{Pt-M}(Å)	N_{Pt-M}	σ2 (Å^2)×10^{-3}
sd-$Pt_{85}Ni_{15}$	BOL	$Pt_{85}Ni_{15}$	2.71(1)	8.6(1.4)	9(1)	2.65(1)	1.5(0.5)	5(2)
	ADT	$Pt_{92}Ni_8$	2.73(1)	10(2)	9(2)	2.62(6)	0.7(4)	6(3)
sd-$Pt_{84}Ni_{12}Co_4$	BOL	$Pt_{84}Ni_{12}Co_4$	2.714(7)	7.8(1.0)	7.4(9)	2.65(1)	2.1(6)	9(2)
	ADT	$Pt_{87}Ni_{10}Co_3$	2.72(3)	9.6(2.4)	9(3)	2.67(2)	1.1(1.1)	2(6)
fd-$Pt_{86}Ni_{14}$	BOL	$Pt_{86}Ni_{14}$	2.733(4)	8.2(7)	6.6(6)	2.659(7)	1.2(3)	5(1)
	ADT	$Pt_{95}Ni_5$	2.746(9)	7.5(1.4)	5(2)	2.60(2)	1(3)	2

Ni side		Ni-Pt scattering			Ni-M (M = Ni and/or Co) scattering		
	Stages	R_{Ni-Pt} (Å)	N_{Ni-Pt}	σ2 (Å^2)×10^{-3}	R (Å)	NN_{i-Ni}	σ2 (Å^2)×10^{-3}
sd-$Pt_{85}Ni_{15}$	BOL	2.66(2)	5.2(1.8)	5(3)	2.64(3)	3.6(1)	13(9)
	ADT						
sd-$Pt_{84}Ni_{12}Co_4$	BOL	2.65(1)	6.9(1.3)	9(2)	2.64(1)	5.1(1.5)	13(4)
	ADT						
fd-$Pt_{86}Ni_{14}$	BOL	2.659(7)	7(1)	5(1)	2.60(3)	1.7(1.5)	9(8)
	ADT						

*Fits were performed at the Pt L_3 and Ni K-edge simultaneously in *R*-space, $k^{1,2,3}$ weighting. 1.2 < *R* < 3.1 Å and Δ*k* = 2.8 – 12.2 Å^{-1} for Pt spectra and 1.3 < *R* < 3.1 Å and Δ*k* = 2.6 – 11.6 Å^{-1} for Ni spectra were used for fitting. S_0^2 was fixed at 0.84 and 0.68 for Pt and Ni, respectively, as obtained by fitting the corresponding reference foils. The number given in the parentheses represents the uncertainty of the last digit of the fitting result. BOL: beginning of life.

for sd-$Pt_{85}Ni_{15}$ before and after ADT. Indeed, the linear regression fittings between Ln(SA/SA_{Pt}) and (-Strain, %) of the catalysts, suggest a much better fitting without sd-$Pt_{85}Ni_{15}$ before ADT (R^2 = 0.9) than the one with sd-$Pt_{85}Ni_{15}$ before ADT (R^2 = 0.8) (Figure 2.1j). This finding calls for a thorough investigation, especially on sd-$Pt_{85}Ni_{15}$, to capture contributing factors to the catalytic activity beyond simply strain.

A further examination of the sd-Pt-alloys and fd-Pt-alloys before and after ADT using *in-situ* Pt-L_3 XANES spectra revealed additional structural details that may contribute to the apparent

difference in ORR activity and stability between the two classes of catalysts. Specifically, sd-$Pt_{85}Ni_{15}$ showed a considerable peak broadening in the energy range of 11564 eV to 11576 eV, compared to fd-$Pt_{86}Ni_{14}$ and commercial Pt/C (Figure. 2.10a), pointing to some unique atomic structural features achieved within the catalyst. XANES peak broadening was also observed for fd-$Pt_{86}Ni_{14}$ although at a much less extent (Figure. 2.10a). However, after 20,000 cycles of ADT, the peak broadening remained prominent in sd-$Pt_{92}Ni_{8}$-ADT, while it was nearly gone in fd-$Pt_{95}Ni_{5}$-ADT (Figure. 2.10a). Together with the different catalyst morphologies after ADT in sd-PtNi and in fd-PtNi, this observation suggests that the peak broadening in the Pt L_3-edge XANES spectra correlates with the fine structure of Pt-alloys which may be associated with structural stability. This broadening phenomenon has been observed, although little noted, in XAS studies of intermetallic Pt-alloys featuring enriched charge transfer, such as the ordered intermetallic PtFe[32], PtNiCo[33], and annealed PtCu[34] and PtCo[35]. In particular, the Pt L_3-edge XANES peak area has been shown to reflect multiple scattering involving both Pt and M neighboring atoms and the change of density of states of the 5d-orbitals, where its tailing to the higher energy indicates intensified Pt-M coupling[36-38]. In addition, we found that annealing the p-PtNi catalysts can also lead to an ultra-broad XANES peak (Figure. 2.11) together with a high Pt-Ni coordination number (7 ± 1) (Table 2.2). We, therefore, infer that the XANES peak broadening observed in sd-$Pt_{85}Ni_{15}$ is associated with an intimate mixing of Ni and Pt in the catalysts that facilitates the charge transfer between the Pt and Ni[36,39], denoting an intensified Pt-Ni coupling that weakens the Pt-O binding and in turn improves the intrinsic ORR activity of Pt[6]. We hypothesize that the drastic broadening and the resulting tailing of the *in-situ* Pt XANES peak towards higher energy observed in sd-Pt-alloys may be a characteristic feature useful for representing Pt-M coupling that encompasses

ligand effect and local atomic coordination contribution to the ORR activities in Pt-M alloys in general.

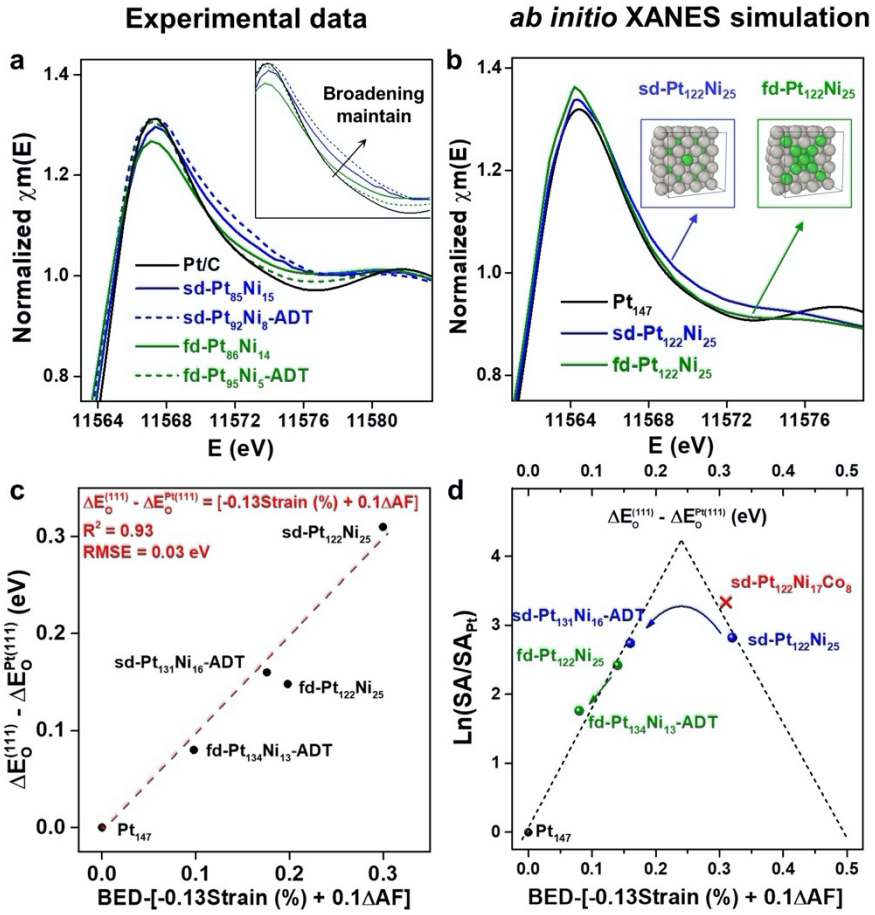

Figure 2.10. Development of the binary experimental descriptor (BED) and the Sabatier plot for predicting high-performance ORR catalyst. (**a**) Experimental Pt L_3-edge *in-situ* XANES spectra of sd-$Pt_{85}Ni_{15}$ (blue), sd-$Pt_{92}Ni_8$-ADT (blue-dashed), fd-$Pt_{86}Ni_{14}$ (olive), and fd-$Pt_{95}Ni_5$-ADT (olive-dashed) catalyst compared to Pt/C catalyst (black) collected at 0.54 V in O_2-saturated 0.1 M $HClO_4$ solution. The inset panel is an enlarged region in panel (**a**), showing that the XANES broadening observed in sd-PtNi samples maintained after ADT. (**b**) Calculated Pt L_3-edge XANES spectra for Pt_{147} (black), sd-$Pt_{122}Ni_{25}$ (blue), and fd-$Pt_{122}Ni_{25}$ (olive) cluster models, showing similar broadening for sd-$Pt_{122}Ni_{25}$ models. The inset of panel (**b**) shows the cluster models of sd-$Pt_{122}Ni_{25}$ and fd-$Pt_{122}Ni_{25}$ clusters. (**c**) Linear regression fitting between the DFT-determined ($\Delta E_O^{(111)} - \Delta E_O^{Pt(111)}$) and the BED-[-0.13Strain (%) + 0.1ΔAF] based on the cluster models, showing good one-to-one correspondence. RMSE: Root-mean-square error. (**d**) The Sabatier-like relationship between experimentally measured activity ($Ln(SA/SA_{Pt})$) of Pt/C, sd-PtNi, fd-PtNi catalyst before and after 20,000 cycles of ADT and their corresponding simulated BED-[-0.13Strain (%) +

0.1ΔAF] based on cluster models. The top X-axis is the DFT-determined difference of oxygen binding energy ($\Delta E_O^{(111)}$ - $\Delta E_O^{Pt(111)}$). The red cross indicates the theoretically predicted high-performance sd-PtNiCo catalyst.

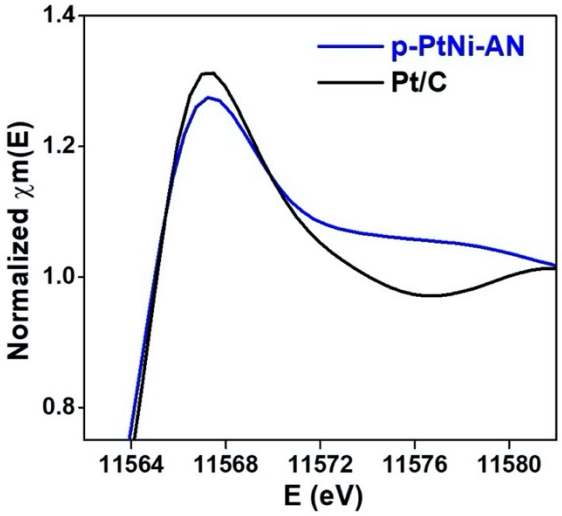

Figure 2.11. XANES spectra of p-PtNi-AN (blue) and Pt/C catalysts (black). The p-PtNi-AN catalyst was activated in N_2-saturated 0.1 M $HClO_4$ between 0.05 V to 1.1 V versus RHE at a scan rate of 100 mV/s prior to XAS measurement.

Table 2.2. Summaries of EXAFS fitting results of the Pt L_3-edge spectra of examined samples. The number in parentheses represents the statistical error and applies to the last digit.

	Pt-Pt scattering			Pt-M (M = Ni and/or Co) scattering		
Sample	R_{Pt-Pt} (Å)	N_{Pt-Pt}	σ2 (Å^2)×10^{-3}	R_{Pt-M}(Å)	N_{Pt-M}	σ^2(Å^2)×10^{-3}
fd-$Pt_{84}Ni_{12}Co_4$	2.717(5)	7.6(1.3)	5.6(9)	2.65(2)	2.7(1.4)	1.2(4)
fd-$Pt_{93}Ni_5Co_2$	2.727(2)	8.4(5)	6.1(4)	2.65(1)	1.7(4)	8(2)
p-$Pt_{40}Ni_{60}$-AN	2.68(1)	2(1)	5(3)	2.569(4)	7(1)	5(7)
p-$Pt_{41}Ni_{57}Co_2$-AN	2.68(6)	1.8(0.7)	3(1)	2.565(2)	7.3(6)	5.1(5)
tetra-$Pt_{65}Cu_{28}Ni_7$	2.696(6)	4.4(1.0)	5(1)	2.623(8)	3.8(8)	7(2)
tetra-$Pt_{77}Cu_{15}N_8$	2.700(7)	5.6(1.0)	5.8(8)	2.637(9)	3.3(8)	7(2)
Oct-$Pt_{72}Ni_{13}Cu_{15}$	2.713(4)	7.6(7)	NA	2.66(1)	1.9(5)	NA
Oct-$Pt_{79}Ni_{15}Co_6$	2.715(9)	5.9(2.0)	NA	2.63(3)	4.1(2.0)	NA
Oct-$Pt_{61}Ni_{33}Co_6$	2.722(9)	6.3(1.9)	6(1)	2.64(2)	1.4(1.2)	7(6)

To confirm this, we constructed 147-atom cuboctahedra cluster models based on the experimental data (Figure. 2.12). In addition to a pure Pt_{147} cluster, we generated Pt-Ni clusters to represent fd-PtNi and sd-PtNi before and after ADT:

(1) a $Pt_{122}Ni_{25}$ cluster with Ni aggregated into the inner core and thus with the minimized number (204) of Pt-Ni nearest neighbor bonds to represent the fast dealloying of peripheral Ni atoms in fd-$Pt_{86}Ni_{14}$, termed fd-$Pt_{122}Ni_{25}$;

(2) a fd-$Pt_{134}Ni_{13}$-ADT cluster with the minimized number of Pt-Ni bonds and a lower Ni content than fd-$Pt_{122}Ni_{25}$ to represent fd-$Pt_{95}Ni_{5}$-ADT;

(3) a sd-$Pt_{122}Ni_{25}$ cluster with 25 Ni and an intimate alloying of Ni and Pt in the particle core that thus maximizes the number (252) of Pt-Ni nearest neighbor bonds to represent the slow leaching together with atomic reordering of Ni into an energetically stable distribution in sd-$Pt_{85}Ni_{15}$; and

(4) a sd-$Pt_{131}Ni_{16}$-ADT cluster with the maximum number of Pt-Ni bonds but a lower Ni content than sd-$Pt_{122}Ni_{25}$ to represent sd-$Pt_{92}Ni_{8}$-ADT.

All clusters present pure Pt skin. Density functional theory (DFT) geometry relaxation was performed on all structures. We then simulated XANES spectra via *ab initio* FEFF9 calculations[40] for the geometry-relaxed cluster models (Figure. 2.10b). Notably, we observed similar peak broadening in the simulated Pt-L_3 XANES of sd-Pt-alloy models with distributed Ni compared to Pt_{147}. In contrast, no obvious peak broadening was observed in fd-Pt-alloy models with aggregated Ni (Figures. 2.10b, 2.13), consistent with experimental observations (Figure. 2.10a). A closer look into different sites in sd-$Pt_{122}Ni_{25}$ revealed that Pt sites featuring enriched Pt-Ni pairs showed obvious broadening, suggesting Pt-Ni coupling in play (Figure. 2.14a). The combined experimental and computational results so far confirmed the correlation between atomic Pt-Ni distribution in Pt-alloys and Pt L_3 XANES peak broadening. Therefore, we advocate that Pt-L_3

XANES peak broadening can be included in the activity descriptor for Pt-alloy nanocatalysts, together with the strain.

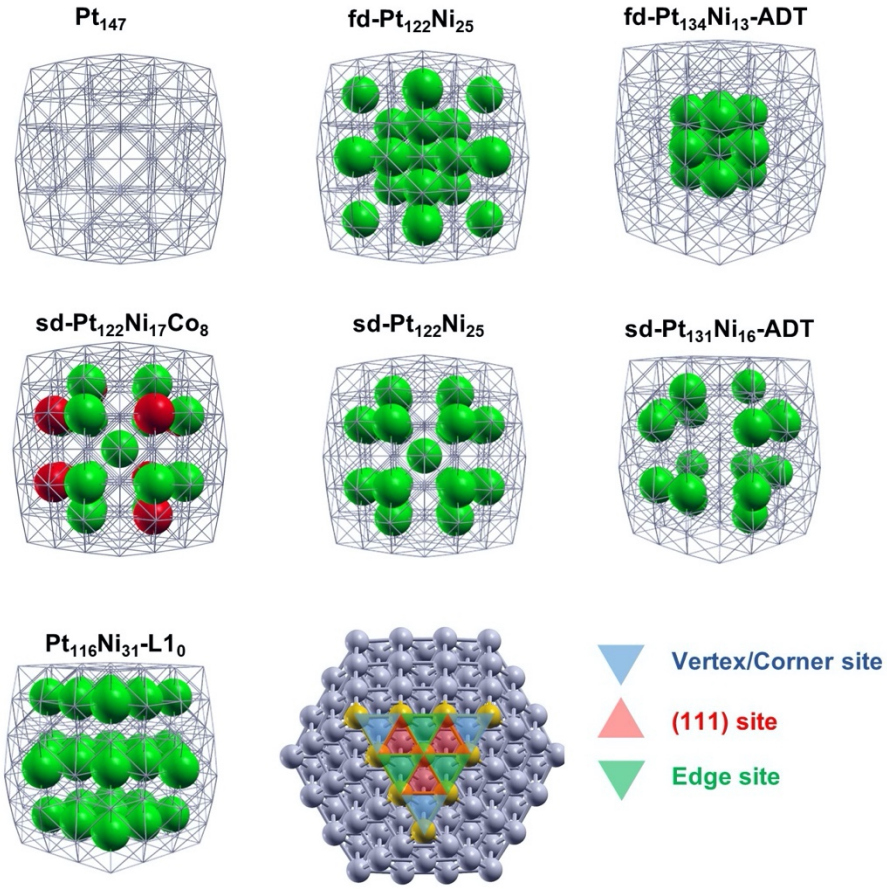

Figure 2.12. Schematic depiction of the 147-atom cluster models investigated in this work together with the location of O-adsorption sites: (111) sites, edge sites, and vertex sites. The grey frame represents the Pt frame. Grey, green, and red sphere represent Pt, Ni and Co, respectively.

We use the peak asymmetry factor (AF, see Figure 2.15 for details)[41] to represent the broadening in Pt-L_3 XANES peak, and further normalize the extent of peak broadening among Pt-based catalysts to ΔAF ($\Delta AF = AF_{Pt\text{-}alloy} - AF_{Pt/C}$) (Table 2.3). We developed a binary experimental descriptor (BED) (BED = A(Strain, %) + B(ΔAF)) that can be used to represent the theoretical ΔE_O, which in turn determines the ORR activity. Through optimal linear regression fitting between the DFT predicted [$\Delta E_O^{(111)} - \Delta E_O^{Pt(111)}$] (Figure. 2.16) and simulated BED on all 147 atom

cuboctahedra cluster models, with strain extracted from relaxed cluster structures and the ΔAF from calculated XANES spectra, we arrived at a BED = [-0.13Strain (%) + 0.1ΔAF]. Significantly, the optimal fitted BED showed a good linear one-to-one correspondence relationship with the calculated [$\Delta E_O^{(111)}$ - $\Delta E_O^{Pt(111)}$] with high fidelity (R^2 = 0.93, Root-mean-square error (RMSE) = 0.03 eV) (Figure. 2.10c), which is a considerably better fitting than the strain-only descriptor (R^2 = 0.82, RMSE = 0.04 eV, Figure. 2.17).

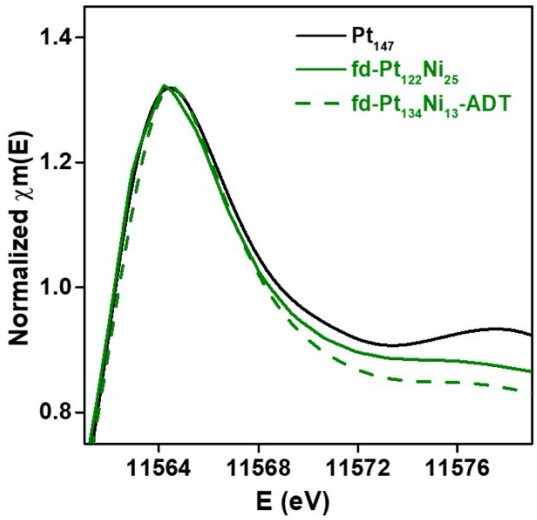

Figure. 2.13. FEFF9-derived Pt L_3-edge XANES spectra for Pt_{147} (black), fd-$Pt_{122}Ni_{25}$ (olive), and fd-$Pt_{134}Ni_{13}$-ADT (olive-dashed) cluster models. The XANES of fd-$Pt_{122}Ni_{25}$ and fd-$Pt_{134}Ni_{13}$-ADT were normalized to the height of the Pt_{147} model for comparison, showing no peak broadening.

We then plotted the experimental ORR activities with simulated BED, which demonstrated a clear Sabatier relationship, as one would expect for SA with the calculated [$\Delta E_O^{(111)}$ - $\Delta E_O^{Pt(111)}$],

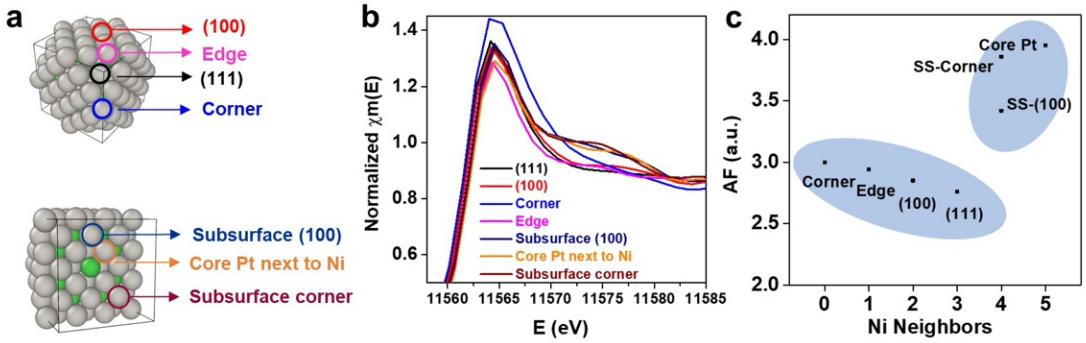

Figure. 2.14. (**a**) Depiction of specific sites of the mixed sd-$Pt_{122}Ni_{25}$ cluster. (**b**) Simulated XANES spectra by FEFF9 for the different sites of the sd-$Pt_{122}Ni_{25}$ model shown in (**a**). (**c**) The relationship between calculated AF and the number of Ni first-neighbors for different sites of the sd-$Pt_{122}Ni_{25}$ cluster model shown in (**a**), suggesting that Pt with more Ni neighbors generally showed a larger AF. SS-Corner: subsurface corner, SS-(111): subsurface (100), Core-Pt: Pt atoms located beneath the subsurface layer (the third layer).

Table 2.3. Summary of compressive strain, ΔAF, and activity.

Sample	Compressive strain (%)	ΔAF	Descriptor	Ln($SA_{PtM}/SA_{Pt/C}$)
sd-$Pt_{85}Ni_{15}$	1.45	0.43	0.23	2.82
sd-$Pt_{92}Ni_{8}$-ADT	0.73	0.45	0.14	2.74
sd-$Pt_{84}Ni_{12}Co_{4}$	1.31	0.49	0.22	3.37
sd-$Pt_{87}Ni_{10}Co_{3}$-ADT	1.09	0.37	0.18	3.33
fd-$Pt_{86}Ni_{14}$	0.62	0.27	0.11	2.46
fd-$Pt_{95}Ni_{5}$-ADT	0.36	0	0.04	1.76
fd-$Pt_{84}Ni_{12}Co_{4}$	1.20	0	0.15	2.42
fd-$Pt_{93}Ni_{5}Co_{2}$-ADT	0.84	0	0.11	1.80
Oct-$Pt_{72}Ni_{13}Cu_{15}$	1.27	0	0.17	2.82
Oct-$Pt_{61}Ni_{33}Co_{6}$	1.20	0.08	0.14	2.78
Oct-$Pt_{79}Ni_{15}Co_{6}$	1.09	0	0.17	2.54
J-PtNWs	1.45	0	0.19	3.49
p-$Pt_{40}Ni_{60}$ AN	2.54	0.50	0.38	1.68
p-$Pt_{41}Ni_{57}Co_{2}$ AN	2.54	0.45	0.37	1.72
tetra-$Pt_{65}Cu_{28}Ni_{7}$	1.82	0.36	0.27	2.74
tetra-$Pt_{77}Cu_{15}N_{8}$	1.82	0.41	0.28	2.93
$L1_0$-$Pt_{50}Ni_{40}Co_{10}$	1.82	0.67	0.30	2.47

Cluster Model	Compressive strain (%)	ΔAF	Descriptor	R_{Pt-Pt} (Å)
Pt_{147}	0	0	0	2.774
sd-$Pt_{122}Ni_{25}$	2.06	0.3	0.3	2.717
fd-$Pt_{122}Ni_{25}$	1.58	0	0.20	2.730
sd-$Pt_{122}Ni_{17}Co_{8}$	2.1	0.31	0.3	2.716
sd-$Pt_{131}Ni_{16}$-ADT	1.15	0.25	0.18	2.742
fd-$Pt_{134}Ni_{13}$-ADT	0.76	0	0.10	2.753

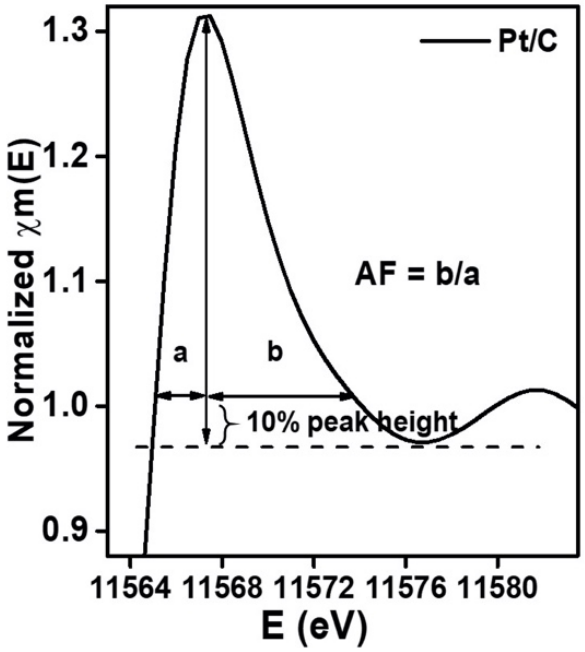

Figure. 2.15. Schematic illustration of AF calculation using XANES of Pt/C.

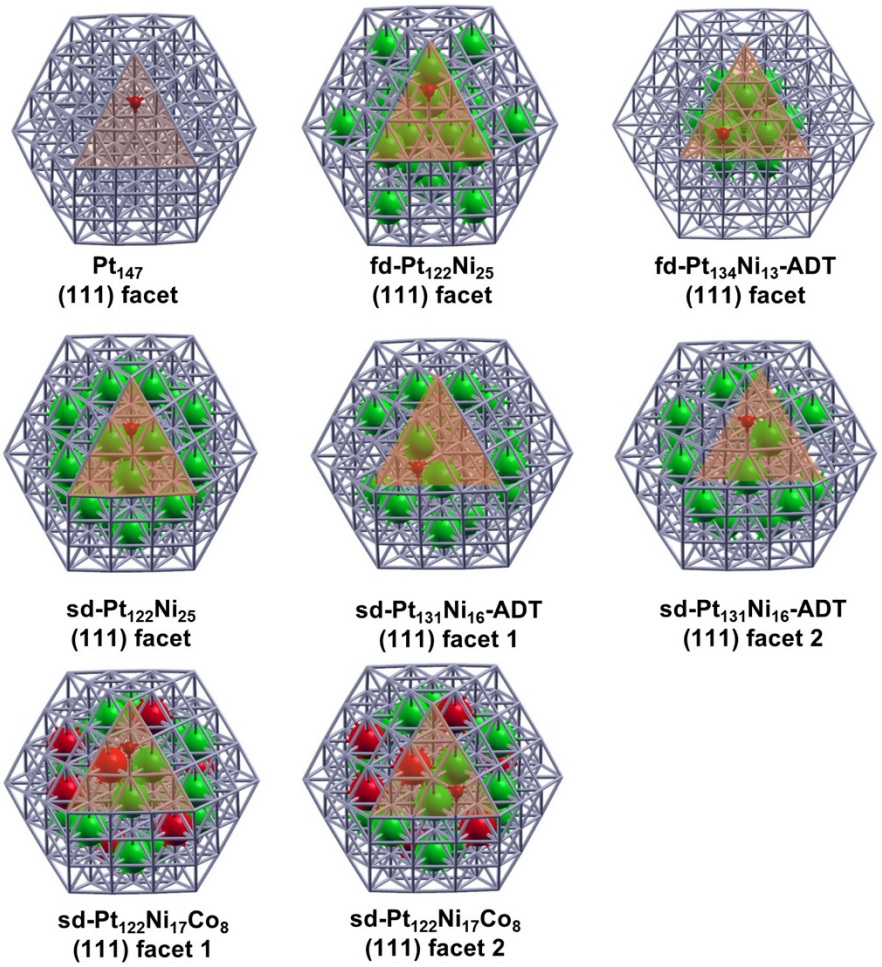

Figure. 2.16. Schematic depiction of 147-atom cluster models and O-binding on (111) sites. Note that in some cases there are 2 inequivalent adsorption sites, named as "facet 1" and "facet 2". In such cases, the oxygen binding energies reported in the main text are calculated as the average of oxygen binding energy of different (111) sites.

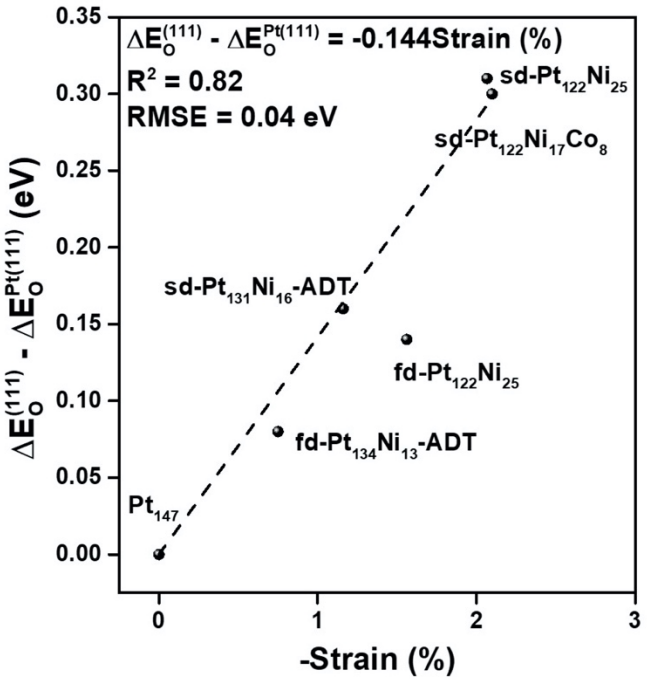

Figure. 2.17. Correlation between ($\Delta E_O^{(111)} - \Delta E_O^{Pt(111)}$) and (-Strain %), showing a R^2 of only 0.82. RMSE: Root-mean-square error.

suggesting that these two can be used interchangeably (Figure. 2.10d). Interestingly, we found that sd-$Pt_{122}Ni_{25}$ resides at the right (weaker Pt-O binding) leg of the Sabatier plot, while the fd-$Pt_{122}Ni_{25}$ locates at the left (stronger Pt-O binding) leg of the plot (Figure. 2.10d). This observation may be used to explain the observed better stability for sd-$Pt_{122}Ni_{25}$: upon ADT, the $\Delta E_O^{(111)}$ of sd-PtNi decreases first, shifting the activity of sd-PtNi upward on the right slope passing the optimal peak position, and then downward along the left slope to the end position (Figure. 2.10d, blue points), resulting in little change in activity despite large change in $\Delta E_O^{(111)}$. In comparison, the fd-$Pt_{122}Ni_{25}$ starts on the left leg of the Sabatier plot, whose activity decreases monotonically with the decreasing $\Delta E_O^{(111)}$ caused by strain relaxation (Figure. 2.10d, olive points). Correspondingly, our calculations also showed better thermodynamic stability for sd-$Pt_{122}Ni_{25}$ with a mixing energy[27] of -13.27 eV than fd-$Pt_{122}Ni_{25}$ (mixing energy of -12.24 eV) (Figure. 2.18),

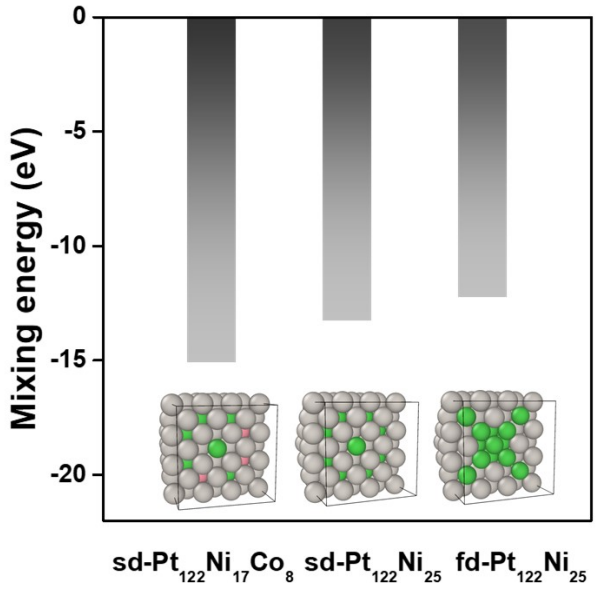

Figure 2.18. Mixing energy of sd-$Pt_{122}Ni_{17}Co_8$ (left), sd-$Pt_{122}Ni_{25}$ (middle), and fd-$Pt_{122}Ni_{25}$ (right) clusters.

consistent with experimental observations of the shape retention in sd-PtNi-ADT but not in fd-PtNi-ADT. The calculation also showed that the presence of enriched subsurface Ni, particularly in the slow-dealloyed structures significantly weakened the interaction between the oxygen and the undercoordinated Pt vertex sites (Supplementary Figs. 16, 17). The [$\Delta E_O^{(Vertex)}$ - $\Delta E_O^{Pt(Vertex)}$], defined as the difference between $\Delta E_O^{(Vertex)}$ of Pt-alloy and $\Delta E_O^{Pt(Vertex)}$ of Pt at vertex site, increases from 0.15 eV for fd-$Pt_{122}Ni_{25}$ alloy, to 0.21 eV for sd-$Pt_{122}Ni_{25}$ alloy, suggesting weaker Pt-O binding on sd-PtNi vertex sites. The weaker Pt-O binding on these vulnerable sites protects them and increases their stability under reaction conditions[28,42]. In addition, an even weaker Pt-O binding ([$\Delta E_O^{(Vertex)}$ - $\Delta E_O^{Pt(Vertex)}$] = 0.28 eV) was found on a $L1_0$-$Pt_{116}Ni_{31}$ structure (Figures. 2.19, 2.20) representing the more stable intermetallic phase, confirming this trend. Together, based on this experimental Sabatier plot, we can expect that Pt-alloy catalysts with large strain and AF tend

to reside on the right side of the plot showing better stability, while those sitting closer to the top of the right slope may exhibit simultaneous high activity and high stability.

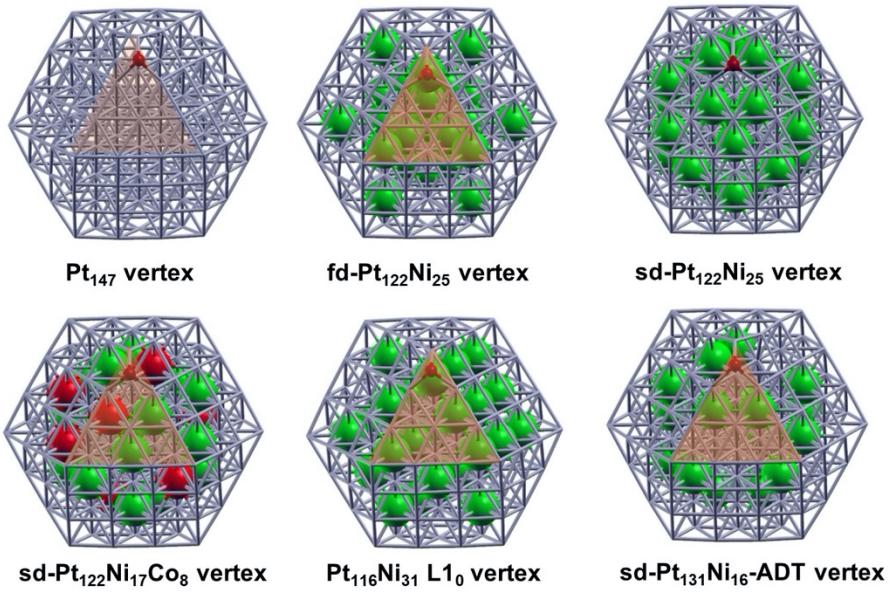

Figure 2.19. Schematic depiction of 147-atom cluster models and O-binding on their vertex sites.

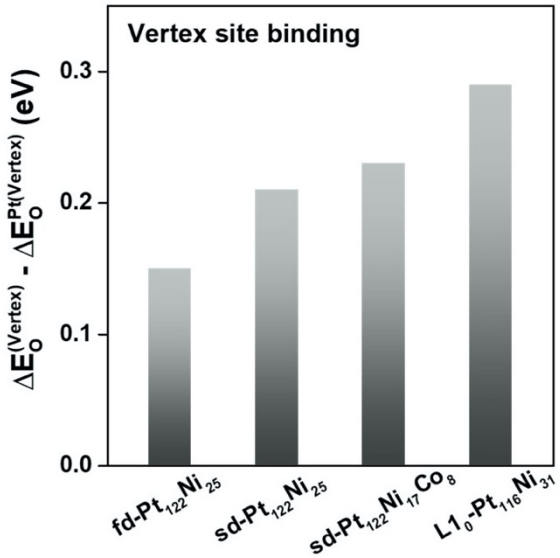

Figure 2.20. Vertex site O-binding energy calculation results. The difference between $\Delta E_O^{(Vertex)}$ of Pt-alloy clusters and $\Delta E_O^{Pt(Vertex)}$ of the pure Pt cluster on vertex site for fd-$Pt_{122}Ni_{25}$, sd-$Pt_{122}Ni_{25}$, sd-$Pt_{122}Ni_{17}Co_8$, and $L1_0$-$Pt_{116}Ni_{31}$ 147-atom cluster models.

Design of ORR catalyst with simultaneously high activity and stability

Taking a step further, we constructed a ternary sd-$Pt_{122}Ni_{17}Co_8$ model due to the higher chemical stability of ternary PtNiCo[16,43,44]. For sd-$Pt_{122}Ni_{17}Co_8$, our model predicted a [$\Delta E_O^{(111)}$ - $\Delta E_O^{Pt(111)}$] of 0.30 eV, with corresponding a BED value of 0.30, which sits closer to the optimal position of the calculated Sabatier plot (red cross points, Figure 2.10d) and demonstrates a better thermodynamic stability (calculated mixing energy of -15.11 eV) (Figure 2.18). Thus, we expected that sd-$Pt_{122}Ni_{17}Co_8$ should outperform the sd-$Pt_{122}Ni_{25}$, in terms of both ORR activity and stability.

We then synthesized concaved PtNiCo catalyst following a similar protocol established for sd-$Pt_{85}Ni_{15}$ and obtained PtNiCo catalysts with similar morphology and Pt composition, which is termed sd-$Pt_{84}Ni_{12}Co_4$ catalyst (Figures 2.21-2.25). As predicted, the sd-$Pt_{84}Ni_{12}Co_4$ showed Pt-L_3 XANES peak broadening (Figure 2.26a) and compressive strain (Figure 2.26b). Similar to sd-$Pt_{85}Ni_{15}$, the peak broadening (AF) and the concaved morphology of sd-$Pt_{84}Ni_{12}Co_4$ were maintained even after the 20,000 cycles of ADT (Figures. 2.26a-f). As predicted, sd-$Pt_{84}Ni_{12}Co_4$ demonstrated superior activity to sd-$Pt_{85}Ni_{15}$ (Figures. 2.26c,d). Specifically, sd-$Pt_{84}Ni_{12}Co_4$ showed an impressive SA of 10.7 ± 1.4 mA/cm^2 and MA of 7.1 ± 1.0 A/mg$_{Pt}$ at 0.9 V versus RHE, which is 28.9 times and 28.4 times those of Pt/C. Based on experimentally determined BED and the activity of sd-$Pt_{84}Ni_{12}Co_4$, we found that the sd-$Pt_{84}Ni_{12}Co_4$ indeed locates near the top right of the Sabatier plot (Figures. 2.26c). Significantly, the SA of the designed sd-$Pt_{84}Ni_{12}Co_4$ is highly competitive among the state-of-the-art Pt-based catalysts including Mo-doped Pt_3Ni[45] and state-of-the-art jagged Pt nanowires (J-PtNWs)[14] (Figures. 2.26d, g). More importantly, the sd-$Pt_{84}Ni_{12}Co_4$ also showed simultaneously exceptional stability with only 8% loss of ECSA, 5% loss in SA, and 12% loss of MA after the ADT (Figure. 2.26e), both superior to that of the sd-$Pt_{85}Ni_{15}$, as predicted. The composition of the sd-$Pt_{84}Ni_{12}Co_4$ stayed essentially unchanged after 20,000

cycles ADT (inset of Figure. 2.26e), and the concave morphology of sd-$Pt_{84}Ni_{12}Co_4$ was also largely maintained (Figure. 2.26f).

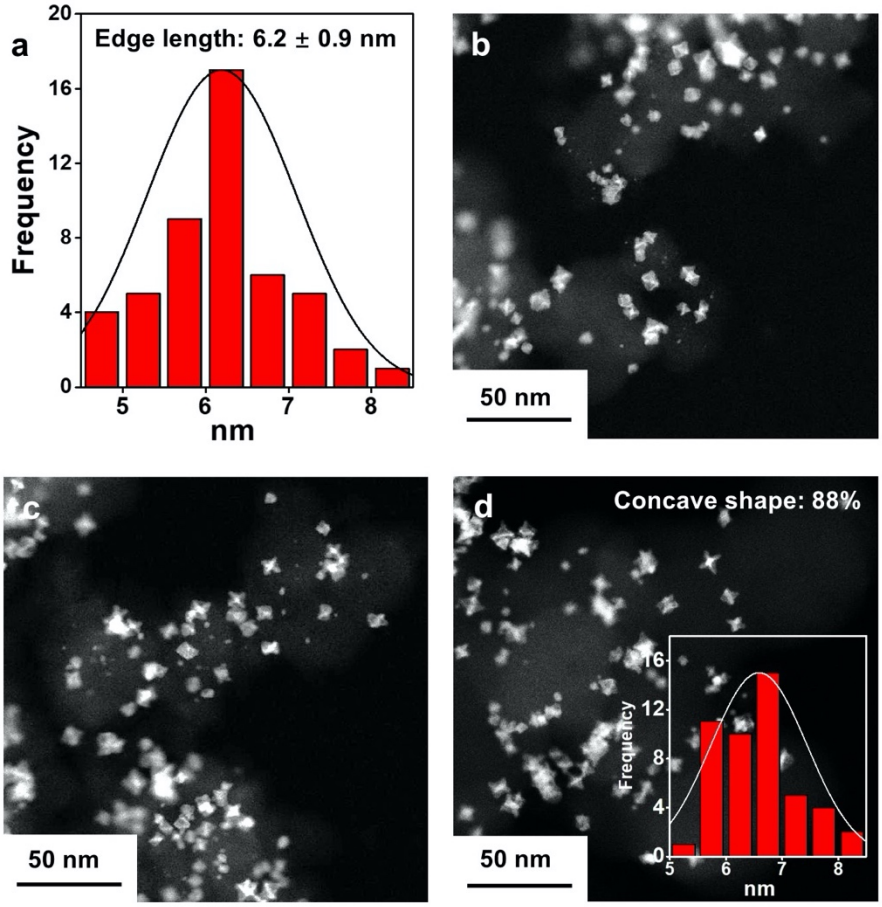

Figure 2.21. TEM analysis of sd-PtNiCo catalysts at different stages. (**a**) Octahedra size distribution of p-$Pt_{41}Ni_{54}Co_5$ catalysts. (**b-d**) Representative HAADF-STEM images for p-$Pt_{41}Ni_{54}Co_5$, sd-$Pt_{70}Ni_{26}Co_4$, and sd-$Pt_{84}Ni_{12}Co_4$ after activation, inset of panel (**d**) is the size distribution of sd-$Pt_{84}Ni_{12}Co_4$ after activation. The insets of panel (**d**) are the percentage of concave shape and the size distribution, respectively.

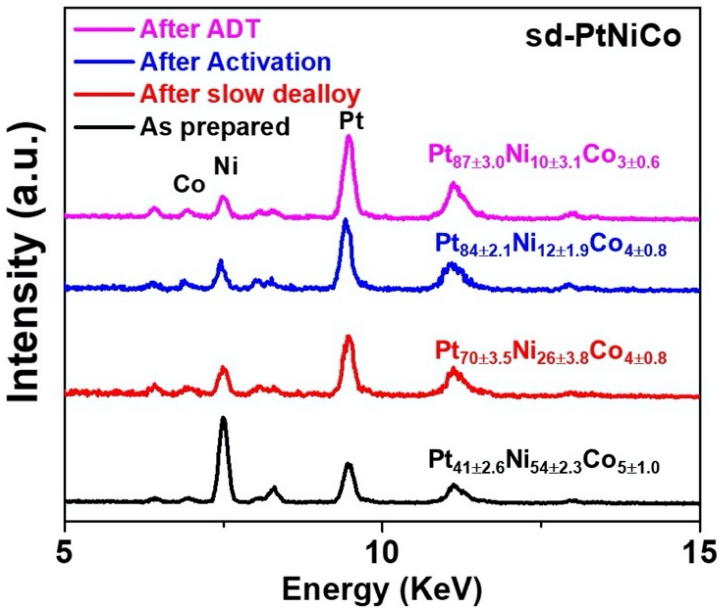

Figure 2.22. EDX composition analysis of sd-PtNiCo at different stages. Each stage corresponds to p-$Pt_{41}Ni_{54}Co_5$ (black), sd-$Pt_{70}Ni_{26}Co_4$ (red), and sd-$Pt_{84}Ni_{12}Co_4$ (blue), and sd-$Pt_{87}Ni_{10}Co_3$-ADT (pink), respectively.

Our proposed BED thus fully accounts for the experimentally observed ORR activities for sd-Pt-alloys and fd-Pt-alloys before and after ADT (Figure. 2.26c), which leads to an experimental Sabatier plot to predict the Pt-alloy activity (SA) based on the experimentally measurable value [-0.13Strain (%) + 0.1ΔAF]. On this experimental Sabatier plot, the sd-Pt-alloys started on the right slope before the ADT, and both were brought to the left slope after the ADT. During this process, the strain and the Pt-M coupling (the local coordination environment that contributed to the broadening of Pt L_3-edge *in-situ* XANES spectra) might work synergistically to preserve the activity of the Pt-alloys. Hence Pt-alloys with such feature may still maintain a $\Delta E_O^{(111)}$ closer to the optimal value despite the lattice relaxation during the long-term electrocatalytic reactions, exhibiting robust stability. This observation suggests that Pt-alloy catalysts whose BED lies on the right slope of the Sabatier plot, usually those with large strain and/or ΔAF, may exhibit better stability than those on the left.

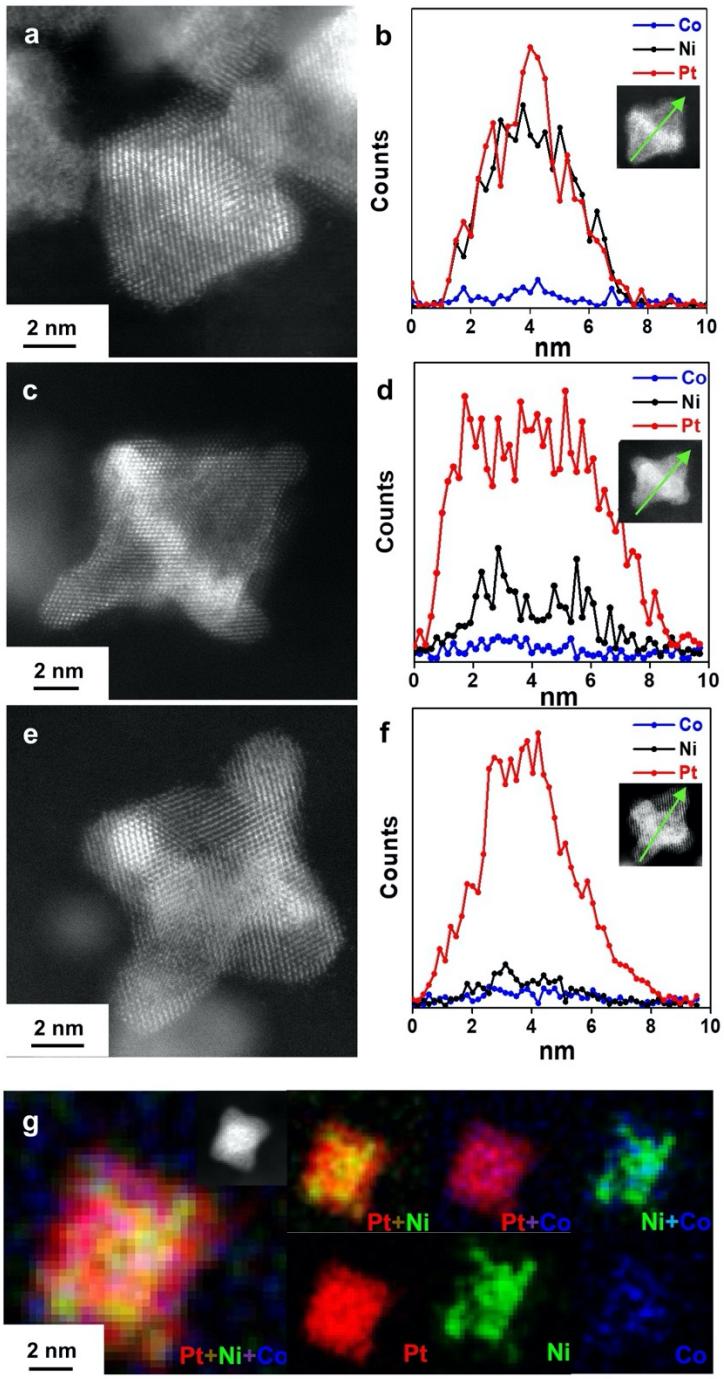

Figure 2.23. Representative HAADF-STEM images and EDX line-scan and mapping analysis for (**a**, **b**) p-$Pt_{41}Ni_{54}Co_5$ catalyst, (**c**, **d**) sd-$Pt_{70}Ni_{26}Co_4$ catalyst (after slow-dealloying in DMF), and (**e, f**) sd-$Pt_{84}Ni_{12}Co_4$ catalysts (after activation). The insets in (**b, d, f**) are the corresponding HAADF-STEM images. (**g**) EDX mapping results of sd-$Pt_{84}Ni_{12}Co_4$ catalyst.

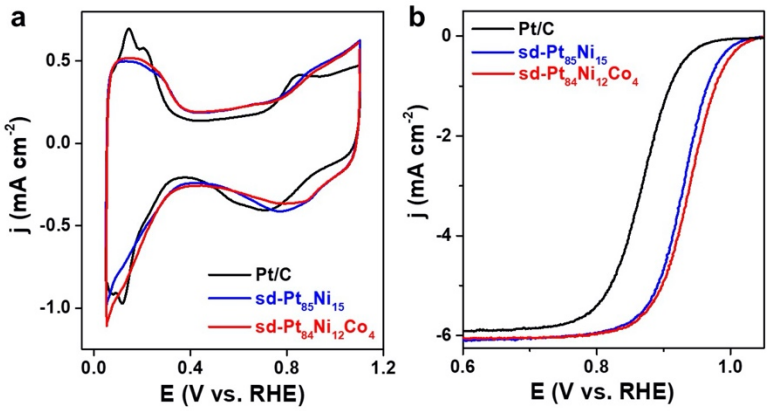

Figure 2.24. Electrochemical performance of sd-$Pt_{84}Ni_{12}Co_4$ catalysts in comparison with sd-$Pt_{85}Ni_{15}$ and commercial Pt/C catalysts. (**a**) CVs of sd-$Pt_{85}Ni_{15}$ (blue) and sd-$Pt_{84}Ni_{12}Co_4$ (red) versus commercial Pt/C (black) catalysts recorded at room temperature in N_2-purged 0.1 M $HClO_4$ solution at a sweep rate of 100 mV/s. (**b**) ORR polarization curves of sd-$Pt_{85}Ni_{15}$ (blue) and sd-$Pt_{84}Ni_{12}Co_4$ (red) in comparison to Pt/C (black) catalysts. The ORR tests were measured in O_2-purged 0.1 M $HClO_4$ solution at a sweep rate of 20 mV/s.

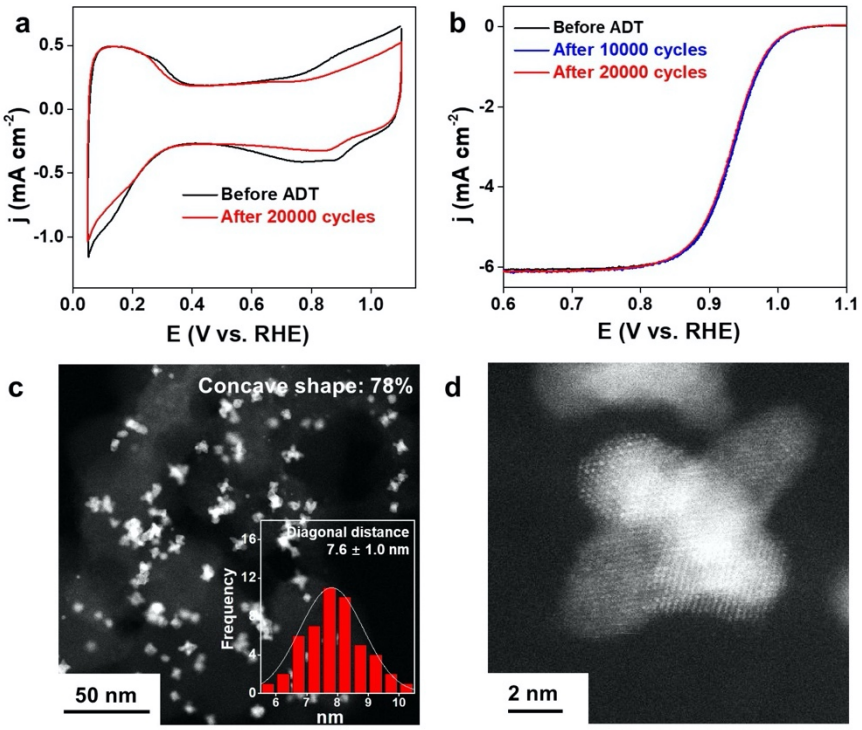

Figure 2.25. Electrochemical stability analysis of sd-$Pt_{84}Ni_{12}Co_4$ catalysts. (**a**) CV comparison before (black) and after 20,000 cycles ADT (red). (**b**) ORR polarization curves of sd-$Pt_{84}Ni_{12}Co_4$ catalysts before ADT (black), after 10,000 cycles ADT (blue), and after 20,000 cycles ADT (red). (**c**, **d**) Representative HAADF-STEM and high-resolution HAADF-STEM image of the sd-

$Pt_{87}Ni_{10}Co_3$-ADT after 20,000 cycles ADT. The insets of panel (**c**) are the percentage of concave shape and the size distribution, respectively.

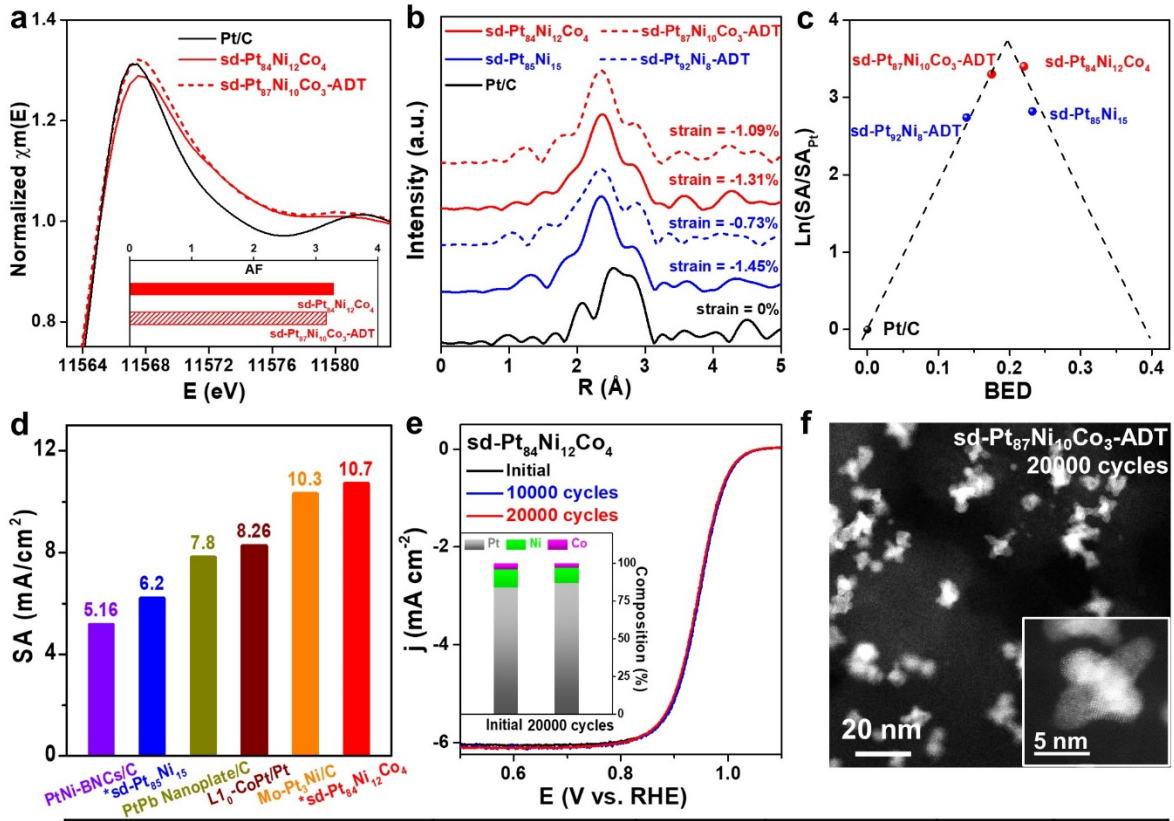

g

Catalyst	SA (mA/cm²)		ADT Cycles	SA Retention	ECSA (m²/g)	MA (A/mg)
	BOL	ADT				
sd-$Pt_{84}Ni_{12}Co_4$ (this work)	**10.7**	**10.1**	**20,000**	**95%**	**68**	**7.1**
sd-$Pt_{85}Ni_{15}$ (this work)	**6.2**	**5.6**	**20,000**	**91%**	**65**	**4.0**
fd-$Pt_{86}Ni_{14}$ (this work)	**4.0**	**2.1**	**20,000**	**53%**	**65**	**2.6**
PtNi-BNCs/C	5.16	5.17	50,000	100.2%	68.2	3.52
PtPb nanoplate/C	7.8	7	50,000	89%	55	4.3
Pt_3Ni/C nanoframes	8.4*	NA	10,000	NA	67.2	5.7
$L1_0$-CoPt/Pt	8.26	6.77	30,000	82%	27.3	2.26
J-PtNWs/C	11.5	10.8	6,000	94.5%	118	13.6

Figure 2.26. Experimentally validated sd-PtNiCo catalyst showing expected BED and simultaneously high activity and stability. (**a**) Pt L_3-edge *in-situ* XANES spectra of sd-$Pt_{84}Ni_{12}Co_4$ (red) and sd-$Pt_{87}Ni_{10}Co_3$-ADT (red-dashed) compared to Pt/C catalyst (black) collected at 0.54 V in O_2-saturated 0.1 M $HClO_4$ solution. The inset panel is the AF of concave sd-PtNiCo catalyst before and after ADT. (**b**) *In-situ* EXAFS spectra of sd-$Pt_{84}Ni_{12}Co_4$ (red), sd-$Pt_{87}Ni_{10}Co_3$-ADT (red-dashed), sd-$Pt_{85}Ni_{15}$ (blue), sd-$Pt_{92}Ni_8$-ADT (blue-dashed), and Pt/C (black). *In-situ* data were collected in an O_2-purged 0.1 M $HClO_4$ electrolyte at 0.54 V versus RHE. (**c**) The relationship between experimentally measured activity ($Ln(SA/SA_{Pt})$) and BED of sd-

$Pt_{84}Ni_{12}Co_4$, sd-$Pt_{87}Ni_{10}Co_3$-ADT, sd-$Pt_{85}Ni_{15}$, sd-$Pt_{92}Ni_8$-ADT, and Pt/C catalyst, showing a similar trend to simulation. The dashed line is adopted from reference[46] with BED replacing (ΔE_O - ΔE_O^{Pt}) in the X-axis. (**d**) Comparison of SAs at 0.9 V versus RHE, for *sd-$Pt_{84}Ni_{12}Co_4$, *sd-$Pt_{85}Ni_{15}$ from this work, and other state-of-the-art ORR catalysts: PtNi-BNCs/C[13], PtPb nanoplate/C[12], $L1_0$-CoPt/Pt[47], and Mo-Pt_3Ni/C[45]. (**e**) ORR polarization curves for the sd-$Pt_{84}Ni_{12}Co_4$ before ADT (black), after 10,000 cycles (blue), and after 20,000 cycles (red) of ADT between 0.6 and 1.0 V versus RHE, showing little loss in activity. Inset of panel **e** is the EDX-determined composition comparison before and after 20,000 cycles of ADT. (**f**) HAADF-STEM images of sd-$Pt_{87}Ni_{10}Co_3$-ADT after 20,000 cycles of ADT, inset panel is the high-resolution STEM image. (**g**) Performance of fd-$Pt_{86}Ni_{14}$, sd-$Pt_{85}Ni_{15}$, sd-$Pt_{84}Ni_{12}Co_4$ catalysts, in comparison to those in several representative works: PtNi-BNCs/C[13], PtPb nanoplate/C[12], Pt_3Ni/C nanoframes[48], $L1_0$-CoPt/Pt[47], and J-PtNWs/C[14]. All activities were compared at 0.9 V versus RHE. BOL: beginning of life, *: calculated based on reported data. NA: not available.

Universality of the descriptor

To examine the universality of the descriptor, we examined various Pt-alloy catalysts (see supplementary materials for the synthesis details) with different morphology, structure, and composition (Tables 2.2, 2.3, Figures 2.27-2.29). With the experimentally measured activity $Ln(SA_{Pt\text{-}alloy}/SA_{Pt/C})$ as the Y-axis, and the BED in place of ($\Delta E_O^{(111)}$ - $\Delta E_O^{Pt(111)}$) in the X-axis, we found that all examined catalysts fall nicely into the predicted Sabatier relation (Figure 2.30a). As shown in the plot, the Pt-based catalysts without XANES broadening (or a negligible ΔAF) all located at the left side of the Sabatier plot, including the previously reported J-PtNWs sitting near the top left of the plot (Figure 2.30a). The intermetallic Pt-alloy (extracted from Ref.[33]), the tetrahedral PtCuNi alloys (tetra-PtCuNi), and the annealed p-Pt-alloy (p-Pt-alloy-AN) all reside on the right slope of the Sabatier plot, showing considerable broadening in their Pt-L_3 XANES peak and a large strain. We expect that this BED can predict ORR activities for virtually all Pt-based catalysts without prior knowledge of the composition, morphology, or structure. We also expect this BED can be used to qualitatively predict the stability of Pt-alloy catalysts, based on

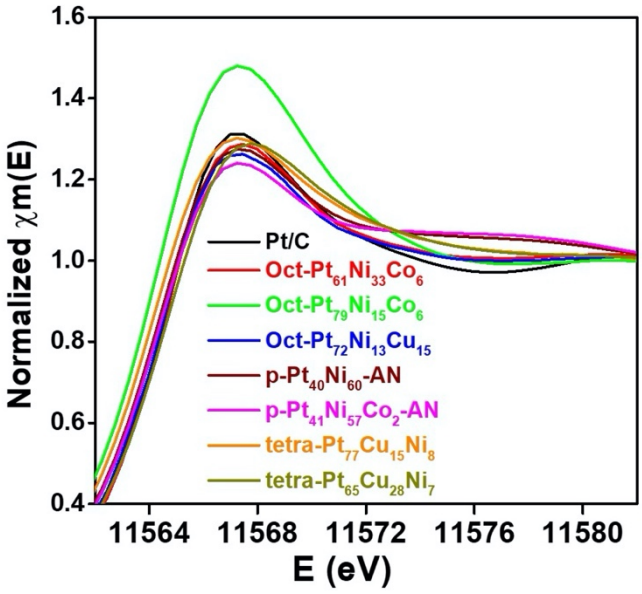

Figure 2.27. ***Ex-situ*** **experimental XANES spectra at the Pt L_3-edge of examined catalysts.** All samples were electrochemically activated in N_2-purged 0.1 M $HClO_4$ solution at a sweep rate of 100 mV/s from 0.05 to 1.1 V vs. RHE prior to XAS measurement.

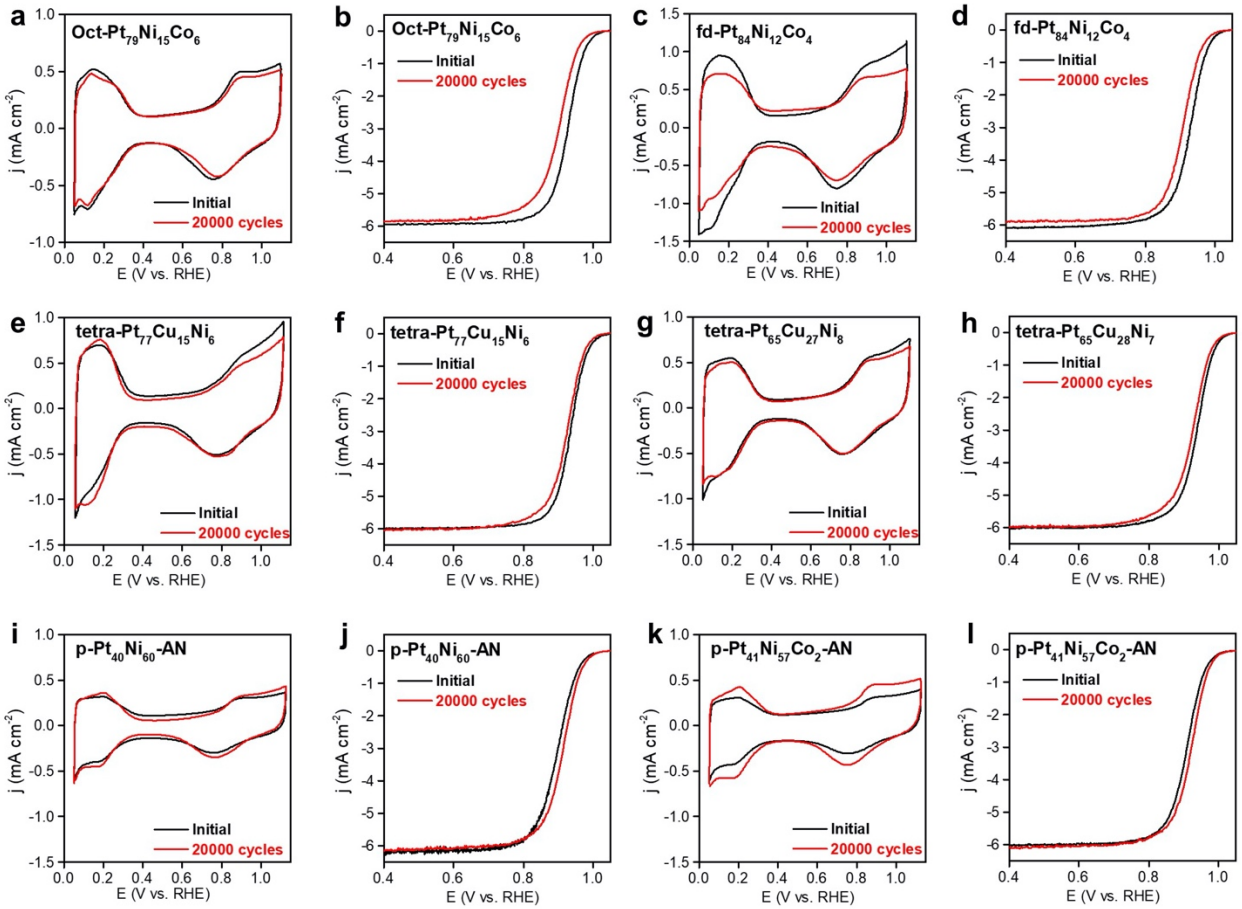

Figure 2.28. Representative CVs and ORR polarization curves before (black) and after 20,000 cycles of ADT (red) for (**a, b**) Oct-$Pt_{79}Ni_{15}Co_6$ catalyst (Pt loading: 7 μg/cm^2). (**c, d**) fd-$Pt_{84}Ni_{12}Co_4$ catalyst (Pt loading: 7.5 μg/cm^2), (**e, f**) tetra-$Pt_{77}Cu_{15}Ni_8$ catalyst (Pt loading: 7.5 μg/cm^2). (**g, h**) tetra-$Pt_{65}Cu_{27}Ni_8$ catalyst (Pt loading: 7.5 μg/cm^2), (**i, j**) p-$Pt_{40}Ni_{60}$-AN catalyst (Pt loading: 7.5 μg/cm^2), (**k, l**) p-$Pt_{41}Ni_{57}Co_2$-AN catalyst (Pt loading: 7.5 μg/cm^2). The ADT was performed between 0.6 to 1.0 V versus RHE at a sweep rate of 100 mV/s in 0.1 M O_2-saturated $HClO_4$.

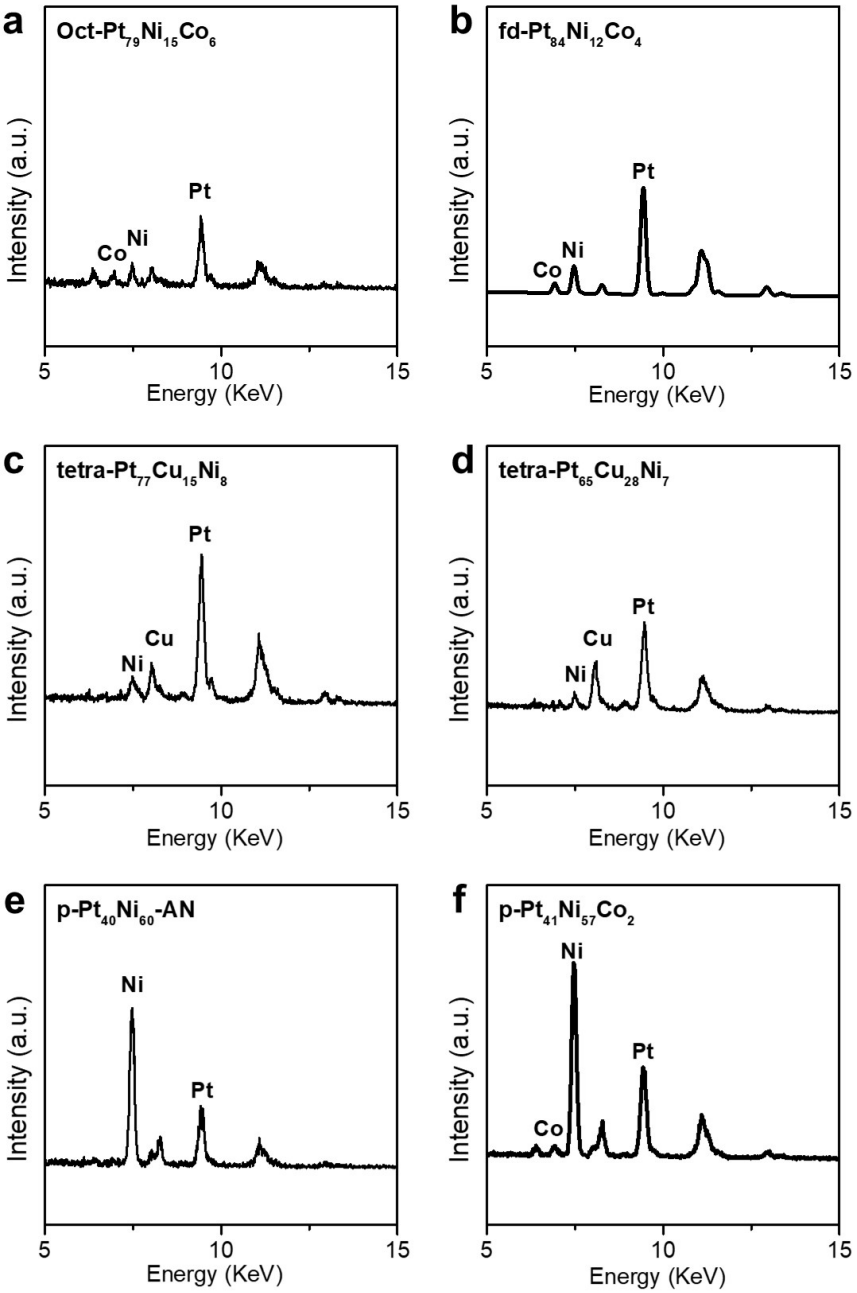

Figure 2.29. Representative EDX elemental analysis for (**a**) Oct-$Pt_{79}Ni_{15}Co_6$ catalyst. (**b**) fd-$Pt_{84}Ni_{12}Co_4$ catalyst. (**c**) tetra-$Pt_{77}Cu_{15}Ni_8$ catalyst. (**d**) tetra-$Pt_{65}Cu_{28}Ni_7$ catalyst. (**e**) p-$Pt_{40}Ni_{60}$-

AN catalyst. (**f**) p-$Pt_{41}Ni_{57}Co_2$-AN catalyst. All samples were electrochemically activated prior to EDX measurement.

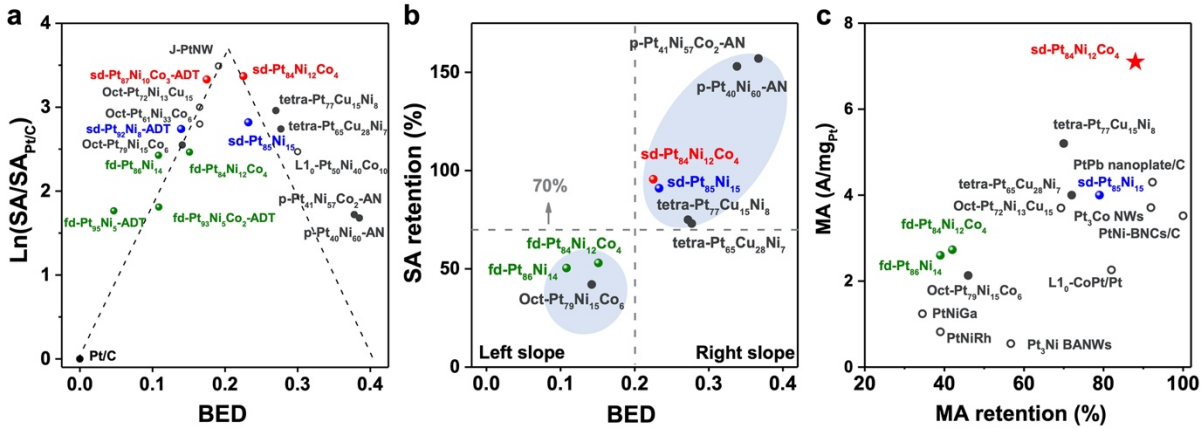

Figure 2.30. Experimentally validated Sabatier plot of Pt-alloy catalysts and stability analysis. (**a**) Experimental Sabatier plot of Pt-alloy catalysts. See supplementary materials for the preparation of tetra-PtCuNi, fd-PtNiCo, p-PtNi-AN, and p-PtNiCo-AN catalysts. Hollow circles represent catalysts reported in literature: L1$_0$-$Pt_{50}Ni_{40}Co_{10}$[33], J-PtNWs[14], Oct-$Pt_{72}Ni_{13}Cu_{15}$[49], Oct-$Pt_{61}Ni_{33}Co_6$ (composition was determined before activation)[44]. The dashed line is adopted from reference[46] with BED replacing (ΔE_O - ΔE_O^{Pt}) in the X-axis. (**b**) Comparison of SA retention for left-slope catalysts and right-slope catalysts after 20,000 cycles of ADT between 0.6 V and 1.0 V versus RHE at a sweep rate of 100 mV/s in O_2-saturated 0.1 M $HClO_4$. The vertical dashed line is the separation line of the left slope and right slope. (**c**) MA and MA retention of Pt-alloy catalysts (with at least 20,000 cycles of ADT), suggesting that sd-PtNiCo possesses both high MA and MA retention. Hollow circles represent catalysts reported in literature: PtPb nanoplate/C[12], PtNi-BNCs/C[13], L1$_0$-CoPt/Pt[47], Oct-$Pt_{72}Ni_{13}Cu_{15}$[49], Pt_3Ni BANWs[50], PtNiRh[51], PtNiGa[52], Pt_3Co NWs[53].

which side of the slope they reside. We hypothesize that similar to sd-PtNi and sd-PtNiCo, Pt-alloys locating on the right side of the experimental Sabatier plot may demonstrate higher stability than those on the left. We further investigated the stability (20,000 cycles of ADT) of the catalysts at the left slope and the right slope, respectively (Figure 2.30b). As expected, the catalysts locating on the right slope of the experimental Sabatier plot all showed an excellent SA retention above 70%, including sd-Pt-alloys, tetra-PtCuNi, and the annealed p-PtNi-AN and p-PtNiCo-AN.

Interestingly, the p-PtNi-AN and p-PtNiCo-AN located at the lower side of the right slope showed an even higher SA after ADT than at which it started (retention about 150%) (Figure 2.28), indicating that ADT decreased BED (and hence (ΔE_O - ΔE_O^{Pt})) and shifted the SA up the right side of the Sabatier plot. In contrast, those Pt-alloy catalysts located at the left slope usually showed a lower SA retention around 50%, consistent with the expectation. Therefore, the BED can capture the contributions from both the strain effect and Pt-M coupling effect to reflect the calculated oxygen binding (ΔE_O - ΔE_O^{Pt}) in Pt-alloy catalysts and can be used to predict both the activity and stability of ORR catalysts. We expected that the Pt-alloys located near the top of the right slope may present the most desirable ORR catalysts possessing both high SA and high stability, such as the sd-PtNiCo we designed in this study. Together with large and stable ECSA, the sd-PtNiCo showed simultaneous high MA of 7.1 ± 1.0 A/mg_{Pt} and MA retention of 88%, showing the optimal combination of activity and stability among the state-of-the-art ORR catalysts (Figure 2.30c). Importantly, the excellent ORR performance of sd-PtNiCo has also been realized in a membrane electrode assembly (MEA), suggesting its applicability in a practical fuel cell. The sd-PtNiCo exhibited a high MA of 0.67 ± 0.03 A/mg_{Pt} and considerable MA retention of 64% after 30,000 square wave cycles of accelerated stress tests (AST) at a cathode loading of 0.083 mg_{Pt}/cm^2, surpassing the DOE 2020 target[54] for MA (0.44 A/mg_{Pt}) and MA retention (> 60%) and low Pt loading (< 0.125 mg_{Pt}/cm^2) (Figure 2.31).

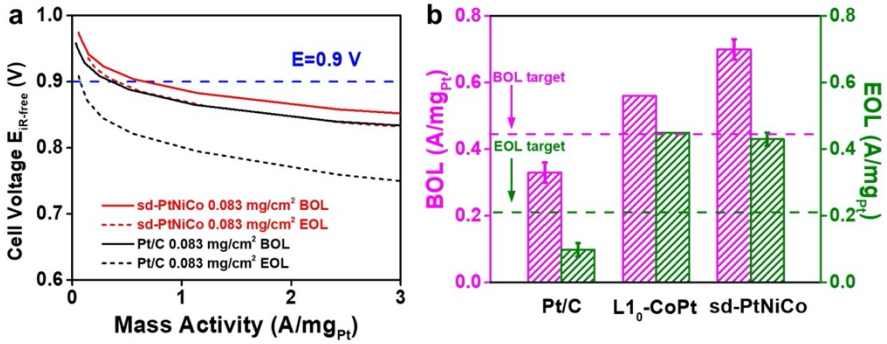

Figure 2.31. MEA performance of the sd-PtNiCo catalysts. (**a**) MAs of sd-PtNiCo (red lines) and Pt/C (black lines) tested by measuring the current at 0.9 V (iR-free) under 150 kPa_{abs} H_2/O_2 (80 ºC, 100% RH) with correction for H_2 crossover. (**b**) Comparison of MAs of sd-PtNiCo, Pt/C, and $L1_0$-CoPt[47]. BOL: beginning of life. EOL: end of life. Cathode Pt loading is 0.083 mg_{Pt}/cm^2 for both Pt/C and sd-PtNiCo, and 0.105 mg_{Pt}/cm^2 for $L1_0$-CoPt, respectively.

2.4 Conclusion

In summary, by comparing the structure-function relationship of concave octahedral sd-PtNi and fd-PtNi catalysts, we found that compressive strain and Pt-Ni coupling can be cumulatively captured with a binary experimental descriptor (BED = [-0.13Strain (%) + 0.1ΔAF]) that can be used in a way similar to the DFT-calculated ΔE_O to predict ORR activity of Pt-alloy catalysts. The BED works generally well to describe the experimentally observed ORR activities for Pt-alloy catalysts, confirming a Sabatier relation that can be used to predict both the activity and the stability of the Pt-based ORR catalysts. Based on this BED, we designed a sd-$Pt_{84}Ni_{12}Co_4$ catalyst residing near the top of the right leg of the Sabatier plot, which exhibited a simultaneously ultrahigh SA of 10.7 ± 1.4 mA/cm^2 and excellent stability showing only 8% loss of ECSA, 5% loss in SA and 12% loss of MA after 20,000 cycles of ADT. The high activity and stability of sd-PtNiCo catalysts have also been validated in MEA with both MA and stability surpassing US DOE set targets.

2.5 References

1. Strasser, P. *et al.* Lattice-strain control of the activity in dealloyed core–shell fuel cell catalysts. *Nat. Chem.* **2**, 454-460 (2010).

2. Escudero-Escribano, M. *et al.* Tuning the activity of Pt alloy electrocatalysts by means of the lanthanide contraction. *Science* **352**, 73-76 (2016).

3. Kitchin, J. R., Nørskov, J. K., Barteau, M. A. & Chen, J. G. Role of strain and ligand effects in the modification of the electronic and chemical properties of bimetallic surfaces. *Phys. Rev. Lett.* **93**, 156801 (2004).

4. Liu, Z., Zhao, Z., Peng, B., Duan, X. & Huang, Y. Beyond extended surfaces: understanding the oxygen reduction reaction on nanocatalysts. *J. Am. Chem. Soc.* **142**, 17812-17827 (2020).

5. Chen, Y., Cheng, T. & Goddard III, W. A. Atomistic explanation of the dramatically improved oxygen reduction reaction of jagged platinum nanowires, 50 times better than Pt. *J. Am. Chem. Soc.* **142**, 8625-8632 (2020).

6. Bligaard, T. & Nørskov, J. K. Ligand effects in heterogeneous catalysis and electrochemistry. *Electrochim. Acta* **52**, 5512-5516 (2007).

7. Calle-Vallejo, F. *et al.* Finding optimal surface sites on heterogeneous catalysts by counting nearest neighbors. *Science* **350**, 185 (2015).

8. Cui, C., Gan, L., Heggen, M., Rudi, S. & Strasser, P. Compositional segregation in shaped Pt alloy nanoparticles and their structural behaviour during electrocatalysis. *Nat. Mater.* **12**, 765-771 (2013).

9. Cherevko, S., Kulyk, N. & Mayrhofer, K. J. J. Durability of platinum-based fuel cell electrocatalysts: Dissolution of bulk and nanoscale platinum. *Nano Energy* **29**, 275-298 (2016).

10. Calle-Vallejo, F. *et al.* Why conclusions from platinum model surfaces do not necessarily lead to enhanced nanoparticle catalysts for the oxygen reduction reaction. *Chem. Sci.* **8**, 2283-2289 (2017).

11. Chattot, R. *et al.* Surface distortion as a unifying concept and descriptor in oxygen reduction reaction electrocatalysis. *Nat. Mater.* **17**, 827-833 (2018).

12. Bu, L. *et al.* Biaxially strained PtPb/Pt core/shell nanoplate boosts oxygen reduction catalysis. *Science* **354**, 1410 (2016).

13. Tian, X. *et al.* Engineering bunched Pt-Ni alloy nanocages for efficient oxygen reduction in practical fuel cells. *Science* **366**, 850 (2019).

14. Li, M. *et al.* Ultrafine jagged platinum nanowires enable ultrahigh mass activity for the oxygen reduction reaction. *Science* **354**, 1414 (2016).

15. Huang, J. *et al.* PtCuNi tetrahedra catalysts with tailored surfaces for efficient alcohol oxidation. *Nano Lett.* **19**, 5431-5436 (2019).

16. Huang, X. *et al.* A rational design of carbon-supported dispersive Pt-based octahedra as efficient oxygen reduction reaction catalysts. *Energy Environ. Sci.* **7**, 2957-2962 (2014).

17. Arruda, T. M., Shyam, B., Ziegelbauer, J. M., Mukerjee, S. & Ramaker, D. E. Investigation into the competitive and site-specific nature of anion adsorption on Pt using in situ X-ray absorption spectroscopy. *J. Phys. Chem. C* **112**, 18087-18097 (2008).

18. Jia, Q. *et al.* Activity descriptor identification for oxygen reduction on Platinum-based bimetallic nanoparticles: *in situ* observation of the linear composition–strain–activity relationship. *ACS Nano* **9**, 387-400 (2015).

19. Newville, M. IFEFFIT: interactive XAFS analysis and FEFF fitting. *J Synchrotron Radiat* **8**, 322-324 (2001).

20. Ravel, B. & Newville, M. ATHENA, ARTEMIS, HEPHAESTUS: data analysis for X-ray absorption spectroscopy using IFEFFIT. *J. Synchrotron Radiat.* **12**, 537-541 (2005).

21. Newville, M., Līviņš, P., Yacoby, Y., Rehr, J. J. & Stern, E. A. Near-edge x-ray-absorption fine structure of Pb: A comparison of theory and experiment. *Phys. Rev. B* **47**, 14126-14131 (1993).

22. Ankudinov, A. L., Ravel, B., Rehr, J. J. & Conradson, S. D. Real-space multiple-scattering calculation and interpretation of x-ray-absorption near-edge structure. *Phys. Rev. B* **58**, 7565-7576 (1998).

23. Mattheiss, L. F. Energy bands for solid argon. *Phys. Rev.* **133**, A1399-A1403 (1964).

24. Giannozzi, P. *et al.* QUANTUM ESPRESSO: a modular and open-source software project for quantum simulations of materials. *J. Condens. Matter Phys.* **21**, 395502 (2009).

25. Perdew, J. P., Burke, K. & Ernzerhof, M. Generalized gradient approximation made simple. *Phys. Rev. Lett.* **77**, 3865-3868 (1996).

26. Vanderbilt, D. Soft self-consistent pseudopotentials in a generalized eigenvalue formalism. *Phys. Rev. B* **41**, 7892-7895 (1990).

27. Barcaro, G., Sementa, L. & Fortunelli, A. A grouping approach to homotop global optimization in alloy nanoparticles. *Phys. Chem. Chem. Phys.* **16**, 24256-24265 (2014).

28. Jennings, P. C., Aleksandrov, H. A., Neyman, K. M. & Johnston, R. L. A DFT study of oxygen dissociation on platinum based nanoparticles. *Nanoscale* **6**, 1153-1165 (2014).

29. Zhang, C., Hwang, S. Y. & Peng, Z. Size-dependent oxygen reduction property of octahedral Pt–Ni nanoparticle electrocatalysts. *J. Mater. Chem. A* **2**, 19778-19787 (2014).

30. Wang, C. *et al.* Correlation between surface chemistry and electrocatalytic properties of monodisperse Pt_xNi_{1-x} Nanoparticles. *Adv. Funct. Mater.* **21**, 147-152 (2011).

31. Fortunelli, A. *et al.* The atomistic origin of the extraordinary oxygen reduction activity of Pt_3Ni_7 fuel cell catalysts. *Chem. Sci.* **6**, 3915-3925 (2015).

32. Gong, M. *et al.* Optimizing PtFe intermetallics for oxygen reduction reaction: from DFT screening to in situ XAFS characterization. *Nanoscale* **11**, 20301-20306 (2019).

33. Wang, T. *et al.* Sub-6 nm fully ordered $L1_0$-Pt–Ni–Co nanoparticles enhance oxygen reduction via Co doping induced ferromagnetism enhancement and optimized surface strain. *Adv. Energy Mater.* **9**, 1803771 (2019).

34. Dutta, I. *et al.* Electrochemical and structural study of a chemically dealloyed PtCu oxygen reduction catalyst. *J. Phys. Chem. C* **114**, 16309-16320 (2010).

35. Hwang, B. J. *et al.* An investigation of structure−catalytic activity relationship for Pt−Co/C bimetallic nanoparticles toward the oxygenreduction reaction. *J. Phys. Chem. C* **111**, 15267-15276 (2007).

36. Moraweck, B., Renouprez, A. J., Hlil, E. K. & Baudoing-Savois, R. Alloying effects on x-ray absorption edges in nickel-platinum single crystals. *J. Phys. Chem.* **97**, 4288-4292 (1993).

37. Hlil, E. K., BaudoingSavois, R., Moraweck, B. & Renouprez, A. J. X-ray absorption edges in platinum-based alloys. 2. influence of ordering and of the nature of the second metal. *J. Phys. Chem.* **100**, 3102-3107 (1996).

38. Chen, J. *et al.* Elucidating the many-body effect and anomalous Pt and Ni core level shifts in X-ray photoelectron spectroscopy of Pt–Ni alloys. *J. Phys. Chem. C* **124**, 2313-2318 (2020).

39. Mukerjee, S., Srinivasan, S., Soriaga, M. P. & Mcbreen, J. Role of structural and electronic-properties of Pt and Pt alloys on electrocatalysis of oxygen reduction: an *in-situ* XANES and EXAFS investigation. *J. Electrochem. Soc.* **142**, 1409-1422 (1995).

40. Rehr, J. J., Kas, J. J., Vila, F. D., Prange, M. P. & Jorissen, K. Parameter-free calculations of X-ray spectra with FEFF9. *Phys. Chem. Chem. Phys.* **12**, 5503-5513 (2010).

41. Pápai, Z. & Pap, T. L. Analysis of peak asymmetry in chromatography. *J. Chromatogr. A* **953**, 31-38 (2002).

42. Hu, J. *et al.* Increasing stability and activity of core–shell catalysts by preferential segregation of oxide on edges and vertexes: oxygen reduction on Ti–Au@Pt/C. *J. Am. Chem. Soc.* **138**, 9294-9300 (2016).

43. Arán-Ais, R. M. *et al.* Elemental anisotropic growth and atomic-scale structure of shape-controlled octahedral Pt–Ni–Co alloy nanocatalysts. *Nano Lett.* **15**, 7473-7480 (2015).

44. Zhao, Z. *et al.* Composition tunable ternary Pt-Ni-Co octahedra for optimized oxygen reduction activity. *ChemComm* **52**, 11215-11218 (2016).

45. Huang, X. *et al.* High-performance transition metal–doped Pt_3Ni octahedra for oxygen reduction reaction. *Science* **348**, 1230 (2015).

46. Greeley, J. *et al.* Alloys of platinum and early transition metals as oxygen reduction electrocatalysts. *Nat. Chem.* **1**, 552-556 (2009).

47. Li, J. *et al.* Hard-magnet $L1_0$-CoPt nanoparticles advance fuel cell catalysis. *Joule* **3**, 124-135 (2019).

48. Chen, C. *et al.* Highly crystalline multimetallic nanoframes with three-dimensional electrocatalytic surfaces. *Science* **343**, 1339 (2014).

49. Cao, L. *et al.* Differential surface elemental distribution leads to significantly enhanced stability of PtNi-based ORR catalysts. *Matter* **1**, 1567-1580 (2019).

50. Gong, M. *et al.* One-nanometer-thick Pt_3Ni bimetallic alloy nanowires advanced oxygen reduction reaction: integrating multiple advantages into one catalyst. *ACS Catal.* **9**, 4488-4494 (2019).

51. Beermann, V. *et al.* Rh-doped Pt–Ni octahedral nanoparticles: understanding the correlation between elemental distribution, oxygen reduction reaction, and shape stability. *Nano Lett.* **16**, 1719-1725 (2016).

52. Lim, J. *et al.* Ga–doped Pt–Ni octahedral nanoparticles as a highly active and durable electrocatalyst for oxygen reduction reaction. *Nano Lett.* **18**, 2450-2458 (2018).

53. Bu, L. *et al.* Surface engineering of hierarchical platinum-cobalt nanowires for efficient electrocatalysis. *Nat. Commun.* **7**, 11850 (2016).

54. DRIVE, U. S. *Fuel Cell Technical Team Roadmap*, <https://www.energy.gov/sites/prod/files/2017/11/f46/FCTT_Roadmap_Nov_2017_FINAL.pdf> (2017).

Chapter 3. Multifunctional PtCuNi tetrahedra catalysts with tailored surfaces for efficient alcohol oxidation

3.1 Introduction

With the possibility of using non-PGM catalysts for the cathodic ORR reaction in basic electrolytes, the demand of using precious-metal-based (*e.g.*, Pt-based) catalyst to drive the methanol oxidation reaction (MOR) or ethanol oxidation reaction (EOR) becomes a critical cost issue for direct methanol/ethanol fuel cells (DMFCs/DEFCs). Thus, it is highly desirable to improve the activity and stability of Pt-based catalysts for MOR/EOR in basic conditions. In particular, a high mass activity (MA) of Pt is essential for reducing Pt usage in DMFCs/DEFCs. Common limitations of Pt and Pt-group metals in base arise from the fact that they are generally inefficient in dissociating/activating water[1]. It has been suggested that surface adsorbed hydroxyl (OH_{ad}) species can assist the carbon monoxide (CO) oxidation[2,3], which is a rate-determining step for MOR/EOR[4,5]. Pt surface cannot adsorb hydroxyl (OH_{ad}) species effectively due to their low oxophilicity, which limits the SA towards MOR/EOR in the base. To facilitate OH_{ad} adsorption and water dissociation, the surface of Pt-group metals have been paired with transition metal hydroxide or reduced graphene oxide (rGO) in the vicinity, which showed significant improvement on SA in basic conditions [6,7]. For example, Liu et al.[8] and Ren et al.[9] combined rGO with Pt alloys, and showed that it brought ~2 to 6 times enhancement in SA compared to those without rGO for EOR. Lu et al.[10] found that surface Ni on PtNi alloy can boost SA ~2 times compared to commercial Pt/C. Chen et al[11] combine Ni and P surface modification on PdNi which could boost the EOR MA up to 4.95 A/mg_{Pd}. Jiang et al[12] synthesized ordered PdCu with Ni/Co which showed ~8 times enhancement of MA compared to Pd/C towards EOR. Thus, the surface decoration with transition metals can significantly boost the SA of Pt towards alcohol oxidation reaction. However,

such decorations generally block surface-active Pt sites, thus reducing the ECSA and the overall MA[6]. This represents a dilemma that high ECSA and surface modification are mutually exclusive in improving MA to some extent. Therefore, it is more desirable to achieve high SA based on high ECSA.

In the previous chapter, we designed the core-shell PtCuNi tetrahedra for ORR and the experimental Sabatier plot. In this chapter, we further elaborated on the preparation of these unique catalysts. In addition, we tuned the surface composition core-shell PtCuNi tetrahedra to explore their multifunctions, which can be potentially used on DMFCs/DEFCs. The optimal catalyst with a composition of $Pt_{56}Cu_{28}Ni_{16}$ shows a MOR and EOR SA of 14.0 ± 1.0 mA/cm^2 and 11.2 ± 1.0 mA/cm^2, respectively; and MA of 7.0 ± 0.5A/mg$_{Pt}$ and 5.6 ± 0.6 A/mg$_{Pt}$ for the MOR and EOR, respectively.

3.2 Experimental methods

Materials and chemicals

Platinum(II) acetylacetonate ($Pt(acac)_2$, 97%), nickel(II) acetylacetonate ($Ni(acac)_2$, 95%), copper (II) acetylacetonate ($Cu(acac)_2$, 97%), glucose, perchloric acid ($HClO_4$, 70%, PPT Grade), oleylamine [OAm; $CH_3(CH_2)_7CH{=}CH(CH_2)_7CH_2NH_2$, >70%], 1-octadecene [ODE; $CH_2{=}CH(CH_2)_{15}CH_3$; technical grade, >90%], were all purchased from Sigma-Aldrich. Commercial Pt/C catalyst (20 wt% Pt, and particle size 2 to 5 nm) were purchased from Alfa Aesar. Cyclohexane (C_6H_{12}; analytical reagent, >99.5%), ethanol (200 proof) were obtained from EMD Millipore, and Decon, respectively. All reagents were used as received without further purification. Carbon black (Vulcan XC-72) was received from Carbot Corporation and annealed in 280 ℃ air

before used. The deionized water (18 MΩ/cm) was obtained from an ultra-pure purification system (Milli-Q advantage A10).

Synthesis of of CS-PtCuNi tetrahedra

In a typical preparation of CS-$Pt_{56}Cu_{28}Ni_{16}$, $Pt(acac)_2$ (20 mg), $Cu(acac)_2$ (6 mg), $Ni(acac)_2$ (6 mg), Glucose (135 mg), OAm (3 ml), and ODE (2 ml) were added into a vial (volume, 35 ml). After the vial had been capped, the mixture was ultrasonicated for around 1 hour. The resulting homogeneous mixture was then purged with carbon monoxide (CO) for 5 minutes and heated from room temperature to 170°C in around 0.5 hours and kept at 170°C for 12 hours in an oil bath with stirring. After cooling to room temperature, the colloidal products were collected by centrifugation and washed with cyclohexane/ethanol (v/v = 1:5) mixture two times. For the syntheses of CS-$Pt_{64}Cu_{34}$ tetrahedra and CS-$Pt_{42}Cu_{20}Ni_{48}$tetrahedra, all the conditions were similar to those of CS-$Pt_{56}Cu_{28}Ni_{16}$ except by adding 0 and 12 mg $Ni(acac)_2$.

The as-prepared CS-PtCuNi tetrahedra were suspended in 20 mL cyclohexane/ethanol (v/v = 1:1) mixture. To load the sample on to carbon black, 20 mg of carbon black was added and sonicated for 2 hours. The resulting CS-PtCuNi tetrahedra/C catalysts were collected by centrifugation and cleaned with cyclohexane/ethanol mixture, placed in an alumina boat and annealed at 130°C for 6 hours in Ar with a flow rate of 100 sccm in a home-build tube furnace to dry and get rid of the surfactant.

Structure and composition characterization

Powder X-ray diffraction (XRD) patterns were collected on a Panalytical X'Pert Pro X-ray Powder Diffractometer with Cu-Kα radiation. X-ray photoelectron spectroscopy (XPS) tests were carried out on a Kratos AXIS Ultra DLD spectrometer. Low magnification Transmission electron microscopy (TEM) images were taken on a FEI T12 operated at 120 kV. High-resolution TEM

images (HRTEM), energy-dispersive X-ray spectroscopy (EDS) line-scan file, and the high-angle annular dark-field scanning transmission electron microscope (HAADF-STEM) images were taken on Titan S/TEM (FEI) and JEM-ARM300F Grand ARM Transmission Electron Microscope operated at 300 kV were performed on aberration-corrected TEM. TEM samples were prepared by dropping ethanol dispersion of catalysts onto carbon-coated Aluminum TEM grids. The elementary concentration of catalysts was determined by the inductively coupled plasma atomic emission spectroscopy (ICP-AES, Shimadzu ICPE-9000). The Pt loading is determined by the catalyst before electrochemical ink preparation.

Electrochemical measurement

A three-electrode cell system was used to conduct all electrochemical tests. The working electrode was a glassy carbon rotating disk electrode (RDE) with a 0.196 cm^2 glassy carbon geometry area from Pine Instruments. The counter and reference electrodes are Pt coil and Hg/HgO reference electrode was used as respectively. Pt loadings were 5.1 $\mu g/cm^2$ for all samples. Cyclic voltammetry (CV) activations were performed in N_2-saturated 1 M KOH electrolyte with a potential scan rate of 100 mV/s. Methanol was added into the electrolyte and controlled to 1 M as the reactant for MOR. Electrochemical active surface area (ECSA) in the acid electrolyte was determined in N_2-saturated 0.1 M $HClO_4$ electrolyte with a potential scan rate of 100 mV/s. ECSA determined by hydrogen underpotential deposition (H_{upd}) was calculated by integrating hydrogen adsorption charge on CV curve by taking a value of 210 $\mu C/cm^2$ for the adsorption of a hydrogen monolayer. Double-layer correction was also applied. For the CO stripping voltammetry measurements, working electrodes were firstly immersed in a CO-saturated 1M KOH solution for 40 s, and then the CO stripping voltammetry was tested between 0.05 to 1.1 V vs. the reverse hydrogen electrode (RHE) at a sweep rate of 25 mV/s.

3.3 Results and discussion

Structure of core-shell (CS) tetrahedral PtCuNi catalysts.

The synthesized CS-$Pt_{66}Cu_{34}$, CS-$Pt_{56}Cu_{28}Ni_{16}$, and CS-$Pt_{42}Cu_{20}Ni_{38}$ nanocrystals show primarily tetrahedral morphology and display an average edge length of 5.9 ± 1.1 nm, 5.7 ± 1.1 nm, and 6.1 ± 1 nm, respectively (Figure 3.1) (CS: core-shell). The average (111) lattice spacings are 0.219 nm, 0.218 nm, and 0.216 nm for CS-$Pt_{66}Cu_{34}$, CS-$Pt_{56}Cu_{28}Ni_{16}$, and CS-$Pt_{42}Cu_{20}Ni_{38}$, respectively (Figures 3.2, 3.3) calculated based on the fast Fourier transform (FFT). More importantly, the energy dispersion x-ray spectroscopy (EDS) mapping results show that a Cu-rich core and Pt-rich or Pt/Ni-rich shell configuration with a shell thickness of ~1 nm (Figures 3.2, 3.3). We further carried out a time-dependent growth experiment for typical CS-$Pt_{56}Cu_{28}Ni_{16}$ (Figures 3.4, 3.5). Notably, we observed that the initial nanocrystal has an average composition of $Pt_{31}Cu_{69}$ without Ni present, confirming faster Cu reduction than Pt and Ni. During the latter stage of growth, the composition of Cu decreases with increasing Pt and Ni, which is consistent with EDS results.

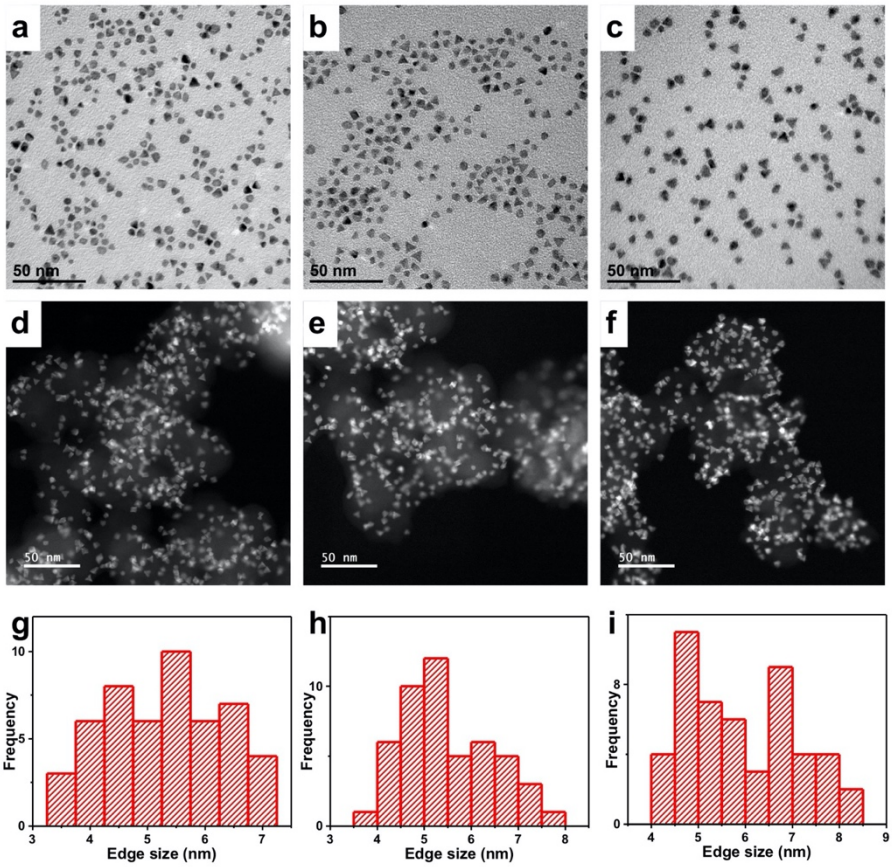

Figure 3.1. Low magnification, HAADF STEM images and size distribution of tetrahedral nanoparticles (**a, d** and **g**) CS-$Pt_{66}Cu_{34}$, (**b, e** and **h**) CS-$Pt_{56}Cu_{28}Ni_{16}$ and (**c, f** and **i**) CS-$Pt_{42}Cu_{20}Ni_{38}$.

Composition analysis clearly shows that Cu has a much higher composition in the core than the shell and Pt/Ni has a higher composition in the shell (Figure 3.6a-c). Cores of CS-$Pt_{66}Cu_{34}$, CS-$Pt_{56}Cu_{28}Ni_{16}$, and CS-$Pt_{42}Cu_{20}Ni_{38}$ have average compositions of $Pt_{39}Cu_{61}$, $Pt_{38}Cu_{56}Ni_{6}$, and $Pt_{30}Cu_{57}Ni_{13}$, respectively (Figure 3.6d-f). The near-surface (~1 nm) composition for CS-$Pt_{66}Cu_{34}$, CS-$Pt_{56}Cu_{28}Ni_{16}$, and CS-$Pt_{42}Cu_{20}Ni_{38}$ are $Pt_{77}Cu_{23}$, $Pt_{75}Cu_{14}Ni_{11,}$ and $Pt_{41}Cu_{13}Ni_{46}$, respectively (Figures 3.6a-c, 3.7), which further indicated the core-shell structure.

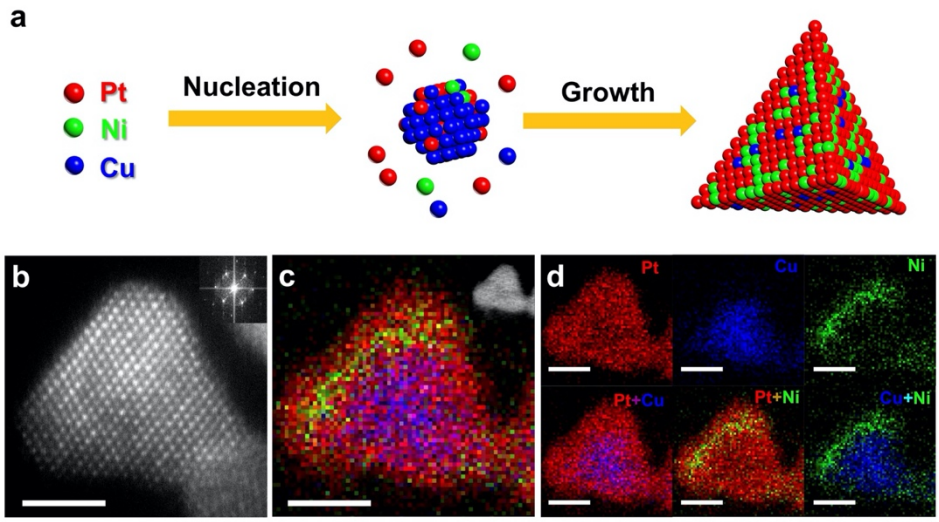

Figure 3.2. Schematic illustration for the synthesis of typical CS-PtCuNi tetrahedra (**a**). The first step represents faster Cu nucleation than Pt and Ni. The second step represents further Pt, Cu, Ni deposition. HAADF STEM images of tetrahedral nanoparticles (**b**) CS-$Pt_{56}Cu_{28}Ni_{16}$. Inset images in panels (**b**) is corresponding FFT image. EDS mapping of tetrahedral nanoparticle (**c**) CS-$Pt_{56}Cu_{28}Ni_{16}$. Inset images in panels (**c**) are corresponding HAADF STEM images of mapped nanoparticles. (**d**) EDS maps of individual or combinations of elements shown in (**c**). All scale bars are 2 nm.

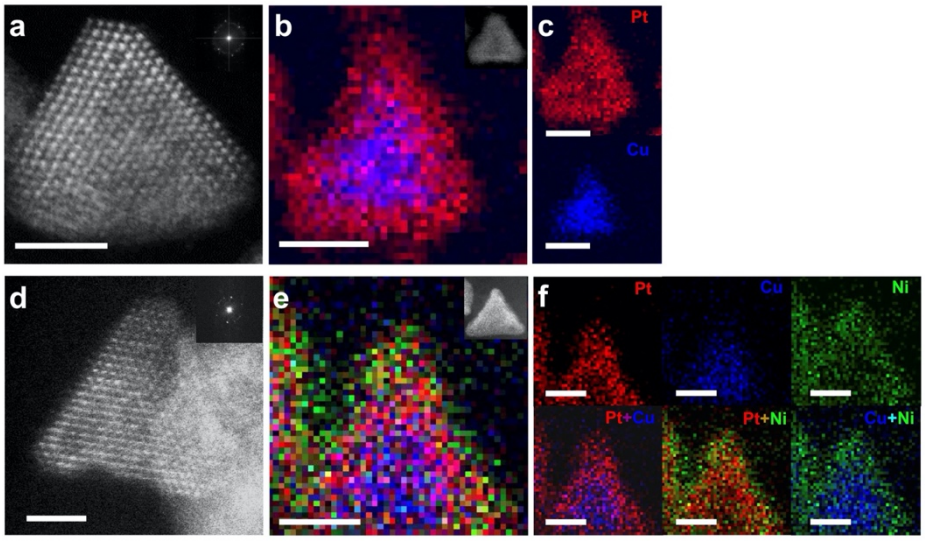

Figure 3.3. HAADF STEM images of tetrahedral nanoparticles (**a**) CS-$Pt_{66}Cu_{34}$ and (**d**) CS-$Pt_{42}Cu_{20}Ni_{38}$. Inset images in panels (**a**) and (**d**) are corresponding FFT image. EDS mapping of tetrahedral nanoparticles (**b**) CS-$Pt_{66}Cu_{34}$ and (**e**) CS-$Pt_{42}Cu_{20}Ni_{38}$. Inset images in panels (**b**) and (**e**) are corresponding HAADF STEM images of mapped nanoparticles. (**c** and **f**) EDS maps of individual or combinations of elements shown in (**b**) and (**e**), respectively. Scale bars are all 2 nm.

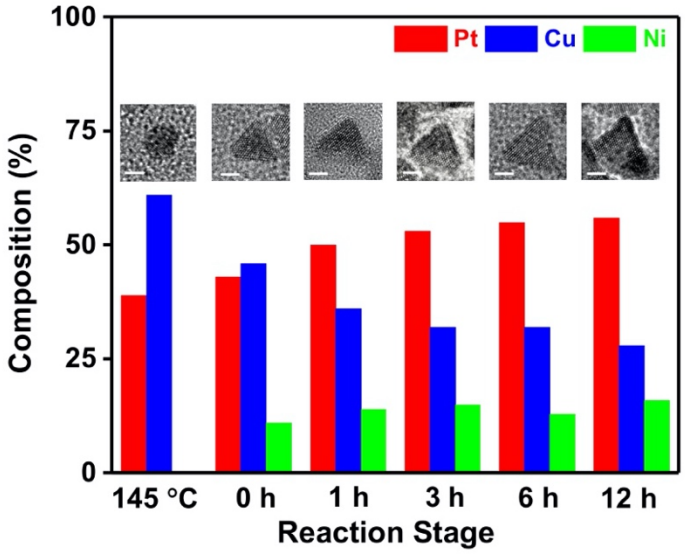

Figure 3.4. Composition and representative morphology changes of CS-$Pt_{56}Cu_{28}Ni_{16}$ at different reaction stage. All scale bars are 2 nm.

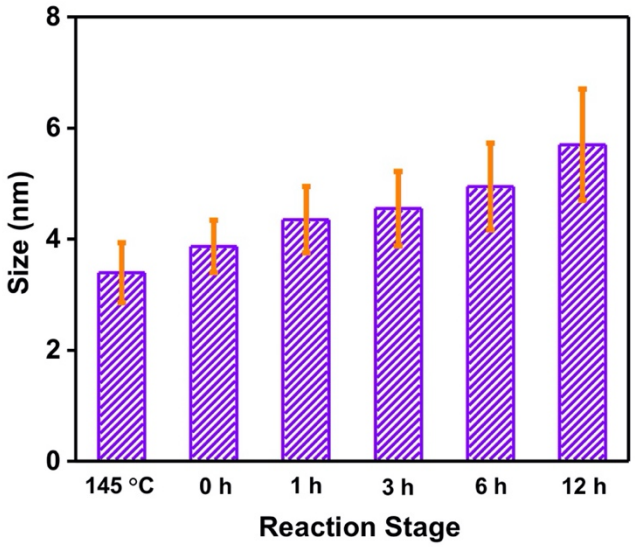

Figure 3.5. Composition of CS-$Pt_{56}Cu_{28}Ni_{16}$ at different reaction stages.

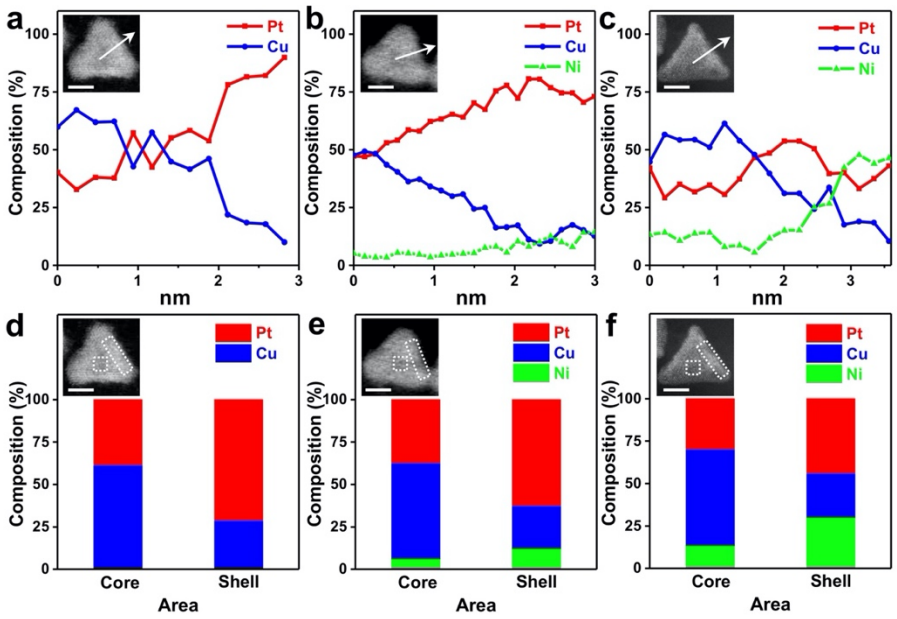

Figure 3.6. Composition variation from the core to shell based on the EDS line scan composition profiles analysis of (**a**) CS-$Pt_{66}Cu_{34}$, (**b**) CS-$Pt_{56}Cu_{28}Ni_{16}$ and (**c**) CS-$Pt_{42}Cu_{20}Ni_{38}$. The EDS composition comparisons between core area and shell area for (**d**) CS-$Pt_{66}Cu_{34}$, (**e**) CS-$Pt_{56}Cu_{28}Ni_{16}$ and (**f**) CS-$Pt_{42}Cu_{20}Ni_{38}$. All scale bars are 2 nm.

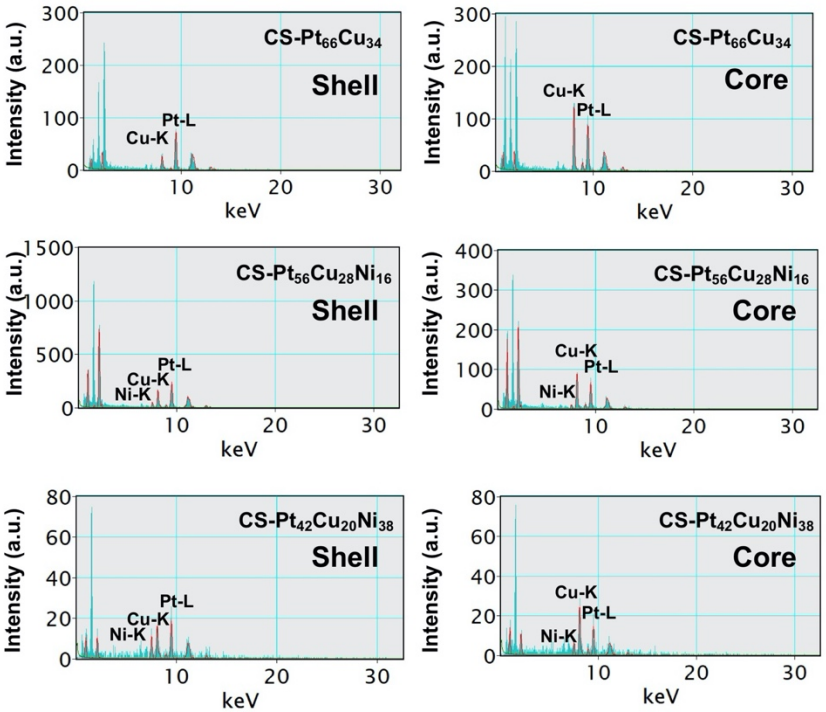

Figure 3.7. Energy dispersion X-ray spectroscopy (EDS) composition analysis for core area and shell area in Figure 3.6.

Methanol oxidation reaction (MOR) and ethanol oxidation reaction (EOR) performance

To evaluate the electrocatalytic performance of catalysts, we first used cyclic voltammetry (CV) in N_2-saturated 1 M KOH solution (0.05 V to 1.1 V *vs.* RHE) (RHE: reversible hydrogen electrode) with a sweep rate of 100 mV s^{-1} to activate catalysts until the CV curve was stabilized (Figure 3.8). The ECSA was evaluated by measuring the charge collected in the hydrogen underpotential deposition (H_{upd}) region (0.05 V to 0.40 V *vs.* RHE) and normalized by the mass of Pt loaded on the electrode. The ECSA for CS-$Pt_{66}Cu_{34}$, CS-$Pt_{56}Cu_{28}Ni_{16}$, and CS-$Pt_{42}Cu_{20}Ni_{38}$ are ~ 37 m^2/g_{Pt}, ~ 50 m^2/g_{Pt}, and ~ 34 m^2/g_{Pt}, respectively.

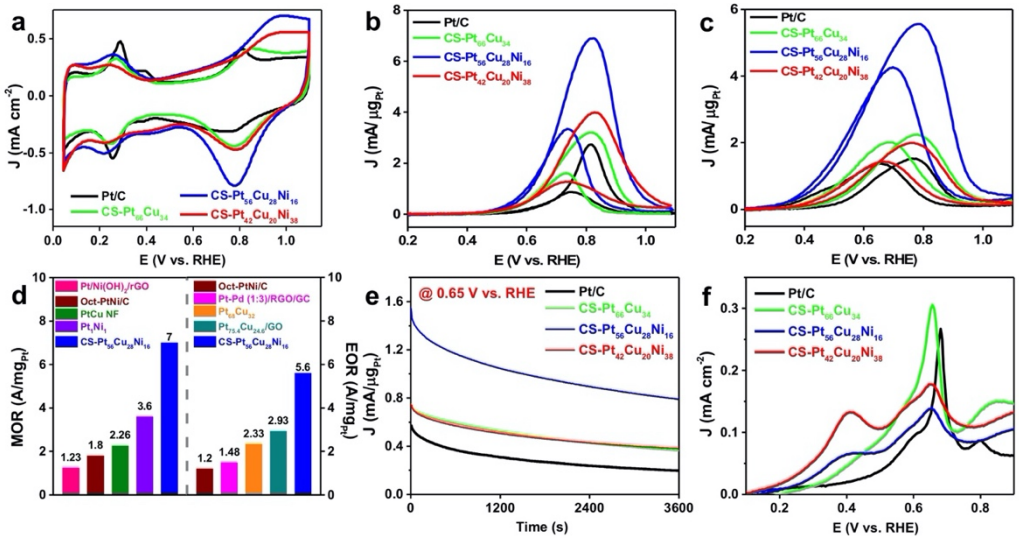

Figure 3.8. Electrocatalytic performance of the CS-$Pt_{66}Cu_{34}$, CS-$Pt_{56}Cu_{28}Ni_{16}$, and CS-$Pt_{42}Cu_{20}Ni_{38}$ catalysts for MOR and EOR compared against Pt/C in 1M KOH electrolyte. (**a**) Cyclic voltammetry (CV) performed between 0.05 V and 1.1 V *vs.* RHE at a scan rate of 100 mV/s. (**b**) The MOR CVs under a sweeping rate of 50 mV/s with 1 M methanol. (**c**) The EOR CVs under a sweeping rate of 50 mV/s with 1 M ethanol. (**d**) MOR/EOR performance comparison of the tetrahedral CS-$Pt_{56}Cu_{28}Ni_{16}$ with the state-of-art Pt-based catalysts: Pt/$Ni(OH)_2$/rGO[13], Oct-PtNi/C[14], PtCu NF[15], Pt_1Ni_1[10], Pt-Pd (1:3)/RGO/GC[9], $Pt_{68}Cu_{32}$ alloy[16], $Pt_{75.4}Cu_{24.6}$/GO[8]. More comprehensive comparison tables were given in the supporting information. (**e**) The chronoamperometry (CA) MOR test at a potential of 0.65 V *vs.* RHE. (**f**) CO stripping under a sweeping rate of 25 mV/s.

It is apparent that both CS-$Pt_{56}Cu_{28}Ni_{16}$, and CS-$Pt_{42}Cu_{20}Ni_{38}$ adsorbs OH_{ad} at a lower potential than CS-$Pt_{66}Cu_{34}$ and Pt/C (Figure 3.8a). This is due to the higher oxophilicity of superficial Ni than Pt and Cu. Most likely, surface Ni and NiO species have been transformed to $Ni(OH)_2$, especially at potential above 0 V *vs.* RHE[17], which has been reported in previous studies[18,19]. To explore their electrocatalytic activities, we evaluated their performance for MOR and EOR. The MOR test was conducted in 1 M KOH electrolyte with 1 M methanol. A CV with a scan rate of 50 mV/s was used to measure the MOR activity for all samples. MOR activities were determined when the CV cycles are stable (normally ~20 cycles). Notably, the SA of CS-$Pt_{56}Cu_{28}Ni_{16}$ reached 14.0 ± 1.0 mA/cm^2, which is higher than those of CS-$Pt_{66}Cu_{34}$ (8.6 ± 0.4 mA/cm^2), CS-$Pt_{42}Cu_{20}Ni_{38}$ (12.1 ± 0.3 mA/cm^2), and Pt/C (5.7 ± 0.2 mA/cm^2). Together with the higher ECSA, CS-$Pt_{56}Cu_{28}Ni_{16}$ shows a peak MA of 7.0 ± 0.5 A/mg_{Pt} at 0.81 V *vs.* RHE, which is much higher than those of CS-$Pt_{66}Cu_{34}$ (3.2 ± 0.2 A/mg_{Pt}), CS-$Pt_{42}Cu_{20}Ni_{38}$ (4.1 ± 0.1 A/mg_{Pt}), and Pt/C (2.6 ± 0.1 A/mg_{Pt}) (Figure 3.8b and Table 3.1).

Table 3.1. Catalytic performance comparison of the tetrahedra and Pt/C. Near-surface compositions were tested by the EDS line scans for the average composition within 1 nm from the surface. All catalytic performances were tested at least five times.

Materials	Near-surface composition	Specific activity (mA/cm^2)		Mass activity (A/mg_{Pt})		ECSA (m^2/g)
		MOR	EOR	MOR	EOR	
CS-$Pt_{66}Cu_{34}$	$Pt_{77}Cu_{23}$	8.6 ± 0.4	5.4 ± 0.3	3.2 ± 0.2	2.0 ± 0.1	37
CS-$Pt_{56}Cu_{28}Ni_{16}$	$Pt_{75}Cu_{14}Ni_{11}$	14.0 ± 1.0	11.2 ± 1.2	7.0 ± 0.5	5.6 ± 0.6	50
CS-$Pt_{42}Cu_{20}Ni_{38}$	$Pt_{41}Cu_{13}Ni_{46}$	12.1 ± 0.3	6.6 ± 0.2	4.1 ± 0.1	2.2 ± 0.1	34
Pt/C	Pure Pt	5.7 ± 0.2	2.9 ± 0.4	2.6 ± 0.1	1.3 ± 0.2	46

Similarly, the EOR performance tested in 1 M KOH with 1 M ethanol electrolyte shows a SA of 11.2 ± 1.2 mA/cm^2, which is significantly higher than those of CS-$Pt_{66}Cu_{34}$ (5.4 ± 0.3 mA/cm^2), CS-$Pt_{42}Cu_{20}Ni_{38}$ (6.6 ± 0.2 mA/cm^2), and Pt/C (2.9 ± 0.4 mA/cm^2). Thus, it can deliver a high MA of 5.6 ± 0.6 A/mg$_{Pt}$ at 0.77 V *vs.* RHE, which is higher than that of CS-$Pt_{66}Cu_{34}$ (2.0 ± 0.1 A/mg$_{Pt}$), CS-$Pt_{42}Cu_{20}Ni_{38}$ (2.2 ± 0.1 A/mg$_{Pt}$) and Pt/C (1.3 ± 0.2 A/mg$_{Pt}$) (Figure 3.8c).

We also performed chronoamperometry (CA) tests at 0.65 V *vs.* RHE to evaluate the stability of CS-$Pt_{66}Cu_{34}$, CS-$Pt_{56}Cu_{28}Ni_{16}$, CS-$Pt_{42}Cu_{20}Ni_{38}$, and Pt/C (Figure 3.8e). After 3,600-seconds stability test, the MA of CS-$Pt_{56}Cu_{28}Ni_{16}$ decayed from 1.56 A/mg$_{Pt}$ to 0.83 A/mg$_{Pt}$ (53% retention), which is comparable with CS-$Pt_{66}Cu_{34}$ (0.79 A/mg$_{Pt}$ to 0.40 A/mg$_{Pt}$, 51% retention), CS-$Pt_{42}Cu_{20}Ni_{38}$ (0.78 A/mg$_{Pt}$ to 0.41 A/mg$_{Pt}$, 52% retention), and much higher than Pt/C (0.20 A/mg$_{Pt}$, 29% retention). We also characterized morphologies and compositions for CS-$Pt_{56}Cu_{28}Ni_{16}$ after CA stability test (Figure 3.9). Although corners of nano tetrahedra became slightly rounded, tetrahedral shape and core-shell structure are retained. Together with the tailored surface, this catalyst with core-shell configuration can not only boost activity but also improve stability. EOR stability test was also performed and showed comparable performance to Pt/C (Figure 3.10).

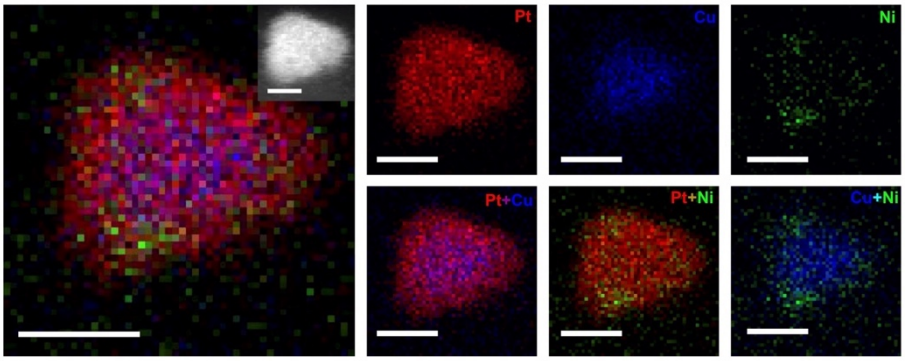

Figure 3.9. EDS mapping of tetrahedral nanoparticle CS-$Pt_{56}Cu_{28}Ni_{16}$ after MOR stability test. Inset is the corresponding HAADF STEM image. All scale bars are 2 nm.

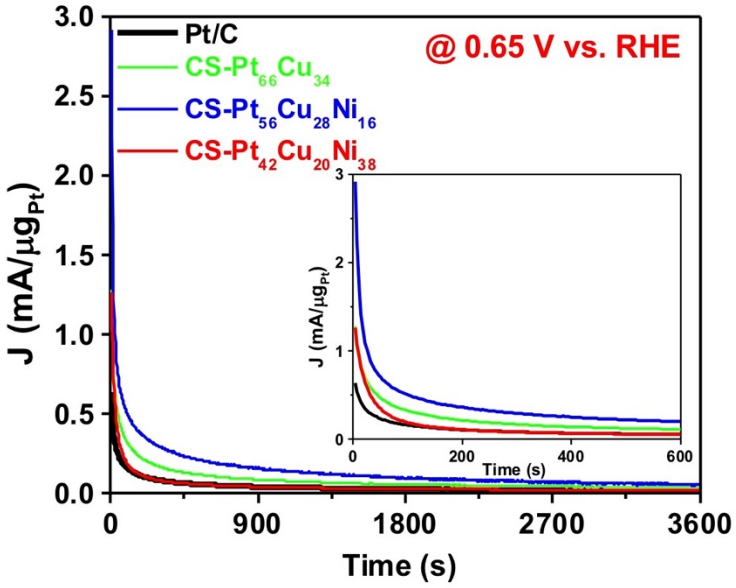

Figure 3.10. EDS mapping of tetrahedral nanoparticle CS-$Pt_{56}Cu_{28}Ni_{16}$ after MOR stability test. Inset is the corresponding HAADF STEM image. All scale bars are 2 nm.

It has been suggested that CO poisoning over Pt is one of the major reasons that cause the loss of MOR/EOR catalyst performance[20]. In order to investigate the role of Ni and Cu in assisting CO oxidation on MOR/EOR in the base, we further conducted CO stripping experiments to evaluate the ability of catalysts to oxidize CO_{ad}, which is a poisoning intermediate for MOR/EOR (Figures 3.8f, 3.11). Two oxidation peaks at different potentials are found in both CS-$Pt_{56}Cu_{28}Ni_{16}$ and CS-$Pt_{42}Cu_{20}Ni_{38}$. The first oxidation peak potential is about 0.4 V for CS-$Pt_{56}Cu_{28}Ni_{16}$ and CS-$Pt_{42}Cu_{20}Ni_{38}$, indicating easier CO oxidation than Pt/C (0.685V). This pre-oxidation is facilitated by OH_{ad} evidenced by CVs. Here, Pt and Ni together act as a bifunctional catalyst according to the Langmuir−Hinshelwood mechanism[6,21]. Pt adsorbs CO, while Ni helps adsorb OH_{ad}. If there is sufficient OH_{ad} present in the vicinity of CO, the CO oxidation step can be greatly accelerated. This phenomenon has also been observed in previous studies[10,13]. The second oxidation peak potential for CS-$Pt_{66}Cu_{34}$, CS-$Pt_{56}Cu_{28}Ni_{16}$, and CS-$Pt_{42}Cu_{20}Ni_{38}$ is ~ 0.650 V *vs.* RHE, which is ~35 mV lower than Pt/C (0.685 V). This is due to the alloying effect that mitigates

CO_{ad} adsorption, thus promoting CO_{ad} electro-oxidation[15,22,23]. A Pt surface with Cu has also been proved to facilitate water-gas shift reaction due to weaker CO bonding on PtCu[24]. These earlier CO oxidations demonstrated better MOR/EOR activity and stability than Pt/C. The core-shell tetrahedra configuration with Cu in the core can provide an effective structure as well as modifying the electronic structure for Pt, thus improving catalytic activity. Further, the presence of more oxophilic Ni on the surface can boost the activity based on core-shell PtCu tetrahedra alloys. However, it is noteworthy that excessive Ni will cover the active surface of Pt, rendering decreasing ECSA. Thus, the ratio of elements needs to be controlled to optimize the MA.

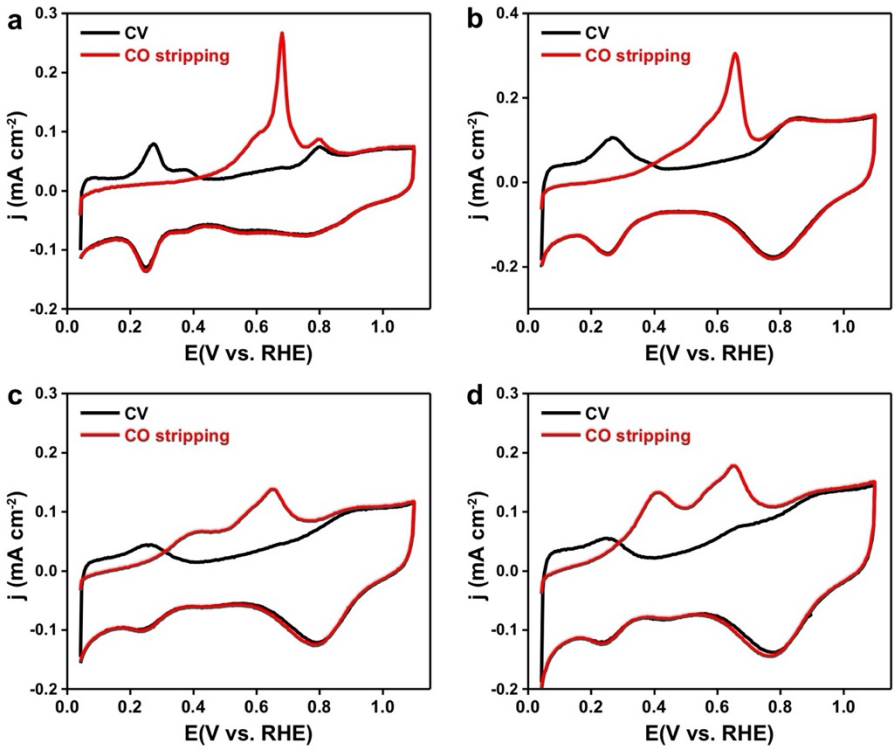

Figure 3.11. Comparison of CO stripping and CVs in 1 M KOH under sweeping rate of 25 mV/s for (**a**) Pt/C, (**b**) CS-$Pt_{66}Cu_{34}$, (**c**) CS-$Pt_{56}Cu_{28}Ni_{16}$ and (**d**) CS-$Pt_{42}Cu_{20}Ni_{38}$.

3.4 Conclusion

In summary, we developed a facile one-pot method to obtain nano tetrahedra with Cu-rich core and Pt/PtNi-rich shell. The XPS results and STEM EDS elemental mapping results confirmed

the core-shell configuration and elemental distributions. It is the first time that Pt-based tetrahedra structures with mainly transition metal in the core have been synthesized in a one-step synthesis. Our synthetic approach can not only achieve a unique Cu-rich core with Pt/PtNi-rich shell tetrahedral structure but also provides control over near-surface compositions. Electrocatalytic studies show that the CS-$Pt_{56}Cu_{28}Ni_{16}$ provides the best MOR and EOR MA of 7.0 ± 0.5 A/mg_{Pt} and 5.6 ± 0.6 A/mg_{Pt}, respectively, which is about 2-5 times and 2.5-5 times of that of the state-of-art catalysts[8-10,13,15,16]. The durability of MOR has also been strengthened, indicating the role of Pt-rich shell in preventing transition metal leaching. Overall, this unique Cu-rich core with Pt/PtNi-rich shell tetrahedra structure design provides a new pathway to improve MA and stability of Pt for diverse reactions and novel insight to rational design efficient Pt-based catalysts.

3.5 References

1. Subbaraman, R. *et al.* Enhancing Hydrogen Evolution Activity in Water Splitting by Tailoring Li+-Ni(OH)(2)-Pt Interfaces. *Science* **334**, 1256-1260 (2011).

2. Farias, M. J. S., Buso-Rogero, C., Gisbert, R., Herrero, E. & Feliu, J. M. Influence of the CO Adsorption Environment on Its Reactivity with (111) Terrace Sites in Stepped Pt Electrodes under Alkaline Media. *J. Phys. Chem. C* **118**, 1925-1934 (2014).

3. Stoffelsma, C. *et al.* Promotion of the Oxidation of Carbon Monoxide at Stepped Platinum Single-Crystal Electrodes in Alkaline Media by Lithium and Beryllium Cations. *J. Am. Chem. Soc.* **132**, 16127-16133 (2010).

4. Chung, D. Y., Lee, K. J. & Sung, Y. E. Methanol Electro-Oxidation on the Pt Surface: Revisiting the Cyclic Voltammetry Interpretation. *J. Phys. Chem. C* **120**, 9028-9035 (2016).

5. Lu, G. Q., Chrzanowski, W. & Wieckowski, A. Catalytic methanol decomposition pathways on a platinum electrode. *J. Phys. Chem. B* **104**, 5566-5572 (2000).

6. Subbaraman, R. *et al.* Trends in activity for the water electrolyser reactions on 3d M(Ni,Co,Fe,Mn) hydr(oxy)oxide catalysts. *Nat. Mater.* **11**, 550-557 (2012).

7. Strmcnik, D. *et al.* Improving the hydrogen oxidation reaction rate by promotion of hydroxyl adsorption. *Nat. Chem.* **5**, 300-306 (2013).

8. Liu, T. Y., Li, C. Z. & Yuan, Q. Facile Synthesis of PtCu Alloy/Graphene Oxide Hybrids as Improved Electrocatalysts for Alkaline Fuel Cells. *ACS Omega* **3**, 8724-8732 (2018).

9. Ren, F. F. *et al.* Clean Method for the Synthesis of Reduced Graphene Oxide-Supported PtPd Alloys with High Electrocatalytic Activity for Ethanol Oxidation in Alkaline Medium. *ACS Appl. Mater. Interfaces* **6**, 3607-3614 (2014).

10. Lu, S. Q., Li, H. M., Sun, J. Y. & Zhuang, Z. B. Promoting the methanol oxidation catalytic activity by introducing surface nickel on platinum nanoparticles. *Nano Res.* **11**, 2058-2068 (2018).

11. Chen, L. *et al.* Improved ethanol electrooxidation performance by shortening Pd-Ni active site distance in Pd-Ni-P nanocatalysts. *Nat. Commun.* **8**, 14136 (2017).

12. Jiang, K. Z. *et al.* Ordered PdCu-Based Nanoparticles as Bifunctional Oxygen-Reduction and Ethanol-Oxidation Electrocatalysts. *Angew. Chem., Int. Ed.* **55**, 9030-9035 (2016).

13. Huang, W. J. *et al.* Highly active and durable methanol oxidation electrocatalyst based on the synergy of platinum-nickel hydroxide-graphene. *Nat. Commun.* **6**, 10035 (2015).

14. Huang, X. Q. *et al.* A rational design of carbon-supported dispersive Pt-based octahedra as efficient oxygen reduction reaction catalysts. *Energy Environ. Sci.* **7**, 2957-2962 (2014).

15. Zhang, Z. C. *et al.* One-Pot Synthesis of Highly Anisotropic Five-Fold-Twinned PtCu Nanoframes Used as a Bifunctional Electrocatalyst for Oxygen Reduction and Methanol Oxidation. *Adv. Mater.* **28**, 8712-8717 (2016).

16. Liu, T. Y. *et al.* Monodispersed sub-5.0 nm PtCu nanoalloys as enhanced bifunctional electrocatalysts for oxygen reduction reaction and ethanol oxidation reaction. *Nanoscale* **9**, 2963-2968 (2017).

17. Liu, E. S. *et al.* Unifying the Hydrogen Evolution and Oxidation Reactions Kinetics in Base by Identifying the Catalytic Roles of Hydroxyl-Water-Cation Adducts. *J. Am. Chem. Soc.* **141**, 3232-3239 (2019).

18. Medway, S. L., Lucas, C. A., Kowal, A., Nichols, R. J. & Johnson, D. In situ studies of the oxidation of nickel electrodes in alkaline solution. *J. Electroanal. Chem.* **587**, 172-181 (2006).

19. Zhao, Z. P. *et al.* Surface-Engineered PtNi-O Nanostructure with Record-High Performance for Electrocatalytic Hydrogen Evolution Reaction. *J. Am. Chem. Soc.* **140**, 9046-9050 (2018).

20. Lee, M. J. *et al.* Understanding the Bifunctional Effect for Removal of CO Poisoning: Blend of a Platinum Nanocatalyst and Hydrous Ruthenium Oxide as a Model System. *ACS Catal.* **6**, 2398-2407 (2016).

21. Spendelow, J. S., Goodpaster, J. D., Kenis, P. J. A. & Wieckowski, A. Mechanism of CO oxidation on Pt(111) in alkaline media. *J. Phys. Chem. B* **110**, 9545-9555 (2006).

22. Tritsaris, G. A. & Rossmeisl, J. Methanol Oxidation on Model Elemental and Bimetallic Transition Metal Surfaces. *J. Phys. Chem. C* **116**, 11980-11986 (2012).

23. Zhao, Z. J., Mu, R. T., Wang, X. H. & Gong, J. L. Fast Prediction of CO Binding Energy via the Local Structure Effect on PtCu Alloy Surfaces. *Langmuir* **33**, 8700-8706 (2017).

24. Knudsen, J. *et al.* A Cu/Pt near-surface alloy for water-gas shift catalysis. *J. Am. Chem. Soc.* **129**, 6485-6490 (2007).

Chapter 4. 1D PtCo Nanowires as Stable Catalysts for PEMFCs with low Pt Loading

4.1 Introduction

Proton-exchange membrane fuel cells (PEMFCs) represent an attractive and sustainable power generation technology in automotive applications[1-3]. Although platinum (Pt) group metal (PGM) materials represent the most efficient catalysts facilitating the sluggish oxygen reduction reaction (ORR) in PEMFCs[2,4], the high cost of Pt and related components has severely impeded the broad dissemination of PEMFCs[5,6]. In principle, it is highly desirable to minimize the usage of Pt while achieving high performance. The Department of Energy (DOE) has set a beginning of life (BOL) mass activity (MA) target of 0.44 A/mg_{PGM} and a total loading target of 0.125 mg_{PGM}/cm^2 by 2020, and planned to further lower the loading to 0.1 mg_{PGM}/cm^2[6,7]. To this end, developing practical high-performance ORR catalysts for a membrane electrode assembly (MEA) with high MA and high power density is essential for minimizing Pt usage[3,8,9]. In general, Pt-alloy catalysts show much improved catalytic activity than pure Pt in rotating disk electrode (RDE) measurements owing to their adjusted Pt-O binding strength[10-13]. However, the higher activity does not necessarily translate directly to MEA. In addition, reducing the PGM loading while keeping the power density performance and stability adds more challenges due to the more severe mass transport issues and harsher testing conditions in MEA[3,6,14]. Large losses of power density were widely observed for cells with low Pt loadings (< 0.1 mg/cm^2) due to the decreasing Pt roughness factor (r.f., units of cm^2_{Pt}/cm^2_{MEA}) and the consequently increasing O_2 transport resistance[3,6,14]. In essence, to decrease loading while maintaining the same catalyst layer thickness, the interparticle distance became larger, leading to a faster Pt dissolution rate and worse structural stability[14]. This represents an intrinsic dilemma for currently low PGM loading MEAs: i.e. the decrease in usage of Pt usually comes with a substantial sacrifice in power density and stability that leads to low Pt

utilization. Therefore, it is of primary importance to design catalysts to overcome the above said dilemma.

One-dimensional (1D) nanostructures can simultaneously achieve high ECSA and MA, offering considerable potential for lowering the Pt loading in PEMFCs[15,16]. In addition, 1D nanostructures showed better structural stability than nanoparticles, which can effectively mitigate aggregation and dissolution[17] and can potentially help retain high power density at low PGM loading in MEA. Previously, the Jagged-Pt nanowires developed by Li et al. showed a record-high MA of 13.6 A/mg_{Pt} towards ORR on the rotating disk electrode (RDE)[13]. During the electrochemical dealloying process, nanowires could maintain the 1D structure, proving its high structural stability. Bu et al. and Jiang et al. also prepared a series of Pt-alloy NWs, showing respectable activity and stability[18,19]. Despite promising performance reported for 1D catalysts in half-cell RDE measurements, the outstanding performance of this new generation of catalysts has not yet been incorporated and investigated in a MEA[2,3,20,21]. Furthermore, low PGM loading MEA (e.g. $\leq$ 0.1 mg_{PGM}/cm^2 planned by 2025)[6] has been rarely reported. Therefore, it is highly desirable to incorporate Pt-based nanowires into MEAs to fully demonstrate and capture their merit in practical PEMFCs with low Pt loading, owing to their demonstrated high MA and ECSA.

Herein, we demonstrated an ultralow Pt loading (total loading of 0.072 mg_{Pt}/cm^2) and high-performance MEA using ultrathin platinum-cobalt nanowires (PtCoNWs) as cathode catalysts. The PtCoNWs showed a high ECSA of 73.2 m^2/g_{Pt} and achieved a unprecedented MA of 1.06 ± 0.14 A/mg_{Pt} [0.9 $V_{iR\text{-}free}$] at the BOL stage in MEA. This MA is 3.3 times that of the commercial Pt/C (0.32 A/mg_{Pt}) and far surpasses the DOE 2020 target (0.44 A/mg_{PGM}). The PtCoNWs reached a peak power density of 1016 mW/cm^2, outperforming the PtNWs (830 mW/cm^2) and Pt/C (773 mW/cm^2) with comparable Pt loading. After the AST, the

PtCoNWs showed a respectable end of life (EOL) MA of 0.45 A/mg_{Pt}, remaining above the DOE 2020 BOL target.

4.2 Experimental methods

Materials and chemicals

All chemicals were purchased from Sigma-Aldrich unless otherwise specified. Commercial Pt/C catalyst (10 wt% and 40 wt% Pt) were purchased from Alfa Aesar. Isopropanol (≥ 99.5%) were purchased from Fisher Scientific. All reagents were used as received without further purification. For MEA test, Ketjen-300J carbon was obtained from Lion Specialty Chemicals Co., Ltd. The deionized water (18 MΩ/cm) was obtained from an ultra-pure purification system (Milli-Q advantage A10). The Nafion HP membranes were purchased from fuel cell store.

Synthesis of PtCoNWs and PtNWs catalysts

In typical synthesis of PtCoNWs, 200 mg $Pt(acac)_2$ and 100 mg $Co(acac)_2$ were mixed with 675 mg glucose, 16mg $W(CO)_6$ and 150 mg PVP-10,000 in a glass vial, with 50 ml of oleylamine and octadecene (3:2 volume ratio) as co-solvent. The mixture was heated to 180 °C for 6 h to form as-prepared PtCo alloy nanowires. The resulting nanowires were collected via centrifuge at 3,000 r.p.m. for 10 min. After loading the nanowires on carbon (Kejten black), the catalysts were then annealed under 450 °C in argon/hydrogen (97:3) atmosphere for 6 h. After annealing, the resulting product was dealloyed in 0.5 M sulfuric acid at 80 °C for 4 hours and washed till the pH is neutral, then annealed in Ar/H_2 (3% H_2) atmosphere at 200 °C for 2 hours to obtain the final ultrafine PtCoNWs.

Synthesis of PtNWs catalysts

For comparison, PtNWs were also prepared via a similar synthesis and processing method. 200 mg $Pt(acac)_2$ and 100 mg $Co(acac)_2$ were mixed with 675 mg glucose, 16mg $W(CO)_6$ and 150 mg PVP-10,000 in a 250 ml glass vial, with 50 ml of oleylamine and octadecene (3:2 volume ratio) as co-solvent. The mixture was heated to 120 °C for 6 h to form Pt nanowires. The resulting nanowires were collected via centrifuge at 3,000 r.p.m. for 10 min. After loading the nanowires on carbon (Kejten black), the catalysts were then annealed under 400 °C in argon/hydrogen (97:3) atmosphere for 6 h. After annealing, the resulting product was dealloyed in 0.5 M sulfuric acid at 80 °C for 4 hours and washed till the pH is neutral, then annealed in Ar/H_2 (3% H_2) atmosphere at 200 °C for 2 hours to obtain the final ultrafine PtNWs.

Structure and composition characterization

Low magnification transmission electron microscopy (TEM) images were taken on a FEI T12 transmission electron microscope operated at 120 kV. High-resolution TEM images (HRTEM), energy-dispersive X-ray spectroscopy (EDX) line-scan file and the high-angle annular dark-field scanning transmission electron microscope (HAADF-STEM) images were taken on JEM-ARM300F Grand ARM transmission electron microscope operated at 300 kV. TEM samples were prepared by dropping ethanol dispersion of catalysts onto carbon-coated aluminum TEM grids. The elementary concentration of catalysts was determined by the inductively coupled plasma (ICP) atomic emission spectroscopy. The Pt loading the catalysts is determined by the catalyst before electrochemical ink preparation. The MEA loading is determined by ICP before and after the MA and power density measurement. In specific, 2 pieces of sprayed catalysts (2 cm^2) were cut and soaked in the aqua regia for one day and were used to prepare ICP solution for metal content measurement. The loading after the MEA measurements was also checked for the accuracy of our results.

MEA preparation and single fuel cell test

The single fuel cell performance of the catalysts as the cathode was tested at an 850e Fuel Cell Test System (Scribner, USA). The MEAs with an active area of 5.0 cm^2 were fabricated using the catalyst-spray membrane method. Catalysts were incorporated into MEAs by direct ultrasonic spraying of a water/2-propanol based ink onto a Nafion HP membrane with desired loading. The anode loading was set to be 0.025 mg_{Pt}/cm^2. The mass activity was measured via measuring the current at 0.9 V (iR-free) in 150 kPa absolute pressure (abs) H_2/O_2 (80 °C, 100% RH, 835/2,000 sccm) with correction for measured H_2 crossover. The H_2-Air tests were measured under 150 kPa_{abs} H_2/Air (80 °C, 100% RH, 835/2,000 sccm). The AST was conducted using the square wave method from 0.6 V to 0.95 V with 3 s hold time at each potential (150 kPa_{abs}, 80 °C, 100% RH, H_2/N_2 = 100/100 sccm). Rated power voltage = (77.6 / (22.1 + T(°C))) V, based on target of $Q/\Delta Ti$ = 1.45 kW/°C. [rated voltage = 0.76 V for 80 °C]. The Pt utilization was calculated by normalizing the rated power by total Pt loading.

XAS data collection and analysis

The electrode inks for the XAS electrodes were composed of ethanol, 5 wt % Nafion solution, and the catalyst powder. The ink was drop cast onto a carbon paper with a total catalyst loading about 8 mg/cm^2. The ADT samples for XAS were cycled on the carbon paper for 20,000 cycles at room temperature in O_2-saturated 0.1 M $HClO_4$ solutions by applying CV sweep between 0.6 and 1.1 V versus RHE at a sweep rate of 100 mV/s. The XAS experiments were conducted at room temperature in a previously described *in-situ* spectro-electrochemical half-cell in which a continuously O_2 purged 0.1 M $HClO_4$ aqueous solution was circulated[22], at the beamline ISS 6-BM and 8-ID in National Synchrotron Light Source II (NSLS-II) (Brookhaven National Laboratory, NY). Before transferred into the cell, the electrodes were conditioned in 0.1 M $HClO_4$

under vacuum for 40 minutes to remove surface oxides and contaminants. Potentiostatic control was maintained with an Autolab PGSTAT30 potentiostat (Metrohm USA, formerly Brinkman Instruments). Full range Pt L_3-edge and Co K-edge spectra were taken at various static potentials along the anodic sweep of the CV. Data were collected on the same electrode in transmission mode at the Pt L_3-edge, and fluorescence mode at the Co K-edge, with a Pt/Co reference foil positioned between the ionization chambers I2 and I3 as a reference. The voltage cycling limits were 0.05 to 1.00 V vs. RHE. Data collection was performed at the chosen potentials held during anodic sweeps. The electrode was fully cycled following each potential hold to clean the electrode surfaces after each potential hold. Typical experimental procedures were utilized with details provided in our previous work[23]. The data were processed and fitted using the Ifeffit–based Athena[24] and Artemis[25] programs. Scans were calibrated, aligned, and normalized with background removed using the IFEFFIT suite[26]. The χ(R) were modeled using single scattering paths calculated by FEFF6[27].

4.3 Results and discussion

Structural and compositional characterizations

To prepare ultrathin PtCoNWs, PtCo alloy NWs were first prepared by reducing platinum(II) acetylacetonate [$Pt(acac)_2$] and cobalt(II) acetylacetonate [$Co(acac)_2$] in the mixed solvent of 1-octadecene and oleylamine according to revised synthesis reported previously[13]. The as-prepared PtCoNWs were then loaded onto carbon black (Ketjen black, denoted as KB), followed by annealing and acid dealloying processes to produce the final ultrathin PtCoNWs (see Supporting Information for details) (Figure 4.1). Transmission electron microscopy (TEM) and high-angle annular dark-field scanning transmission electron microscopy (HAADF-STEM) showed that the as-prepared PtCoNWs have a well-

defined 1D structure (Figures 4.1b, 4.2) with a typical length of 200-300 nm and an average diameter of 1.8 ± 0.3 nm (Figures 4.2b). The average lattice spacing of 0.191 nm (Figure 4.1d) derived from the fast Fourier transform (FFT) was attributed to the interplane distance of (200) plane of PtCo alloy. After annealing and dealloying, the resulting PtCoNWs maintained the ultrathin 1D structure (Figures 4.1c, 4.3a) with an average diameter of 2.3 ± 0.7 nm (Figure 4.3b). The enlarged diameter may be attributed to ripening during the treatment process. The average lattice spacings of 0.225 nm and 0.191 nm along the [011] zone axis were ascribed to (111) and (200) facets, respectively (Figure 4.1e). Energy dispersive X-ray (EDX) line scan profiles and mapping results revealed that before annealing and dealloying, the as-prepared PtCoNWs had a uniform Pt and Co elemental distribution throughout the nanowires (Figures 4.1f, 4.2b) with a composition of ca $Pt_{67}Co_{33}$ (Figure 4.2d and Table 4.1). The composition of the final PtCoNWs became ca $Pt_{82}Co_{18}$ upon dealloying, indicating the loss of Co during the process (Table 4.1), which is consistent with the inductively coupled plasma atomic emission spectroscopy (ICP-AES) results. The Pt loading of the PtCoNWs on carbon is determined to be 11.0% by ICP. Moreover, the dealloying process changed the composition distribution from uniformly distributed PtCo alloy NWs to compositional-segregated NWs with PtCo alloy core and Pt-rich skin. As shown in the EDX line scan profiles, the final PtCoNWs have a PtCo core and an ultrathin Pt-rich shell of 0.6 nm (Figure 4.1g). The inverse FFT analysis suggested that the (111) lattice spacings are different at the core (0.216 nm) and the shell (0.227 nm) regions (Figure 4.3e and f), indicating higher Pt content in the shell ($Pt_{99}Co_1$) than in the core ($Pt_{52}Co_{48}$) according to the Vegard's law, consistent with the EDX line scan profiles (Figure 4.1g). We also prepared Pt nanowires (PtNWs) as reference sample following previously reported approach[13], which were subjected to the same treatment process

performed on PtCoNWs. Similarly, PtNWs maintained the morphology after the annealing and acid washing with an average diameter of 1.8 ± 0.5 nm (Figure 4.4).

The structural details of PtCoNWs were studied using *in-situ* XAS. The white line intensity of the x-ray absorption near-edge structure (XANES) spectrum of PtCoNWs (Figure 4.5a) at the Pt L_3-edge decreased (red arrow) compared with that of Pt/C reference, indicating decreasing Pt d-band vacancies due to the formation of the PtCo alloy.[28] The extended x-ray absorption fine structure (EXAFS) fitting result showed the first-shell Pt-Pt bond length of PtCoNWs is 2.72 Å (Figure 4.5c and Table 4.2), which is about 1.1% shorter than that in of Pt/C (2.75 Å). Furthermore, the degree of alloying of the bimetallic PtCoNWs structures were indicated by analyzing the extent of alloying (J factor) that was derived from the first-shell coordination numbers (CNs).[29] In PtCoNWs, the J_{Pt} and J_{Co} values were determined to be 1.3 and 1.0, respectively (Table 4.2), which are higher than those expected for disordered alloyed structure (J = 1), indicating a well-mixed distribution of Pt and Co atoms.[30] These results showed that PtCoNWs possessed a high degree of alloying, which may promote ligand effect and mitigate Pt dissolution.[31,32]

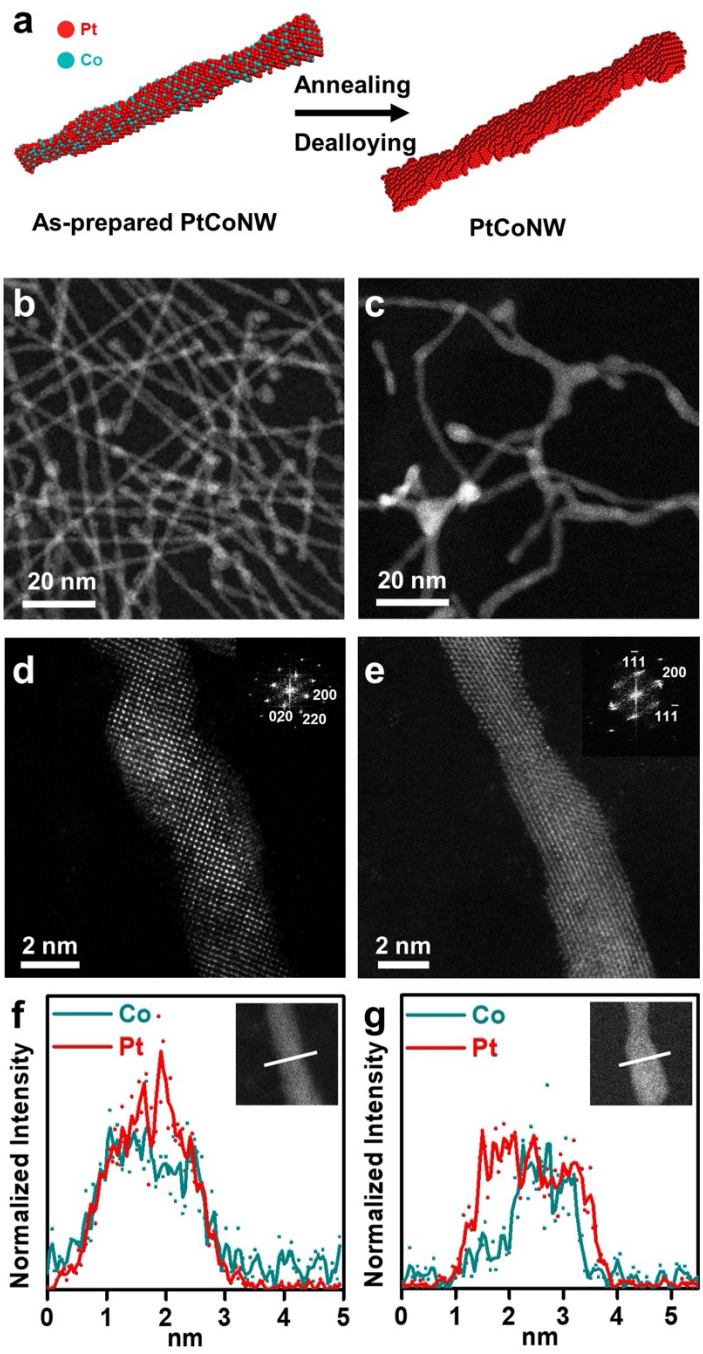

Figure 4.1. Structural and compositional characterizations of as-prepared PtCoNWs and ultrathin PtCoNWs after annealing and dealloying. (**a**) Schematic illustration of transformation from as-prepared alloy PtCoNWs to ultrathin PtCoNWs with a Pt-rich shell and PtCo-alloy core. (**b** and **c**) Representative HAADF-STEM images of as-prepared PtCoNWs and ultrathin PtCoNWs. (**d** and **e**) Atomic resolution STEM images of as-prepared PtCoNWs and ultrathin PtCoNWs, inset is the fast Fourier-transform pattern. (**f** and **g**) EDX spectroscopy line-scan profiles of as-prepared PtCoNWs and ultrathin PtCoNWs.

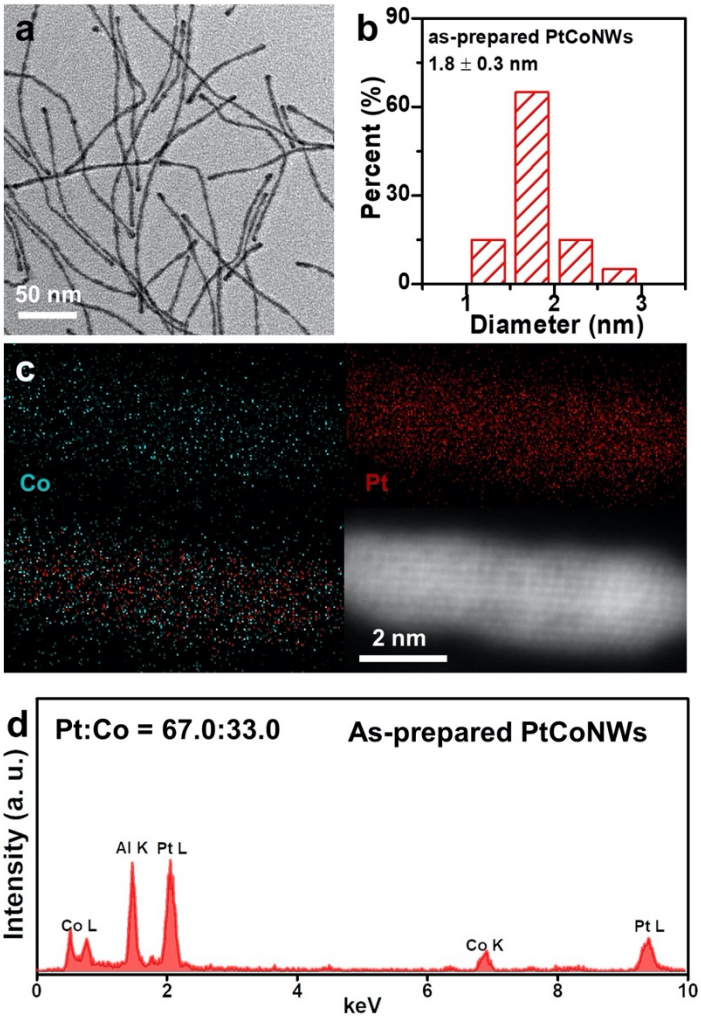

Figure 4.2. (**a**) TEM image of as-prepared PtCoNWs. (**b**) Size distribution of the as-prepared PtCoNWs. (**c**) EDX elemental mapping results of as-prepared PtCoNW. (**d**) Representative EDX spectrum of the as-prepared PtCoNWs.

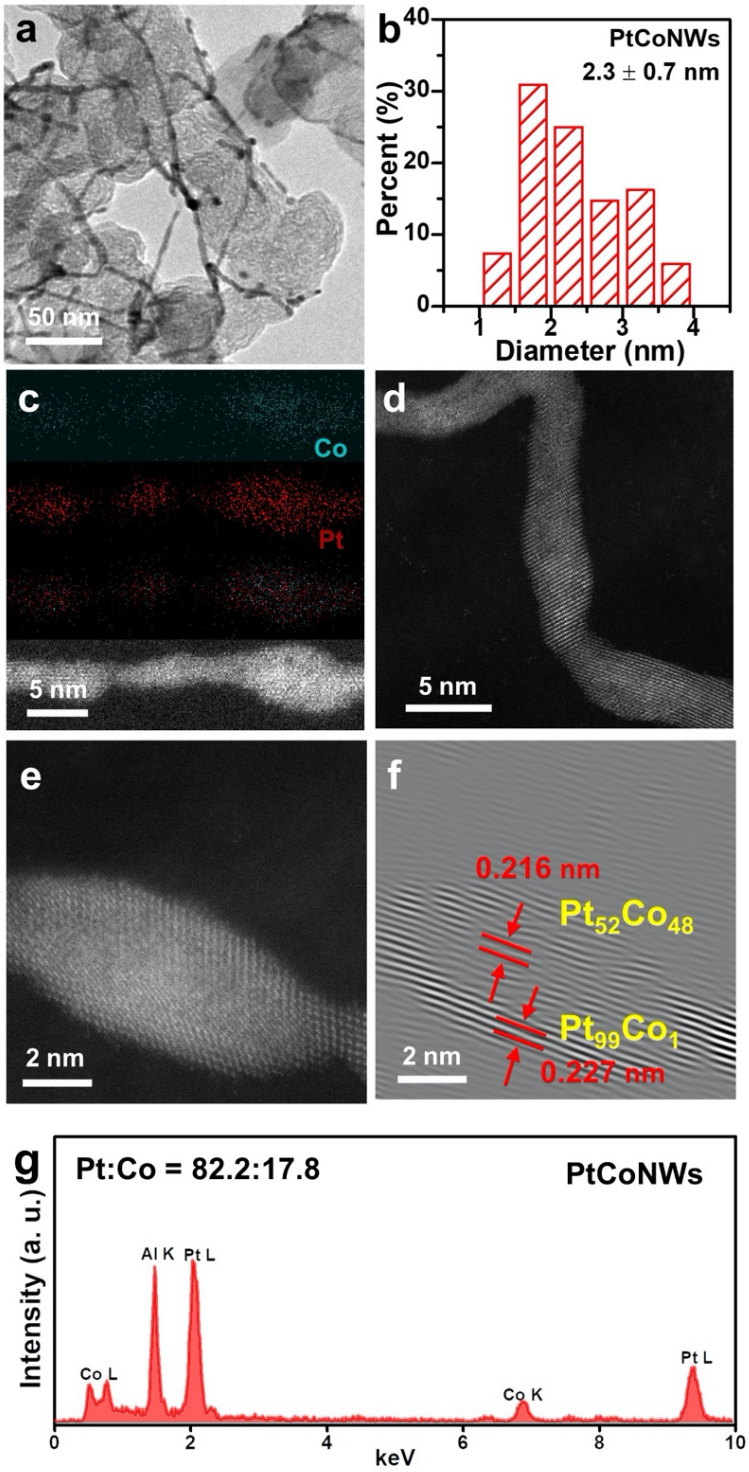

Figure 4.3. (**a**) TEM image of ultrathin PtCoNWs. (**b**) Size distribution of ultrathin PtCoNWs. (**c**) EDX elemental mapping of ultrathin PtCoNWs. (**d** and **e**) High resolution STEM images. (**f**) Inverse FFT of the STEM in panel (**e**). (**g**) Representative EDX spectrum of the ultrathin PtCoNWs.

Table 4.1 Composition of PtCoNWs at different stages.

Sample	EDX composition	
	Pt at.%	Co at.%
As-prepared PtCoNW	67.0 ± 4.7	33.0 ± 4.7
PtCoNW	82.2 ± 2.9	17.8 ± 2.9
PtCoNW before AST	86.5 ± 2.6	13.5 ± 2.6
PtCoNW after AST	91.0 ± 1.8	9.0 ± 1.8

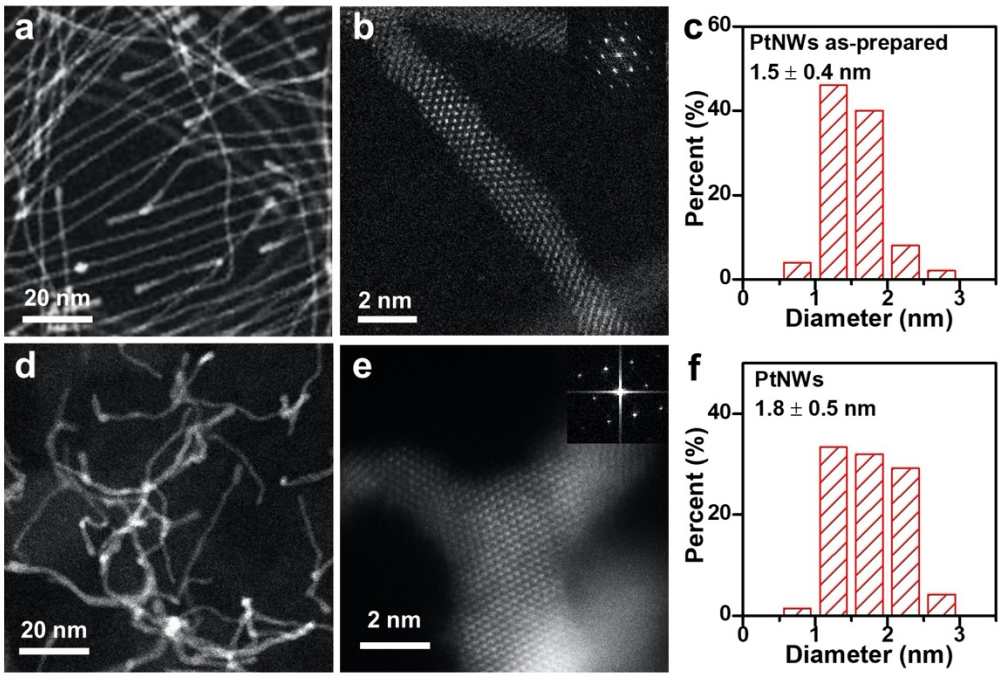

Figure 4.4. (**a, b** and **c**) STEM images and size distribution of the as-prepared PtNWs. (**d, e** and **f**) STEM images and size distribution of the PtNWs after annealing and acid wash.

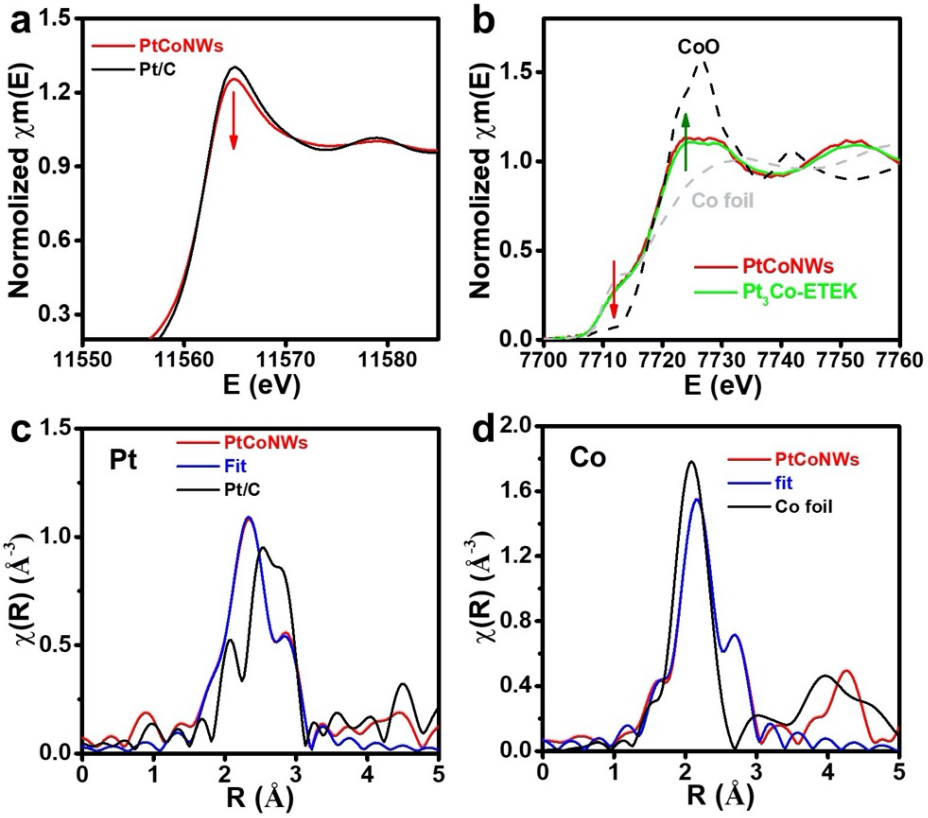

Figure 4.5. XAS results of the PtCoNWs in comparison with Pt/C. (**a** and **b**) XANES spectra at the (**a**) Pt L_3-edge and (**b**) Co K-edge with Pt/C and Pt_3Co-ETEK as references. (**c** and **d**) Fourier-transform EXAFS spectra and the corresponding first shell least-square fit (blue) at the (**c**) Pt L_3-edge and (**d**) Co-K edge for the PtCoNWs.

Table 4.2 EXAFS fitting results of the PtCoNWs.

	Pt-Pt scattering			Pt-Co scattering		
J_{Pt}	R_{Pt-Pt} (Å)	N_{Pt-Pt}	σ^2 (Å^2)×10^{-3}	R_{Pt-Co}(Å)	N_{Pt-Co}	σ^2 (Å^2)×10^{-3}
1.3	2.724 ± 0.005	6.9 ± 0.8	5.0 ± 0.9	2.65 ± 0.01	2.1 ± 0.7	10 ± 3
	Co-Co scattering			Co-Pt scattering		
J_{Co}	R_{Co-Co} (Å)	N_{Co-Co}	σ^2 (Å^2)×10^{-3}	R_{Co-Pt}(Å)	N_{Co-Pt}	σ^2 (Å^2)×10^{-3}
1.0	2.60 ± 0.01	1.8 ± 0.7	3 ± 3	2.65 ± 0.01	10 ± 1	10 ± 3

*Fits were done at the Pt L_3-edge and Co K-edge in *R*-space simultaneously, $k^{1,2,3}$ weighting. 1.17 < *R* < 3.22 Å and Δk = 2.73 – 11.00 Å^{-1} were used for fitting of the Pt edge data and 1.17 < *R* < 3.05Å and Δk = 2.6 – 10.6 Å^{-1} were used for fitting of the Co edge data. S_0^2 was fixed at 0.83 and 0.80 for Pt and Co, respectively, obtained by fitting the Pt and Co reference foils.

MEA performance

We further applied the resulting ultrathin PtCoNWs, PtNWs, and commercial Pt/C (40 wt% Pt, Alfa Aesar) on the cathode of MEAs and compared their performance in a PEMFC single cell with oxygen or air as the cathodic feeding gas. The MEAs were prepared by ultrasonic spraying the catalysts directly on two sides of the proton-exchange membrane. The geometric Pt loading in MEAs was fixed at 0.025 mg_{Pt}/cm^2 for anode and about 0.05 mg_{Pt}/cm^2 for cathode. The MAs of PtCoNWs, PtNWs, and commercial 40% Pt/C catalysts in MEA were evaluated in the H_2-O_2 atmosphere at 80 ^oC, using the hydrogen-crossover corrected current densities at 0.9 $V_{Cell,\ iR\text{-}free}$. In both H_2-O_2 and H_2-Air tests, the PtCoNWs delivered a much higher current density than PtNWs and Pt/C in all potential regions (Figure 4.6a and b). The PtCoNWs demonstrated an exceptional high MA of 1.06 ± 0.14 A/mg_{Pt} at 0.9 V at BOL, which is 2.4 times that of the pure PtNWs (0.44 A/mg_{Pt}) and 3.3 times that of the commercial 40% Pt/C catalysts (0.32 A/mg_{Pt}) (Figure 4.6c), far exceeding the 2020 DOE target (0.44 A/mg_{PGM}). Impressively, the PtCoNWs exhibited the record-high MA among the state-of-the-art Pt-alloy catalysts in MEAs (Table 4.3).

Importantly, when incorporated in MEA (ca. 0.025 mg_{Pt}/cm^2 for anode and ca. 0.05 mg_{Pt}/cm^2 for cathode), the PtCoNWs delivered a large ECSA of 73.2 m^2/g_{Pt}, which was much higher than that of PtNWs (47.0 m^2/g_{Pt}) and Pt/C (33.0 m^2/g_{Pt}) (Figure 4.7). The PtNWs only demonstrated a modest ECSA despite having a smaller average diameter, suggesting that PtNWs might suffer more coalescence or dissolution during the activation process. Indeed, after the MA measurement, PtCoNWs maintained the 1D morphology with a size distribution of 3.1 ± 0.9 nm (Figure 4.8a). Under the same conditions, however, PtNWs evolved into nanorods and nanoparticles (NPs) with a size distribution of 3.6 ± 1.1 nm and

3.91 ± 0.6 nm, respectively (Figure 4.9). Therefore, the large ECSA of PtCoNWs may be attributed to their 1D structure with a high surface area that was well maintained after the MA measurement. In addition, the inverse FFT analysis of the PtCoNWs after the MEA test further confirmed that the segregated structure of the Pt-rich shell ($Pt_{98}Co_2$) and the alloy core ($Pt_{59}Co_{41}$) was also retained, showing different (111) lattice spacings at the core (0.218 nm) and the shell (0.227 nm) regions (Figure 4.8e and f). Impressively, the composition changed only slightly from $Pt_{82}Co_{18}$ to $Pt_{86}Co_{14}$ after the MA measurement (Figure 4.8g). All suggest excellent intrinsic structural and compositional stability of the PtCoNWs in MEA.

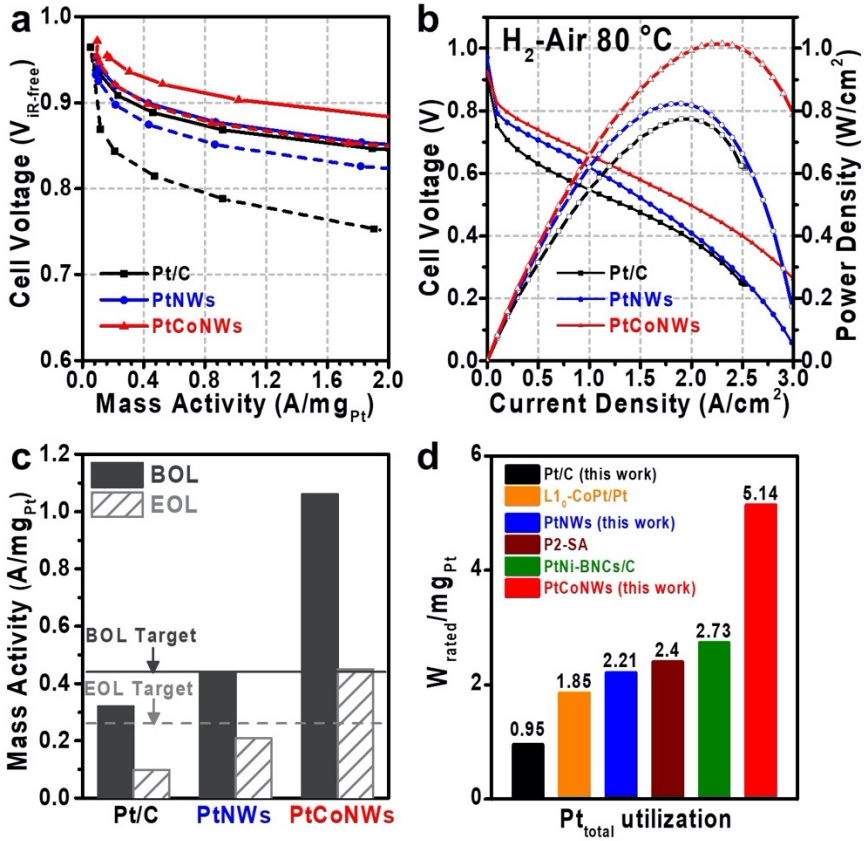

Figure 4.6. Comparison of MEA performances of PtCoNWs, PtNWs, Pt/C, and state-of-the-art catalysts. (**a**) The BOL (solid line) and EOL (dashed line) MA polarization curves of Pt/C, PtNWs and PtCoNWs tested in H_2-O_2 atmosphere. (**b**) H_2-air I-V polarization (solid marks) and power density (hollow marks) curves of Pt/C, PtNWs, and PtCoNWs. (**c**) Comparison of MAs at 0.9 $V_{iR\text{-}}$

$_{free}$ for Pt/C, PtNWs and PtCoNWs. DOE 2020 MA target: 0.44 A/mg$_{PGM}$ (BOL) and 60% retention (0.264 A/mg$_{PGM}$) (EOL). (**d**) Comparison of total Pt utilization of PtCoNWs with the state-of-the-art values reported previously. The total Pt utilization was calculated by normalizing the rated power density over total Pt loading. Reference: $L1_0$-CoPt/Pt: 9 nm $L1_0$-phase intermetallic PtCo nanoparticles.[11] P2-SA: 5 nm PtNi nanoparticles dealloyed 0.5 M sulfuric acid at 80 °C for 24 h in nitrogen.[33] PtNi-BNCs/C: Pt-Ni bunched nanocages.[10]

Table 4.3. Comparisons of the MEA performance among the state-of-the-art catalysts.

Catalyst	Total loading (Anode + Cathode) (mg_{PGM}/cm^2)	MA (A/mg)		AST condition	Power density at 0.6 V (mW/cm^2)	Peak power density (mW/cm^2)	H_2-air test condition
		BOL	EOL				
PtCoNWs (This work)	**0.072 (0.025 + 0.047)**	**1.06**	**0.45**	Square wave: 0.6 V-0.95 V 30,000 cycles	**840**	**1016**	Nafion HP, 80 °C, 150 kPa, 100% RH
PtNWs (This work)	**0.077 (0.025 + 0.052)**	**0.44**	**0.21**		**660**	**830**	
Pt/C (This work)	**0.075 (0.025 + 0.050)**	**0.32**	**0.098**		**402**	**773**	
PtNi-BNSs/C[10]	0.25 (0.1 + 0.15)	NA	NA	Air-conditioned at room temperature of 26 °C for 180 hours	600	770	Nafion 212, 80 °C, 300 kPa, 100% RH
PtNi-BNCs/C[10]	0.25 (0.1 + 0.15)	NA	NA		900	920	
$L1_0$-CoPt/Pt[11]	0.205 (0.1 + 0.105)	0.56	0.45	Trapezoidal wave: 0.6 V-0.95 V 30,000 cycles	570	NA	Nafion 211, 80 °C, 150 kPa, 100% RH
PtNi NW array[34]	0.312*	0.07	0.051	0.6-1.2 V (100 mV/s) 3,000 cycles	541	NA	Nafion 212, 80 °C, cathode/anode: 230/250 kPa, 30%/50% RH
Pt NW array[34]	0.312*	0.062	0.064		504	NA	
P2-SA[33]	0.15 (0.05 + 0.1)	0.64	0.5	Triangle wave: 0.6-1.0 V (50 mV/s) 30,000 cycles	900	NA	Nafion 211, 80 °C, 170 kPa, 100% RH
P2-NA[33]	0.15 (0.05 + 0.1)	0.62	0.43		900	NA	

*: assuming this is the total loading of Pt due to missing specification. NA: not available. Reference: PtNi-BNSs/C: Pt-Ni bunched nanospheres.[10] PtNi-BNCs/C: Pt-Ni bunched nanocages.[10] $L1_0$-CoPt/Pt: 9 nm $L1_0$-phase intermetallic PtCo nanoparticles.[11] PtNi NW array: PtNi nanowire array gas diffusion electrode.[34] Pt NW array: Pt nanowire array gas diffusion electrode.[34] P2-SA: 5 nm PtNi nanoparticles dealloyed 0.5 M sulfuric acid at 80 °C for 24 h in nitrogen.[33] P2-NA: 5 nm PtNi nanoparticles dealloyed 1 M nitric acid at 70 °C for 24 h in nitrogen.[33]

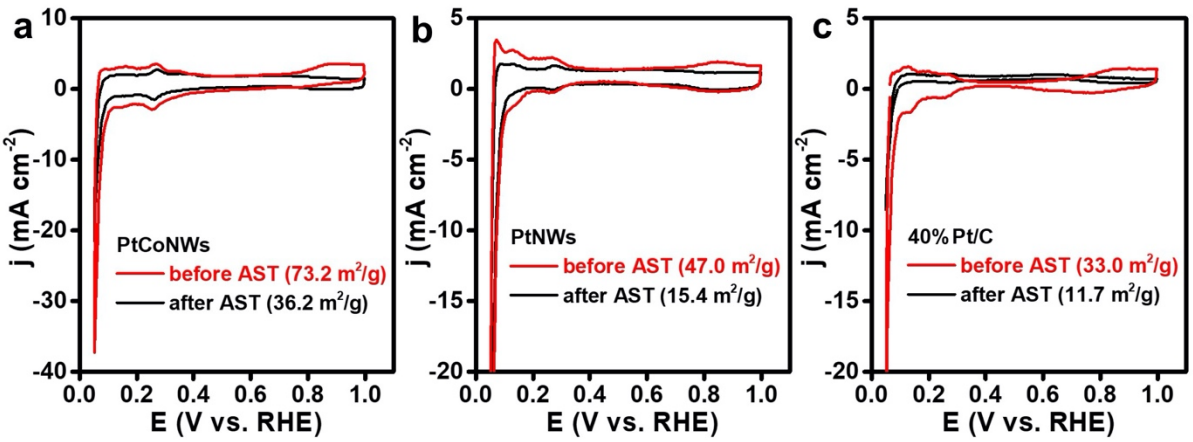

Figure 4.7. ECSAs of the PtCoNWs in comparison with Pt/C and PtNWs before and after AST. All ECSAs were measured on MEA.

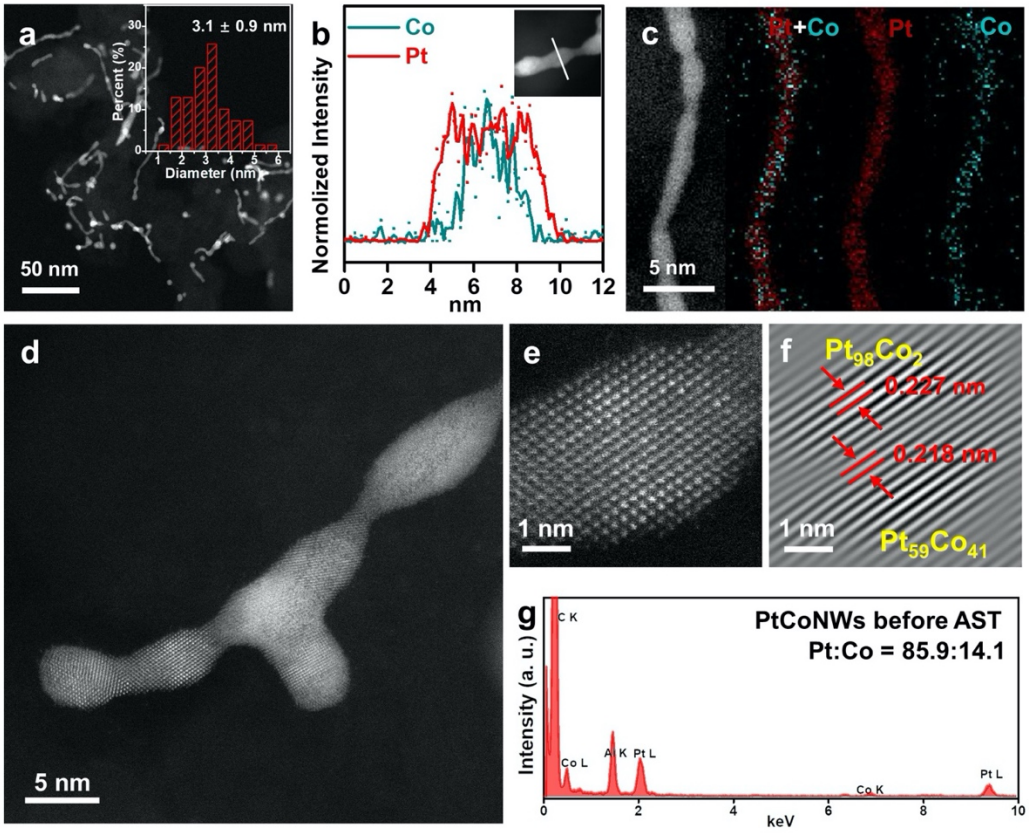

Figure 4.8. Characterizations of the PtCoNWs after activation process and MA measurement, which represents the state before AST. (**a**) STEM low magnification image, inset is the size distribution analysis. (**b**) EDX line-scan profiles. (**c**) EDX mapping results. (**d** and **e**) High resolution STEM images. (**f**) Inverse FFT of the STEM in panel (**e**). (**g**) Representative EDX spectrum result.

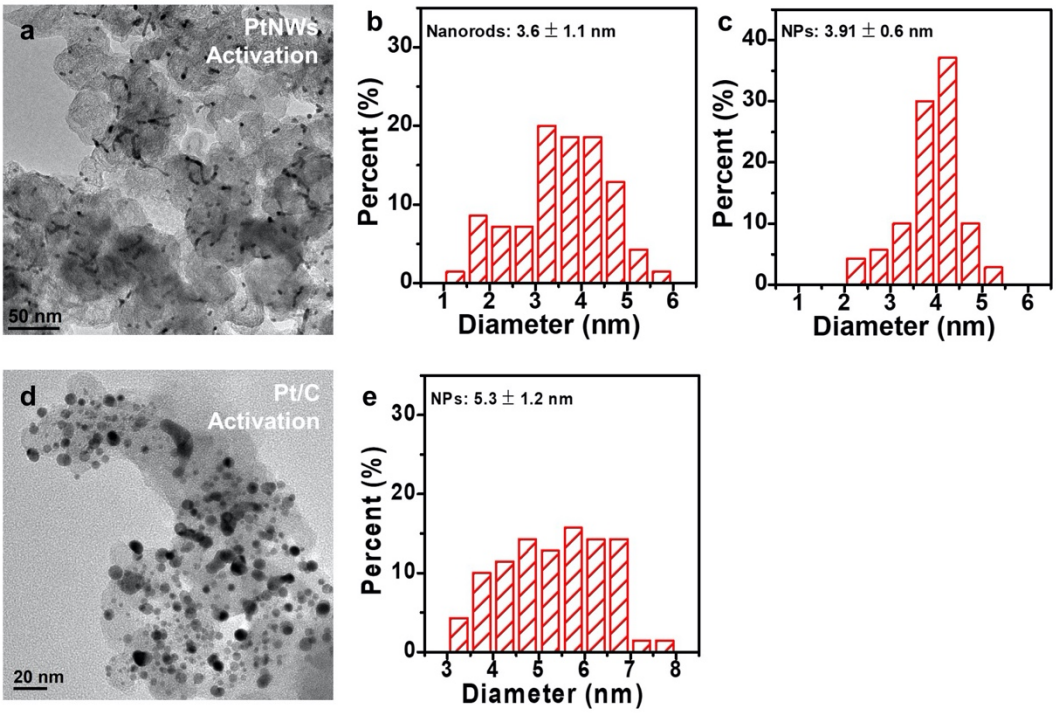

Figure 4.9. (**a** to **c**) TEM image and size distribution of nanorods and nanoparticles (NPs) from PtNWs after activation process and MA measurement. (**d** to **e**) TEM image and size distribution of Pt/C after activation process and MA measurement, suggesting the growth of Pt NPs after activation and MA measurement.

The outstanding MA and large ECSA enabled the PtCoNWs to exhibit high power density in H_2-air tests (Figure 4.6b). The PtCoNWs and PtNWs showed higher current density than that of Pt/C at all potential regions. The PtCoNWs delivered a current density of 1.4 A/cm^2 at 0.6 V cell voltage[10,35] and reached a peak power density of 1016 mW/cm^2, outperforming the PtNWs (1.1 A/cm^2 at 0.6 V and 830 mW/cm^2) and Pt/C (0.67 A/cm^2 at 0.6 V and 773 mW/cm^2). At an even higher current density of 2.5 A/cm^2, PtCoNWs still delivered a power density of 1000 mW/cm^2, while PtNWs only showed a power density of 666 mW/cm^2, comparable to that of Pt/C (626 mW/cm^2). The above power density performance analysis suggested that 1D PtCoNWs showed lower O_2 transport resistance than the nanoparticle Pt/C. We also evaluated the rated power, at which the heat rejection

balance ($Q/\Delta Ti < 1.45$) should be considered for practical operation yet rarely reported and overlooked. The rated power was determined at 0.76 V for cells operated at 80 °C. The PtCoNWs delivered a rated power of 0.37 W/cm^2, which is 5.2 times that of Pt/C (0.071 W/cm^2) and 2.2 times that of the PtNWs (0.17 W/cm^2). This corresponds to an ultrahigh total effective Pt utilization of 5.14 W_{rated}/mg_{Pt} for PtCoNWs, which is 5.4 times that of Pt/C (0.95 W_{rated}/mg_{Pt}), surpassing all the state-of-the-art Pt-alloy catalysts in MEA (Figure 4.6d). The high Pt utilization demonstrated the efficiency of 1D PtCoNW structures in MEA, which can significantly reduce the usage of Pt while delivering high performance in PEMFCs.

We followed the DOE suggested protocol[7] to evaluate the durability of the catalysts by applying the square wave potential cycling between 0.60 and 0.95 V for 30,000 cycles. The PtCoNWs showed an impressive EOL MA of 0.45 A/mg_{Pt}, which is still above the BOL MA target of DOE (0.44 A/mg_{PGM}) (Figure 4.6c). On the other hand, the after AST MA of PtNWs and Pt/C decayed to 0.21 A/mg_{Pt} and 0.1 A/mg_{Pt}, respectively, both below the DOE end of life (EOL) target of 0.26 A/mg_{PGM} (Figure 4.6c). To investigate the degradation behavior, we also performed the characterizations on the catalysts after AST in MEA. Severe aggregation and shape deformation were observed in all catalyst groups. We observed that considerable PtCoNWs maintained the 1D structure, while some tended to evolve into nanoparticles (Figure 4.10b and c), which might contribute to the performance loss. Impressively after AST, the Pt-skin on PtCoNWs still remained as suggested by the inverse FFT and EDX line scan results (Figure 4.11c and g). The mean diameter of PtCoNWs increased from 3.1 ± 0.9 nm to 6.6 ± 1.9 nm (Figure 4.10a and b), leading to a decreased ECSA of 36.2 m^2/g_{Pt} (Figure 4.7), which, however, was still larger than the initial ECSA of Pt/C (33.0 m^2/g_{Pt}). For the PtNWs, a more pronounced morphology

change was observed after AST, where nearly all PtNWs evolved into spherical NPs (4.6 ± 1.2 nm) and showed a low ECSA of 15.4 m^2/g_{Pt} (Figures 4.7, 4.12a and c). Likewise, the Pt/C suffered significant aggregation after AST with average size increasing from 5.3 ± 1.2 nm to 8.8 ± 6.4 nm, and the ECSA dropped from 33.0 m^2/g_{Pt} to 11.7 m^2/g_{Pt} (Figures 4.7, 4.12b and d). In addition to aggregation, the loss of activity could also be partly attributed to the nonoptimal attachment between the catalysts and the carbon support. After AST, the density of nanocatalysts on carbon support apparently decreased (Figures 4.12c), indicating detachment and the loss of catalyst. This problem is commonly reported in the degradation mechanism of fuel cell catalysts.[36-38]

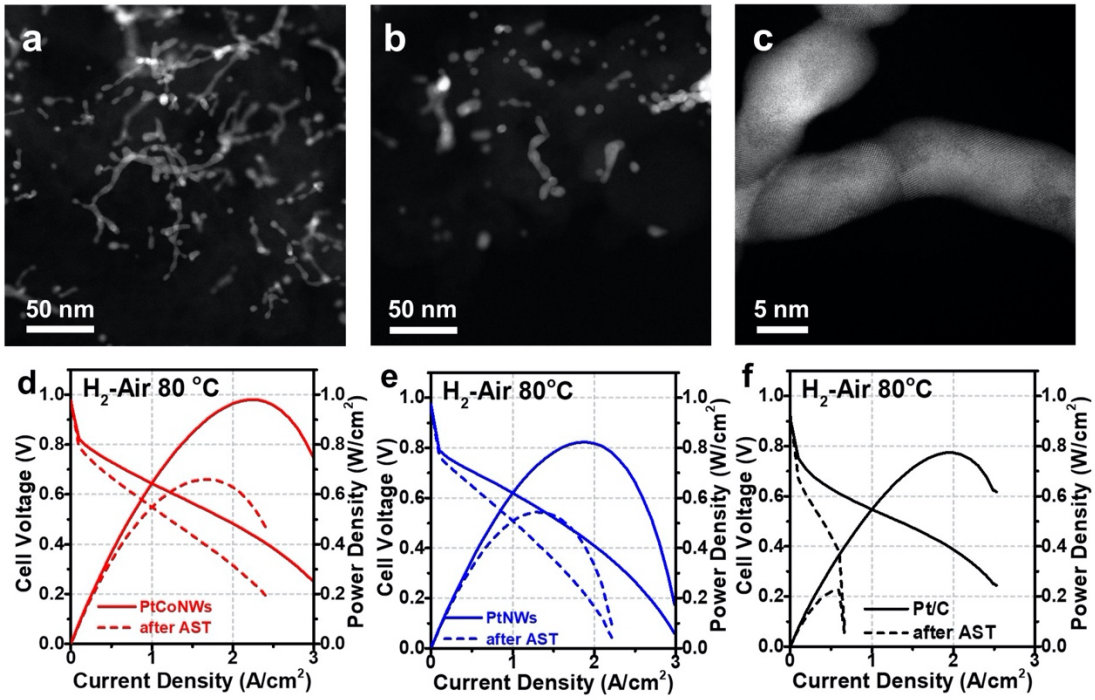

Figure 4.10. Durability analysis of catalysts. (a and b) HAADF-TEM images of PtCoNWs (a) at BOL and (b) at EOL. (c) High-resolution STEM image of PtCoNWs after AST. (d to f) Comparison of H_2-air performance of (d) PtCoNWs, (e) PtNWs, and (f) Pt/C catalysts at the BOL (solid line) and EOL (dashed line) stage.

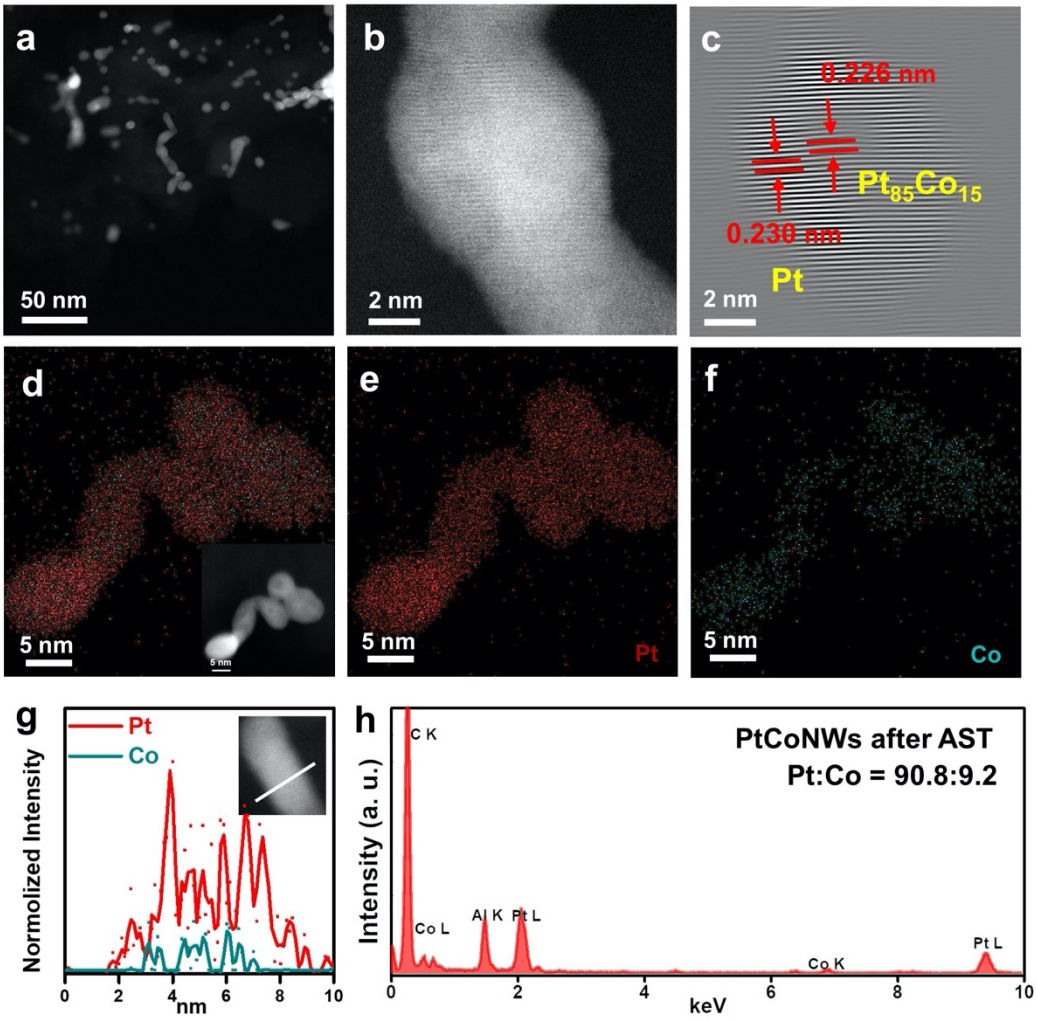

Figure 4.11. Characterizations of the PtCoNWs after the AST. (**a**) STEM low magnification image. (**b**) High resolution STEM image. (**c**) Inverse FFT of the STEM in panel (**b**). (**d, e** and **f**) EDX mapping results. (**g**) EDX line-scan profiles. (**h**) Representative EDX spectrum result.

Overall, both PtCoNWs and PtNWs demonstrated better structural stability than Pt/C. And the PtCoNWs demonstrated much better structural stability compared to Pt/C, which may be attributed to their uniform alloying Pt-Co core. In addition, EDX analysis revealed that PtCoNWs retained most of the Co after AST, where the composition of Co only slightly changed from ca 14% to 9% (Figures 4.11h), indicating composition stability. After AST, the PtCoNWs still delivered a peak power density of 662 mW/cm^2 (Figures 4.10d), while the peak power of PtNWs and Pt/C decayed to 546 mW/cm^2 and 220 mW/cm^2,

respectively (Figures 4.10e and f). 1D NW structures demonstrated much better performance in both MA and power performance compared to nanoparticles (Pt/C), while PtCo alloy demonstrated superiority over pure Pt, confirming the advantages and better structural durability of 1D Pt-alloy catalysts in PEMFC applications. Through the comparison of the structures and compositions of all catalyst groups, it becomes more evident that 1D morphology showed better structural stability than the nanoparticle Pt/C, and that PtCo alloy core further contributed to the higher stability of PtCoNWs, which resulted in the decent activity and power density after AST and can potentially overcome the dilemma between low loading and high-power density.

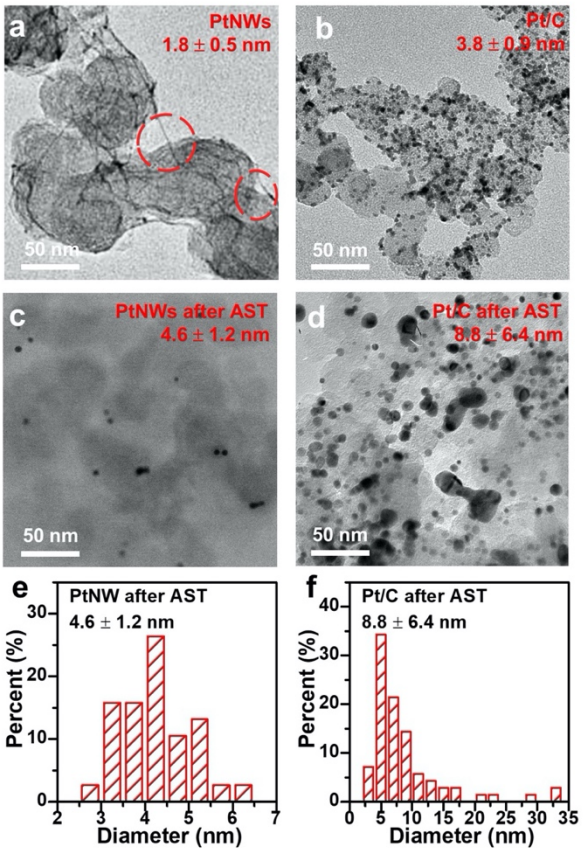

Figure 4.12. MEA stability analysis of the PtNWs and Pt/C. (**a** and **b**) TEM low magnification image of PtNWs and Pt/C before MEA measurements. (**c** and **d**) TEM low magnification image of PtNWs and Pt/C after AST. (**e** and **f**) Size distribution analysis of PtNWs and Pt/C after AST.

4.4 Conclusion

In summary, we demonstrated an ultralow Pt loading and high-performance MEA using ultrathin PtCoNWs. The PtCoNWs showed a high BOL ECSA of 73.2 m^2/g_{Pt}, a record-high MA of 1.06 A/mg_{Pt}, and excellent structural and composition stability in a MEA, outperforming most state-of-the-art Pt-alloy catalysts in MEA reported to date (Table 1) and surpassing DOE set 2020 targets. PtCoNWs also delivered an impressively high Pt utilization of 5.14 W_{rated}/mg_{Pt} at 80 °C, with ultralow Pt loading of 0.047 mg_{Pt}/cm^2, suggesting a valid pathway to overcome the dilemma between low loading and high-power density using ultrathin 1D catalysts.

4.5 References

1. Debe, M. K. Electrocatalyst approaches and challenges for automotive fuel cells. *Nature* **486**, 43-51 (2012).

2. Wang, X. X., Swihart, M. T. & Wu, G. Achievements, Challenges and Perspectives on Cathode Catalysts in Proton Exchange Membrane Fuel Cells for Transportation. *Nat. Catal.* **2**, 578-589 (2019).

3. Kodama, K., Nagai, T., Kuwaki, A., Jinnouchi, R. & Morimoto, Y. Challenges in applying highly active Pt-based nanostructured catalysts for oxygen reduction reactions to fuel cell vehicles. *Nat. Nanotechnol.* **16**, 140-147 (2021).

4. Wu, J. B. & Yang, H. Platinum-based oxygen reduction electrocatalysts. *Acc. Chem. Res.* **46**, 1848-1857 (2013).

5. Whiston, M. M. *et al.* Expert Assessments of the Cost and Expected Future Performance of Proton Exchange Membrane Fuel Cells for Vehicles. *Proc. Natl. Acad. Sci. U. S. A.* **116**, 4899-4904 (2019).

6. Kongkanand, A. & Mathias, M. F. The priority and challenge of high-power performance of low-platinum proton-exchange membrane fuel cells. *J. Phys. Chem. Lett.* **7**, 1127-1137 (2016).

7. DRIVE, U. S. *Fuel Cell Technical Team Roadmap*, <https://www.energy.gov/sites/prod/files/2017/11/f46/FCTT_Roadmap_Nov_2017_FINAL.pdf> (2017).

8. Kriston, A., Xie, T. Y., Gamliel, D., Ganesan, P. & Popov, B. N. Effect of Ultra-Low Pt Loading on Mass Activity of Polymer Electrolyte Membrane Fuel Cells. *J. Power Sources* **243**, 958-963 (2013).

9. Fan, J. *et al.* Bridging the gap between highly active oxygen reduction reaction catalysts and effective catalyst layers for proton exchange membrane fuel cells. *Nat. Energy* **6**, 475-486 (2021).

10. Tian, X. L. *et al.* Engineering Bunched Pt-Ni Alloy Nanocages for Efficient Oxygen Reduction in Practical Fuel Cells. *Science* **366**, 850-856 (2019).

11. Li, J. R. *et al.* Hard-Magnet $L1_0$-CoPt Nanoparticles Advance Fuel Cell Catalysis. *Joule* **3**, 124-135 (2019).

12. Liu, Z. Y., Zhao, Z. P., Peng, B. S., Duan, X. F. & Huang, Y. Beyond Extended Surfaces: Understanding the Oxygen Reduction Reaction on Nanocatalysts. *J. Am. Chem. Soc.* **142**, 17812-17827 (2020).

13. Li, M. F. *et al.* Ultrafine Jagged Platinum Nanowires Enable Ultrahigh Mass Activity for the Oxygen Reduction Reaction. *Science* **354**, 1414-1419 (2016).

14. Sandbeck, D. J. S. *et al.* The Dissolution Dilemma for Low Pt Loading Polymer Electrolyte Membrane Fuel Cell Catalysts. *J. Electrochem. Soc.* **167** (2020).

15. Lu, Y. X., Du, S. F. & Steinberger-Wilckens, R. One-Dimensional Nanostructured Electrocatalysts for Polymer Electrolyte Membrane Fuel Cells-A Review. *Appl Catal B-Environ* **199**, 292-314 (2016).

16. Chen, Y., Cheng, T. & Goddard III, W. A. Atomistic Explanation of the Dramatically Improved Oxygen Reduction Reaction of Jagged Platinum Nanowires, 50 Times Better than Pt. *J. Am. Chem. Soc.* **142**, 8625-8632 (2020).

17. Fuchs, T. *et al.* Structure dependency of the atomic-scale mechanisms of platinum electro-oxidation and dissolution. *Nat. Catal.* **3**, 754-761 (2020).

18. Bu, L. Z. *et al.* Surface Engineering of Hierarchical Platinum-Cobalt Nanowires for Efficient Electrocatalysis. *Nat. Commun.* **7** (2016).

19. Jiang, K. Z. *et al.* Efficient Oxygen Reduction Catalysis by Subnanometer Pt Alloy Nanowires. *Sci. Adv.* **3**, 1-8 (2017).

20. Stephens, I. E. L., Rossmeisl, J. & Chorkendorff, I. Toward sustainable fuel cells. *Science* **354**, 1378 (2016).

21. Sievers, G. W. *et al.* Self-Supported Pt-CoO Networks Combining High Specific Activity with High Surface Area for Oxygen Reduction. *Nat. Mater.* (2020).

22. Arruda, T. M., Shyam, B., Ziegelbauer, J. M., Mukerjee, S. & Ramaker, D. E. Investigation into the competitive and site-specific nature of anion adsorption on Pt using in situ X-ray absorption spectroscopy. *J. Phys. Chem. C* **112**, 18087-18097 (2008).

23. Jia, Q. *et al.* Activity descriptor identification for oxygen reduction on Platinum-based bimetallic nanoparticles: *in situ* observation of the linear composition–strain–activity relationship. *ACS Nano* **9**, 387-400 (2015).

24. Newville, M. IFEFFIT: interactive XAFS analysis and FEFF fitting. *J Synchrotron Radiat* **8**, 322-324 (2001).

25. Ravel, B. & Newville, M. ATHENA, ARTEMIS, HEPHAESTUS: data analysis for X-ray absorption spectroscopy using IFEFFIT. *J. Synchrotron Radiat.* **12**, 537-541 (2005).

26. Newville, M., Līviņš, P., Yacoby, Y., Rehr, J. J. & Stern, E. A. Near-edge x-ray-absorption fine structure of Pb: A comparison of theory and experiment. *Phys. Rev. B* **47**, 14126-14131 (1993).

27. Ankudinov, A. L., Ravel, B., Rehr, J. J. & Conradson, S. D. Real-space multiple-scattering calculation and interpretation of x-ray-absorption near-edge structure. *Phys. Rev. B* **58**, 7565-7576 (1998).

28. Hlil, E. K., BaudoingSavois, R., Moraweck, B. & Renouprez, A. J. X-ray absorption edges in platinum-based alloys. 2. influence of ordering and of the nature of the second metal. *J. Phys. Chem.* **100**, 3102-3107 (1996).

29. Jia, Q. Y. *et al. In Situ* Spectroscopic Evidence for Ordered Core–Ultrathin Shell Pt_1Co_1 Nanoparticles with Enhanced Activity and Stability as Oxygen Reduction Electrocatalysts. *J. Phys. Chem. C* **118**, 20496-20503 (2014).

30. Hwang, B. J. *et al.* Structural Models and Atomic Distribution of Bimetallic Nanoparticles as Investigated by X-ray Absorption Spectroscopy. *J. Am. Chem. Soc.* **127**, 11140-11145 (2005).

31. Kim, H. Y. *et al.* Activity Origin and Multifunctionality of Pt-Based Intermetallic Nanostructures for Efficient Electrocatalysis. *ACS Catal.* **9**, 11242-11254 (2019).

32. Wang, Z. X. *et al.* Structurally Ordered Low-Pt Intermetallic Electrocatalysts toward Durably High Oxygen Reduction Reaction Activity. *Adv. Funct. Mater.* **29** (2019).

33. Han, B. H. *et al.* Record Activity and Stability of Dealloyed Bimetallic Catalysts for Proton Exchange Membrane Fuel Cells. *Energy Environ. Sci.* **8**, 258-266 (2015).

34. Mardle, P., Thirunavukkarasu, G., Guan, S. L., Chiu, Y. L. & Du, S. F. Comparative Study of PtNi Nanowire Array Electrodes toward Oxygen Reduction Reaction by Half-Cell Measurement and PEMFC Test. *ACS Appl. Mater. Interfaces* **12**, 42832-42841 (2020).

35. Chong, L. *et al.* Ultralow-loading platinum-cobalt fuel cell catalysts derived from imidazolate frameworks. *Science* **362**, 1276 (2018).

36. Shao, Y. Y., Yin, G. P. & Gao, Y. Z. Understanding and Approaches for the Durability Issues of Pt-Based Catalysts for PEM Fuel Cell. *J. Power Sources* **171**, 558-566 (2007).

37. Beermann, V. *et al.* Real-Time Imaging of Activation and Degradation of Carbon Supported Octahedral Pt-Ni Alloy Fuel Cell Catalysts at the Nanoscale Using *In situ* Electrochemical Liquid Cell STEM. *Energy Environ. Sci.* **12**, 2476-2485 (2019).

38. Takao, S. *et al.* Observation of Degradation of Pt and Carbon Support in Polymer Electrolyte Fuel Cell Using Combined Nano-X-ray Absorption Fine Structure and Transmission Electron Microscopy Techniques. *ACS Appl. Mater. Interfaces* **10**, 27734-27744 (2018).

Chapter 5. Surface molecular modification for ORR catalysts

5.1 Introduction

The requirement of the costly platinum (Pt)-based catalysts for the sluggish oxygen reduction reaction (ORR) represents the key bottleneck for widespread adoption of proton-exchange membrane fuel cells (PEMFCs)[1-3]. Intensive efforts have been devoted to searching for ORR catalysts with higher catalytic activity[3-6] and longer-term stability[7,8]. Given that Pt binds oxygen stronger than the optimum value[9], strain effect[4,10] and ligand effect[3,11] have been widely adopted to modulate the Pt-O binding energy, therefore lowering the ORR overpotential. Despite considerable progress, enhancing the performance of ORR catalysts via structures and compositions may not be sufficient to satisfy the activity and stability requirement for fuel cells. which signifies the need for further advances. Fundamentally, the specific activity (SA) of ORR does not only correlate with the Gibbs adsorption energy[12], but also the concentration of O_2 at the active site[13,14]. Importantly, these two factors are not mutually exclusive, which can cumulatively enhance the ORR kinetics. According to Le Chatelier's principle[15], increased O_2 solubility of the electrolyte or a higher local O_2 concentration could lead to further activity enhancement. In parallel, expelling product water would also accelerate overall kinetics. However, oxygen solubility in the water-based electrolyte is too low to allow adequate contact with Pt surface, which largely impedes the overall kinetics[15]. To overcome this dilemma, hydrophobic ionic liquids (ILs) with a higher O_2 solubility (ca. 2.4 times compared to that of $HClO_4$) have been proved to successfully speed up the ORR kinetics[14-16]. However, the high cost of ILs adds an additional economic penalty to fuel cells[16]. To date, the exploration of increasing O_2 concentration at the active site is rare, which calls for low-cost and highly efficient approaches.

Tailoring the interfacial configuration can directly modulate the interfacial properties and composition[17-21] to achieve high local O_2 concentration. Recently, surface modification with non-covalent cations[22], pyridine[23], melamine[24], and tetrahexylammonium cations[25] on Pt surface have shown to effectively improve ORR kinetics. However, the underlying mechanism for the enhanced activity remains elusive. In addition, the stability of surface-modified catalysts, which is essential for practical applications, is insufficiently explored to date. These intractable challenges greatly limit the development of the surface modification approach. Herein, we developed a controllable molecular surface modification approach using dimethylformamide (DMF) to greatly boost the ORR performance of Pt-based catalysts. From outset, our molecular dynamics (MD) simulations reveal that surface adsorbed DMF could disrupt interfacial water hydrogen-bonding networks (Figure 5.1), therefore allowing accelerated water exchange kinetics, facilitating O_2 transport towards Pt surface, leading to an increased interfacial oxygen concentration and adsorption time to enable greatly enhanced ORR activity. We further applied this approach to a model Pt-alloy catalysts (PtCuNi), and achieve an unprecedented SA of 21.8 ± 2.1 mA/cm^2 at 0.9 V versus the reversible hydrogen electrode (RHE), about 2.65 times improvement comparing to original PtCuNi catalysts, and nearly double previous record in literature, leading to an ultrahigh mass activity (MA) of 10.7 ± 1.1 A/mg$_{Pt}$. Importantly, after 20,000 cycles of accelerated degradation test (ADT), modified PtCuNi catalysts showed even better SA and MA than the initial performance of original PtCuNi, suggesting that surface adsorbed ligand can considerably extend catalyst lifetime.

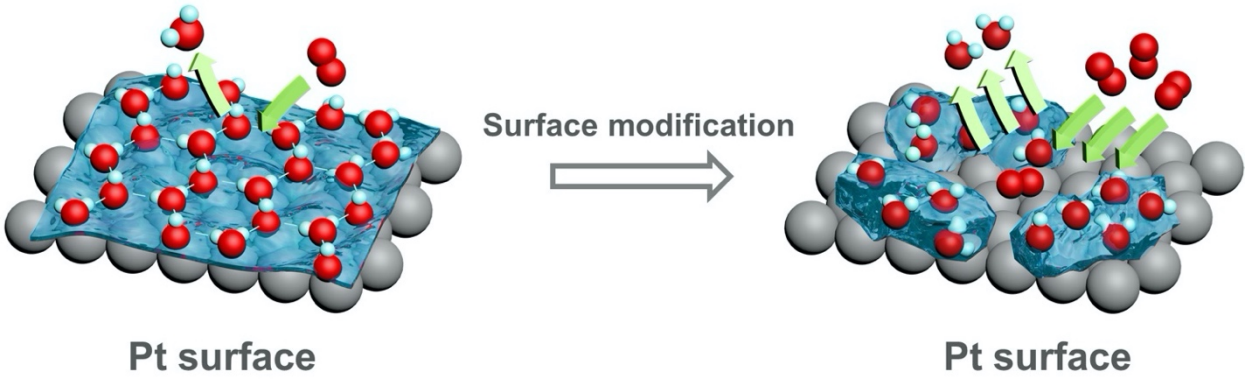

Figure. 5.1. Schematic illustration of Pt surface with selected molecular ligand. The application of surface molecular ligand (DMF) can break the water adlayer network, facilitating O_2 and water transport and leading to high local O_2 concentration. Grey atoms represent Pt(111) surface sites, red atoms represent O, blue atoms represent H.

5.2 Methods

5.2.1 Experimental methods

Materials and Chemicals

Platinum(II) acetylacetonate ($Pt(acac)_2$, 97%), nickel(II) acetylacetonate ($Ni(acac)_2$, 95%), copper (II) acetate ($Cu(AC)_2$, 97%), perchloric acid ($HClO_4$, 70%, PPT Grade), glucose, oleylamine [OAm; $CH_3(CH_2)_7CH{=}CH(CH_2)_7CH_2NH_2$, >70%], 1-octadecene [ODE; $CH_2{=}CH(CH_2)_{15}CH_3$; technical grade, >90%], 5 wt % Nafion were all purchased from Sigma-Aldrich. Commercial Pt/C catalyst (40 wt% Pt) were purchased from Alfa Aesar. N, N-dimethylformamide (DMF, ≥99.8%), ethanol (200 proof), cyclohexane (C_6H_{12}; analytical reagent, >99.5%) were obtained from EMD Millipore and Decon. Isopropanol (≥99.5%) were purchased from Fisher Scientific. All reagents were used as received without further purification. Carbon black (Vulcan XC-72) was received from Carbot Corporation and annealed in 280 ℃ air before used. The deionized water (18 MΩ/cm) was obtained from an ultra-pure purification system (Milli-Q advantage A10). Ultrahigh purity CO was purchased from Airgas, Inc.

Preparation of PtCuNi catalysts

The synthesis of PtCuNi catalysts is similar to a previous report[26]. In a typical preparation of PtCuNi catalysts, $Pt(acac)_2$ (20 mg), $Cu(AC)_2$ (6 mg), $Ni(acac)_2$ (6 mg), glucose (135 mg), OAm (3 ml), and ODE (2 ml) were added into a vial (volume, 35 ml). The mixture was ultrasonicated for 1 hour and then purged with ultrahigh purity carbon monoxide (CO) for 5 minutes and heated from room temperature to 170 °C in 30 minutes and kept at 170 °C for 12 hours in an oil bath with stirring of 300 r.p.m. The colloidal products were collected by centrifugation and washed with cyclohexane/ethanol (v/v = 1:5) mixture for two times. The PtCuNi catalysts were loaded onto 20 mg of carbon black (Vulcan XC-72) by sonication for 2 hours. The as-prepared PtCuNi catalysts were suspended in 20 mL cyclohexane/ethanol (v/v = 1:1) mixture. To load the sample onto carbon black, 20 mg of carbon black was added and sonicated for 2 hours. The resulting catalysts were collected by centrifugation, washed with cyclohexane/ethanol mixture, and annealed at 130 °C for 6 hours in a home-build tube furnace with 100 sccm Ar flow.

Application of surface-modified on PtCuNi catalyst and Pt/C catalyst

The resulting dried PtCuNi catalysts or as-received Pt/C catalysts were first dispersed DMF with a concentration of 1 mg/mL and ultrasonicated for 20 minutes. The resulting solution was heated with magnetic stirring in an oil bath at 120 ℃ for desired time. After the modification, the resulting catalysts were washed with IPA three times and further dried in a vacuum dryer.

Structure and composition characterization

High-resolution TEM images (HRTEM), energy-dispersive X-ray spectroscopy (EDX) line-scan file and the high-angle annular dark-field scanning transmission electron microscope (HAADF-STEM) images were taken on JEM-ARM300F Grand ARM Transmission Electron Microscope operated at 300 kV. TEM samples were prepared by dropping ethanol dispersion of catalysts onto carbon-coated aluminum TEM grids (Ted Pella, Redding, CA). The Pt loading of

catalysts was determined by the inductively coupled plasma atomic emission spectroscopy (ICP-AES). The Pt loading is determined before electrochemical measurement. X-ray photoelectron spectroscopy (XPS) tests were carried out on a Kratos AXIS Ultra DLD spectrometer. All samples were electrochemically activated prior to XPS tests.

Electrochemical measurements

A three-electrode cell system was used to conduct all electrochemical tests. The working electrode was a glassy carbon rotating disk electrode (RDE) with a 0.196 cm^2 glassy carbon geometry area from Pine Instruments. The counter and reference electrodes are Pt wire and Ag/AgCl (1 M Cl^-). For activity measurement, Pt loadings were 10.2 $\mu g/cm^2$ and 7.85 $\mu g/cm^2$ for Pt/C catalysts and all PtCuNi catalysts. Cyclic voltammetry (CV) activations were performed in N_2-saturated 0.1 M $HClO_4$ electrolyte with potential scan rate of 100 mVs^{-1}. Electrochemical active surface area (ECSA) determined by H_{upd} was calculated by integrating hydrogen adsorption charge on CV curve by taking a value of 210 $\mu C/cm^2$ for the adsorption of a hydrogen monolayer. Oxygen reduction reaction (ORR) was tested in an O_2-saturated 0.1 M $HClO_4$ electrolyte with a potential scan rate of 20 mV/s. The measurement temperature was set at 25 ℃ using a water bath 5-neck flask. The current density of ORR polarization curve was iR-corrected during the measurements. The accelerated durability test (ADT) was done at room temperature in O_2-saturated 0.1 M $HClO_4$ solutions by applying CV sweep between 0.6 and 1.1 V versus RHE at a sweep rate of 100 mVs^{-1} for 20,000 cycles. ORR tests were performed before the stability test, after 20,000 cycles of ADT.

5.2.2 Computational methods

All atom/molecule models, including platinum, DMF molecules, oxygen molecules, perchloride anions, hydronium cations, and water molecules (flexible SPC water model), were

prepared using the Materials Studio program[27]. A Pt(111) slab with six Pt layers and box size of 27.74 × 24.03 × 42.00 $Å^3$ were established for DMF adsorption simulations. The zone above the Pt layers was filled with DMF molecules. The model was composed of 175 DMF molecules and 600 Pt atoms. In order to correlate with the synthetic conditions, no water was included, and the simulation temperature was set at 393.15 K (equivalent to 120 °C, synthetic temperature). The (isothermal-isobaric ensemble) NPT ensemble was carried out for the simulation under 1 atm for 8 ns to reach equilibrium. Finally, the flat conformation of DMF located on Pt(111) surface was considered the stable adsorption model. To probe into the monolayer coverage of DMF on Pt(111) surface. A 6-layer Pt(111) slab with dimensions of 27.74×24.03×45.00 $Å^3$ (in total 600 Pt atoms) was set up. 20 or 21 DMF molecules were placed flat on Pt surface respectively and the zone above Pt surface was kept vacuum. The (canonical ensemble) NVT ensemble was applied for the simulation, which lasted for 8 ns at 298.15 K (electrochemical testing conditions). The structure with all the DMF molecules lying flat on Pt(111) was regarded as simulated monolayer (ML) coverage. For further simulations, the corresponding number of DMF molecules at different surface coverages was calculated for different Pt surface areas. The adsorption of oxygen molecules on Pt(111) surface was investigated with oxygen supersaturation models, which can result in enough adsorption statistics. The oxygen adsorption models had the same size of 69.36×62.47×53.00 $Å^3$ with 3900 Pt atoms (6 layers), 100 oxygen molecules (equivalent to 1 M), 10 perchloride anions (equivalent to pH = 1), 10 hydroniums (equivalent to pH = 1) and 5557 water molecules (flexible SPC model). Only the number of DMF varied for different systems. Five systems with DMF coverage equaled ML = 0, 0.1, 0.3, 0.5, and 0.7 respectively, were chosen as the representative coverages to compare with experimental results. In the meantime, the corresponding DMF number in the above systems were 0, 13, 39, 65, and 91.

Molecular Dynamics Simulations protocols

We applied nanoscale molecular Dynamics (NAMD) for all the adsorption simulations[28]. CHARMM-based INTERFACE force field (IFF) parameters were assigned for Pt atoms, oxygen molecules, perchloride anions, and hydroniums cations, while CHARMM36 parameters were granted to DMF and SPC water molecules. IFF is based on a classical Hamiltonian, including parameters for inorganic and organic compounds with systematic validation of chemical bonding (polarity), structure, and energy[29,30]. FCC metals were described by thermodynamically consistent Lennard-Jones (LJ) parameters. The IFF parameters for molecular oxygen reproduce the liquid density, vaporization energy (at boiling point and 1 atm), and solvation free energy (at room temperature) within a 3% deviation from experimental measurements.[31] For oxygen adsorption studies, all the simulations were first equilibrated for 1 ns using NPT ensemble (the pressure was set at 1 atm) and then conducted with NVT ensemble for 50 ns in total under periodic boundary conditions. The trajectory was collected every 1 ps with simulation timestep of 1 fs, with PME tolerance of 0.001 and the summation of Lennard-Jones interactions cutoff at 1.2 nm to acquire abundant dynamics of oxygen adsorption events on Pt(111) surface. The temperature was maintained at 298.15 K for both NPT and NVT ensemble, consistent with electrochemical testing conditions.

Analysis of oxygen/water adsorption on the surface

The trajectories were analyzed by self-developed Python code with the MD Analysis package[32,33]. The analyses were performed on the equilibrated trajectories from 10 ns to 50 ns for all models, which means analyzing 40000 frames for each system. Typically, a distance of 3.5 Å between Pt and oxygen/water was regarded as a criterion for adsorption calculations.[31] For the analyses of adsorption time, only those with time larger than 0 ns were regarded as valid adsorption.

For example, the total adsorption time was calculated for each oxygen molecule on the basis of the summation all the frames with Pt coordination numbers larger than 0. The average adsorption time was estimated by dividing the total oxygen molecule number. Root mean square and standard deviation were applied to the calculation results of average adsorption time. Electrochemical double layer (EDL) was defined with a cutoff of 5 Å above the Pt(111) surface, where the oxygen concentration and exposure in such interfacial zone is very important for electrochemical reactions. Oxygen concentration was defined as the number of oxygen molecules per unit volume within the EDL, while the oxygen exposure flux was the number of exposed oxygen molecules within the EDL in unit area and time.

Calculation of adsorption free energy profiles

The free energy profiles of oxygen adsorption were obtained by steered molecular dynamics (SMD) simulations with the Large-scale Atomic/Molecular Massively Parallel Simulator (LAMMPS) program[34]. Pt(111) slabs with or without DMF were respectively constructed for SMD simulations. The box size was maintained to be 29.969 × 24.027 × 65.550 $Å^3$, and was infinite in the lateral dimensions using 3D periodic boundary conditions. DMF molecules with 50% surface coverages were placed flatly on the Pt(111) surface correlating with the MD results. The systems contained 1000 explicit water molecules (using flexible SPC water model) and only one target oxygen molecule. The initial position of the target oxygen molecule was at least 12 Å (Z direction) away from the platinum surface atomic layer. A force and constant velocity were exerted on the target oxygen molecule so that it was able to move towards to the Pt(11) surface at a slow speed. Note no hydronium ions were involved to represent the acid conditions because hydronium ions can interact with the steered molecule during the pulling process and lead to poor sampling. The free energy was sampled using 1 Å/ns velocity in the bulk

region. When the target molecule approached the surface (~6 Å or less from the surface atomic layer), a very slow pulling velocity of 0.03 Å/ns was set to achieve sufficient sampling within the metal-water interface region. The most suitable velocity was selected as a trade-off according to between the different metal-water-adsorbate interfacial interactions and computation costs. The selected velocity was slow enough for every system to reach equilibrium at every time step to simulate a reversible process. For water adlayers with a discontinuity to bulk water, a slow pulling velocity as given above is necessary to obtain an accurate free energy profile. To avoid movement of the platinum slab, the bottom atomic layer of the slab was constrained in the pulling direction of the target molecules while mobile in the other directions. The simulation systems were first pre-equilibrated for 1 ns in NPT ensemble and then in the NVT ensemble to carry out the SMD runs. The trajectory frames and the corresponding free energies were collected every 1 ps in bulk and every 0.5 ps within 6 Å from the surface atomic layer. The Visual Molecular Dynamics (VMD) program was used to determine the distance between the geometric center of the target oxygen molecule and the surface atomic layer at each frame. The reported free energy profiles were generated by converting the free energies for all frames with a function of the distances between the target molecule and surface atomic layer.

5.3 Results and discussion

Surface molecular modification on Pt/C catalyst.

We first used commercial Pt/C catalysts as a model system to explore the surface modification effect. The Pt/C catalyst (40% wt Pt, Alfa Aesar) was modified in a pure DMF solution with controlled time to exert the surface molecular adsorption as DMF is a commonly used solvent and can maintain stable within a wide potential window[35]. We first performed cyclic

voltammetry (CV) and compare the electrochemically active surface area (ECSA) according to hydrogen underpotential deposition (H_{upd}) area (Figure. 5.2a). Intriguingly, Pt/C catalysts began with an ECSA of 51.6 ± 1.5 m^2/g_{Pt} and continuously decreased to 21.8 ± 0.2 m^2/g_{Pt} after 48 hours modification (Figure. 5.2b, d) due to the block of available surface sites with increasing DMF surface coverage.

To further investigate and compare the surface status, we carried out the X-ray photoelectron spectroscopy (XPS) study (Figures. 5.2c, 5.3). The XPS studies showed that the N-containing species increased with modification time, consistent with increasing adsorption of DMF and reducing ECSA (Figure. 5.2b). The position of XPS peaks didn't shift during the modification, suggesting that the surface-modified ligand didn't induce an obvious electronic effect on Pt (Figure. 5.3). The ORR activities of Pt/C catalysts were further evaluated using the linear sweep voltammetry (LSV) method (Figure. 5.2c). The SA of Pt/C catalysts increased from 0.48 ± 0.06 mA/cm^2 to 0.89 ± 0.04 mA/cm^2 after 24 hours modification (surface coverage of 37.1%) and then decreased to 0.55 ± 0.02 mA/cm^2 after 48 hours modification (surface coverage of 58.0%) (Figure. 5.2d). Accordingly, the MA of Pt/C catalyst increased from 0.23±0.03 A/mg_{Pt} to 0.28±0.03 A/mg_{Pt} after 24 hours modification, corresponding to an optimal enhancement of 20% (Figure. 5.2d). The above interesting experimental results led us to perform a further in-depth investigation to understand the role of DMF and the status of catalyst-electrolyte interfaces.

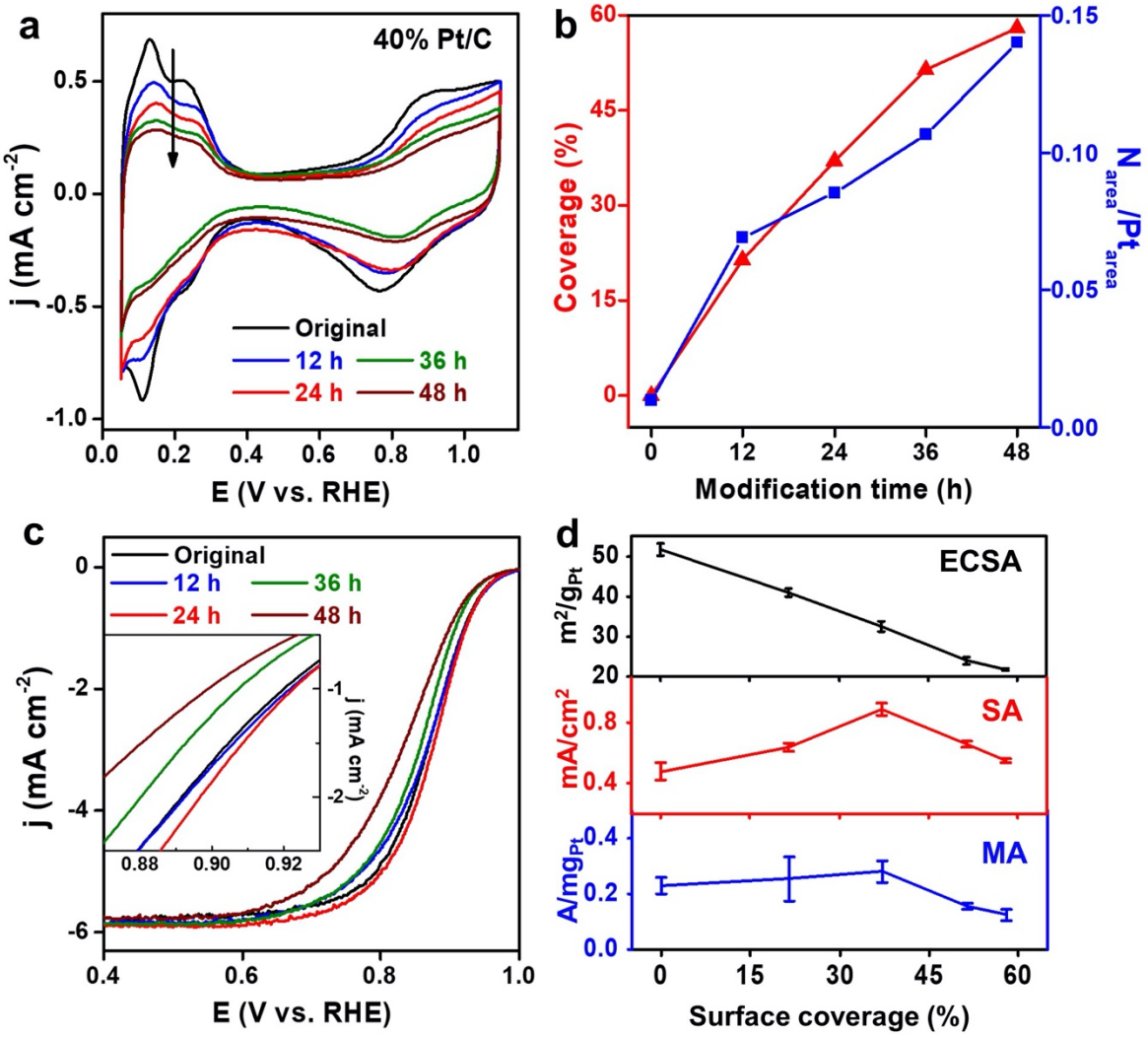

Figure 5.2. Electrochemical measurements of the Pt/C catalysts in 0.1 M $HClO_4$ electrolyte at different modification time in DMF. (**a**) CV curves of Pt/C catalysts at original stage (black), 12 hours (blue), 24 hours (red), 36 hours (green), and 48 hours (wine) modification time. (**b**) Surface coverage derived from ECSA and N/Pt ratio obtained from XPS peak integration as a function of modification time. (**c**) ORR LSV curves of Pt/C catalysts at original stage (black), 12 hours (blue), 24 hours (red), 36 hours (green), and 48 hours (wine) modification time. The inset of the panel (**c**) is the enlarged potential region. (**d**) The evolution of ECSA (black), SA (red), and MA (blue) with surface DMF coverage.

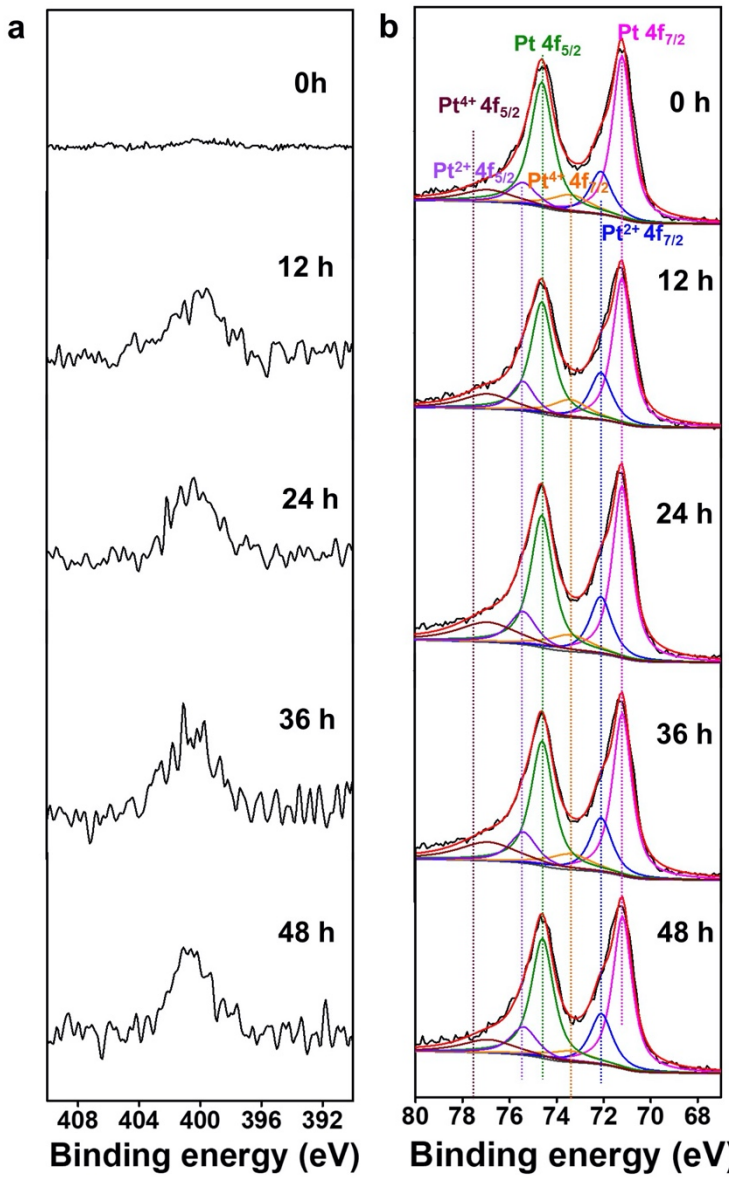

Figure 5.3. (**a**) XPS N 1s spectra of commercial Pt/C catalysts and (**b**) XPS Pt 4f spectra of Pt/C catalysts at different modification time.

MD simulations of interfacial properties.

We carried out interface force field (IFF)-based MD simulations on a representative Pt(111) slab in 0.1 M $HClO_4$ electrolyte to compare the oxygen and water adsorption behavior at different DMF surface coverages (from 0 to 70%) (Figure 5.4). It was found that DMF molecules preferred

to be flatly adsorbed on Pt(111) surface (Figure 5.4). which may disrupt the interfacial water adlayer structure. We further analyzed the average H-bonds of H_2O (Figure 5.5). It was found that the average H-bonds of each H_2O at interfacial layer decreased from 1.02 to 0.89 when DMF coverage reached 50%, and further decreased to 0.70 with 90% DMF coverage, indicating the break of water network due to the DMF adsorption (Figure 5.6a). We suspected that the disruption of the water network would lead to the change of interfacial configuration and composition of the interfacial layer. Therefore, we further investigated the concentration and behavior of species (O_2 and H_2O) at the interface. The interfacial O_2 concentration ($C(O_2)$) increased from 0.29 to 0.69 nm^{-3} as DMF coverage reached 50% (Figure 5.6b), corresponding to about 2.4 times enhancement and comparing reasonably to the experimental SA enhancement (1.9 times). In addition, the water concentration was also affected, which decreased from 30.1 nm^{-3} to 12.6 nm^{-3} when DMF coverage reached 70% (Figure 5.7a). With the increase of DMF coverage, the overall distribution of adsorbed O_2 extends to longer adsorption time with a maximum of 30 ns (Figure 5.8), leading to increased averaged O_2 adsorption time (Figure 5.6c). The average adsorption time of H_2O was calculated following the similar statistic calculation process (Figure 5.7b). Interestingly, the average adsorption time of H_2O declined from 3.5 to 1.5 ns with increased DMF coverage (Figure 5.7b). Therefore, Pt surface with appropriate DMF coverage is likely to have a higher interfacial O_2 concentration and lower water concentration, both can improve the ORR kinetics based on Le Chatelier's principle[36].

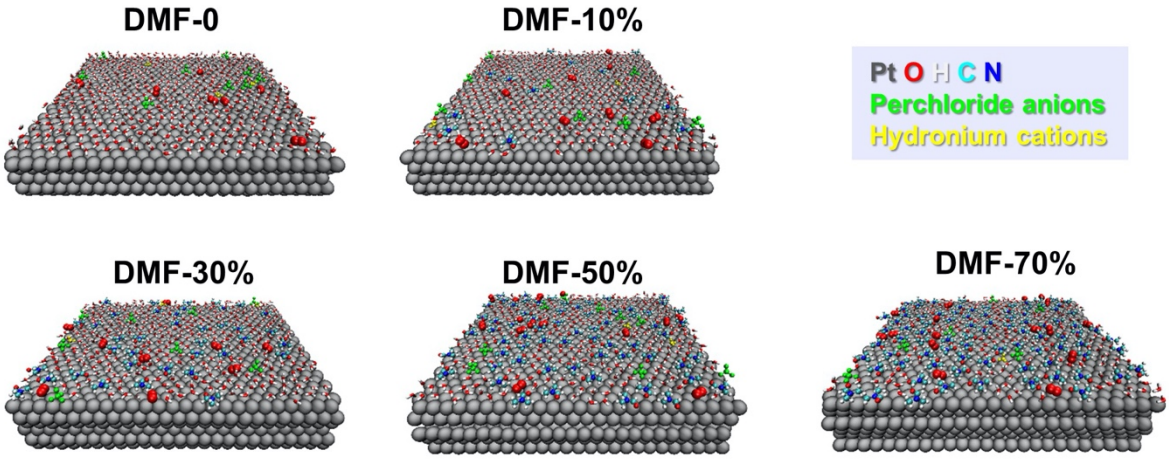

Figure 5.4. Snapshots of the Pt(111) surface with different DMF coverage percentages at the simulation time of 50 ns. Molecules above the adlayer were hidden for clarity.

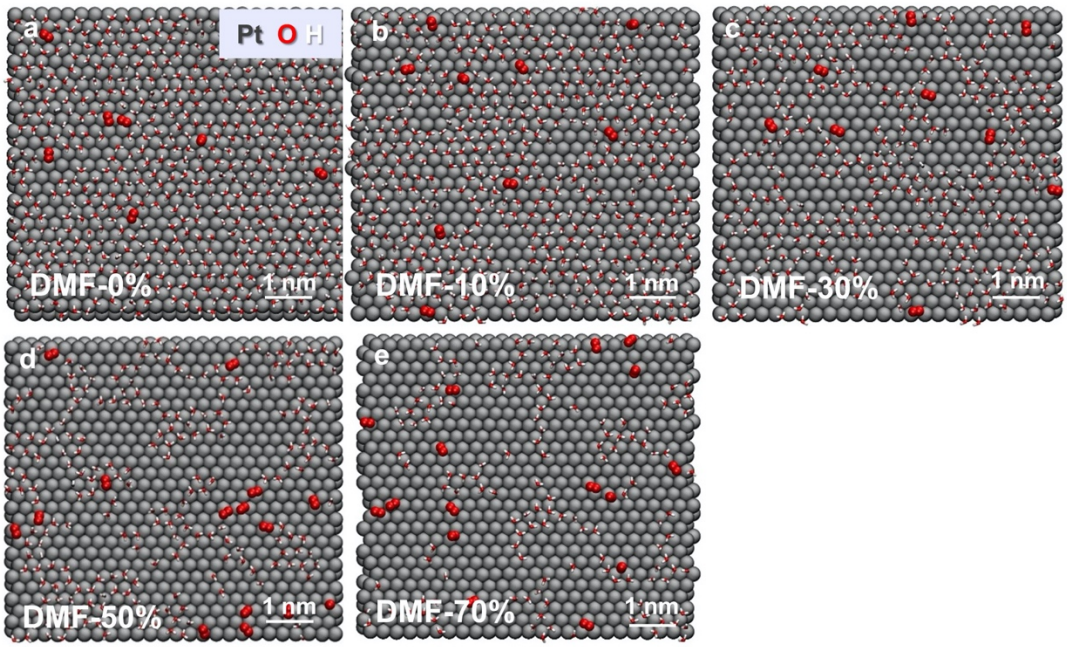

Figure 5.5. (**a-e**) Schematics of water and O_2 distribution at adlayer at a simulation time of 50 ns DMF, hydronium cations, and ClO_4^- anions are hidden to show the configuration of the broken water adlayer. For the hydrogen bonding calculation, a degree of 30° and a distance of 3.5 Å was applied as the criterion. The average H-bonds for each H_2O was calculated by dividing the total formed H-bonds number by the total H_2O number at adlayer. The error bar represents the standard error of the mean.

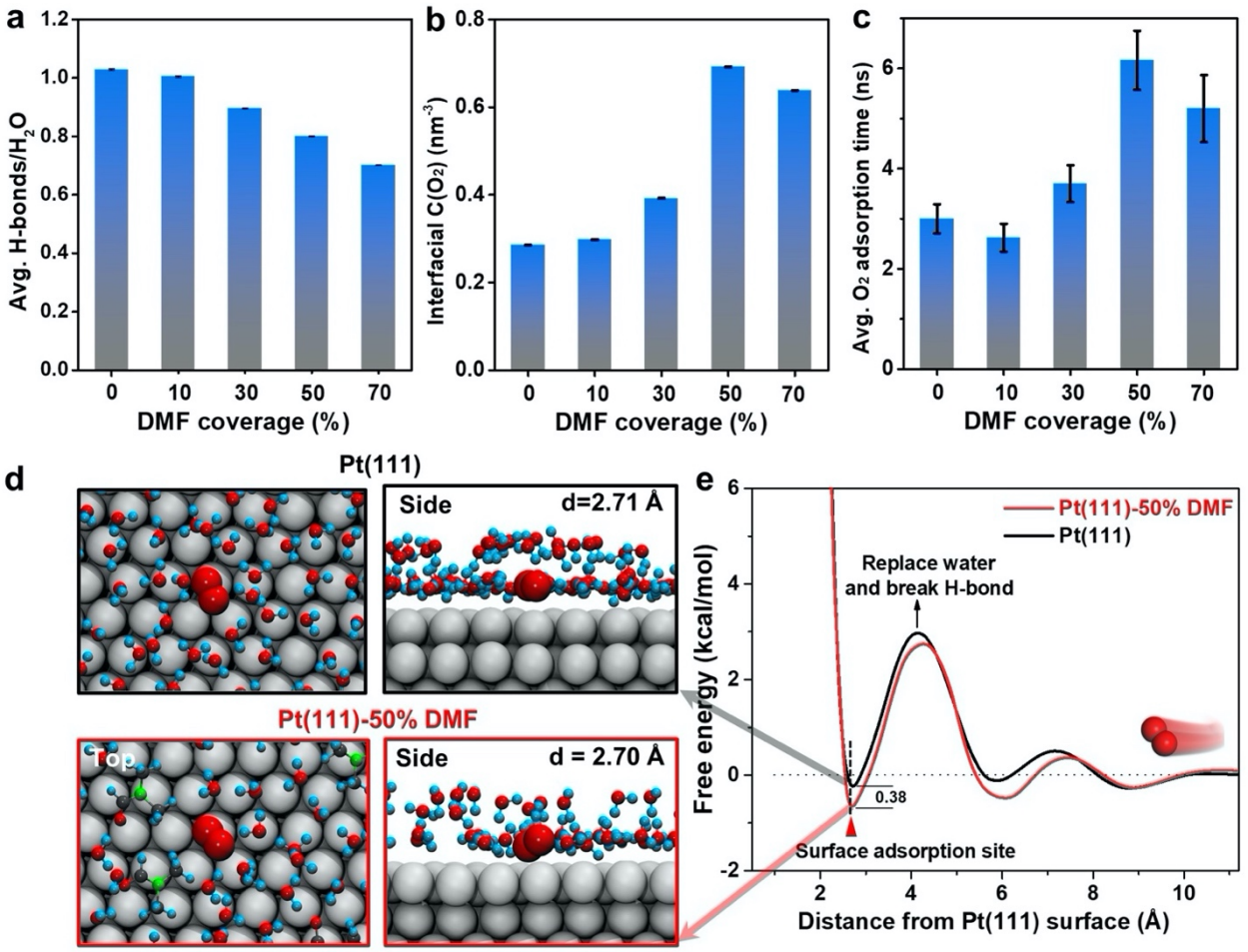

Figure 5.6. MD simulation analysis of the catalyst-electrolyte interface. (**a-c**) The relationship between surface DMF coverage and (**a**) average H-bonds of each water (**b**) interfacial O_2 concentration ($C(O_2)$), and (**c**) average O_2 adsorption time. (**d**) Top and side views of the Pt(111) surface and Pt(111)-50% DMF surface, suggesting that DMF disrupts the water adlayer integrity. DMF molecules at the side view of Pt(111)-50% DMF surface are hidden to show the water layer configuration. (**e**) Comparison of adsorption free energy diagram of the O_2 molecule for Pt(111) surface and Pt(111)-50% DMF surface. The O_2 molecule is approaching the Pt(111) from Z-direction. The gray, blue, red, green, and black spheres represent Pt, H, O, N and C, respectively. The error bar represents the standard error of the mean. The interfacial O_2 concentration ($C(O_2)$) is defined as the number of O_2 per unit volume of the electrochemical double layer (EDL) of 0.5 nm thickness[37]. For the hydrogen bonding calculation, a degree of 30° and a distance of 3.5 Å was applied as the criterion. The average H-bonds for each H_2O was calculated by dividing the total formed H-bonds number by the total H_2O number at adlayer.

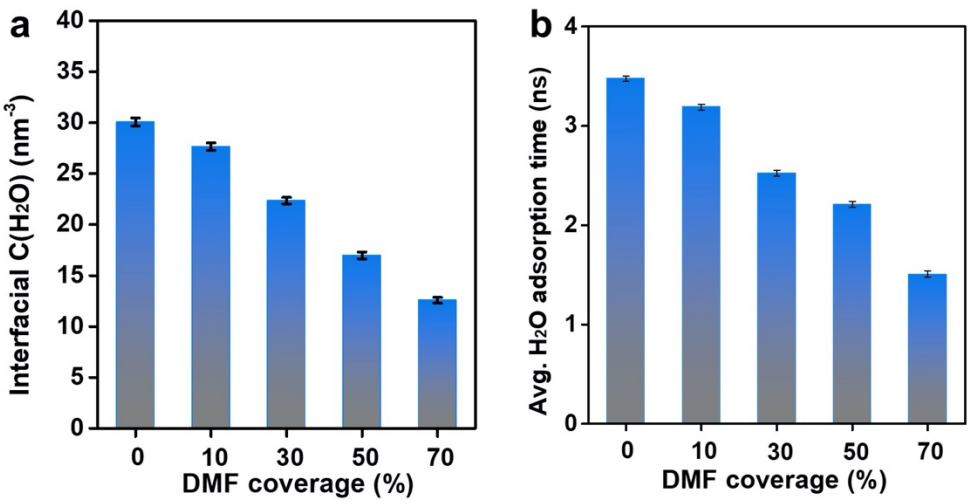

Figure 5.7. Statistic analysis of interfacial H_2O concentration and average H_2O adsorption time at different DMF coverages. The error bar represents the standard error of the mean. The average H_2O adsorption is inversely proportional to the DMF coverage. At 50% DMF coverage, the average H_2O adsorption is only 63.5% of that of pure Pt(111). Although 70% DMF coverage has only half the average H_2O adsorption time compared to pure Pt(111), its O_2 adsorption time also decreased. Together, a DMF coverage of 50% represents the optimal coverage for both O_2 and H_2O dynamics from MD simulations and analyses. The decrease of average H_2O adsorption time is attributed to the broken water adlayer (less H-bonds), which facilitates fast water exchange at the catalyst electrolyte interface.

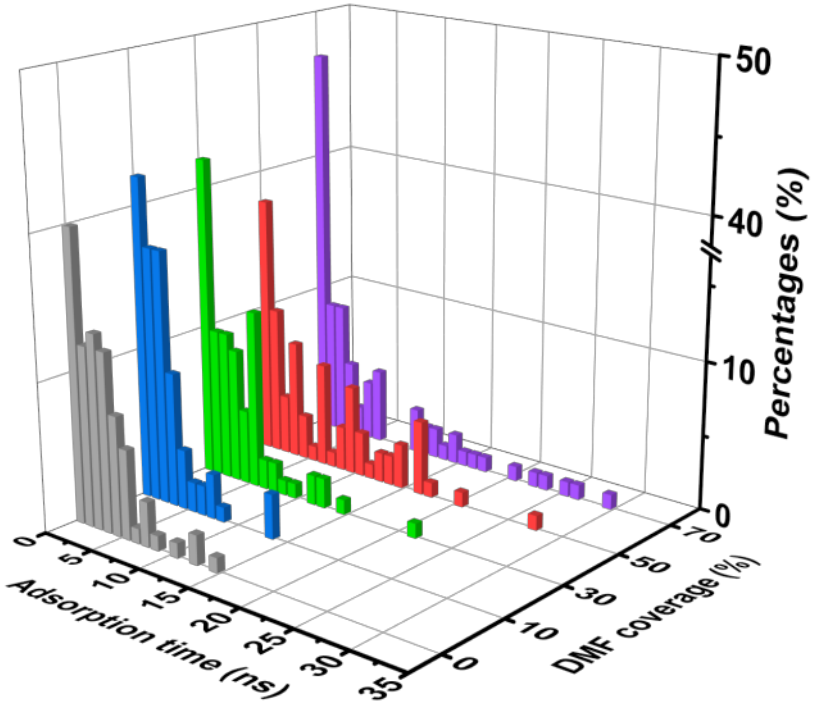

Figure. 5.8. Statistical analyses of adsorption time distribution for O_2 at different DMF coverages. The Y-axis represents the percentage of O_2 molecules at each adsorption time. With the increase of DMF coverage, the adsorption time distribution broadens from 0-15 ns to 0-30 ns, meaning DMF allows more O_2 molecules to adsorb a longer time on Pt(111) surface. However, when the coverage reaches 70%, though it has the broadest adsorption time distribution, about half O_2 molecules (highest percentage compared to other counterparts) do not adsorb to Pt surface. Therefore, an optimal DMF coverage (50%) exists for the best average O_2 adsorption time.

In our MD simulations, the pure Pt(111) surface and Pt(111) surface with 50% DMF coverage (Figure 5.6b and c) showed the highest O_2 concentration and the longest O_2 adsorption time, representing a higher probability to improve the ORR kinetics. Therefore, we focused on two groups (0% DMF coverage vs. 50% DMF coverage) and analyzed the adsorption free energy profiles of oxygen molecules using steered molecular dynamics (SMD) (Figure 5.6d, 5.9, 5.10). The energy barriers arise from the simultaneous breaking of hydrogen bonds and the replacement of interior water molecules when bulky O_2 molecules enter interfacial regions (the adlayer and second water layers). Interestingly, Pt(111)-50% DMF with imcomplete water network integrity showed lower free energies than that for pure Pt(111). Specifically, the peak at a distance of ~2.7 Å from Pt(111) surface represented the contact of O_2 to Pt surface, where the adsorption free energies were calculated to be -0.65 and -0.23 kcal/mol for pure Pt(111) and Pt(111)-50% DMF, respectively. Such high-resolution free energy variation displayed the precise thermodynamics of O_2 adsorption affected by DMF at the complicated catalyst-electrolyte interface (Figure 5.6e). The results above suggested surface adsorbed DMF can lower the energy barrier of O_2 adsorption, hence changing the transport properties of interfacial O_2.

Note that the interfacial O_2 concentration and average O_2 adsorption time decreased when DMF coverage reached 70%, which is due to significantly reduced available surface sites for O_2 molecules. For example, although some of the O_2 molecules have a much longer adsorption time (> 20 ns), 47% of them never had a chance to access the Pt(111) surface (Figure 5.8). As a result,

the average O_2 adsorption time of 70% DMF coverage is lower than the counterpart for 50% DMF coverage.

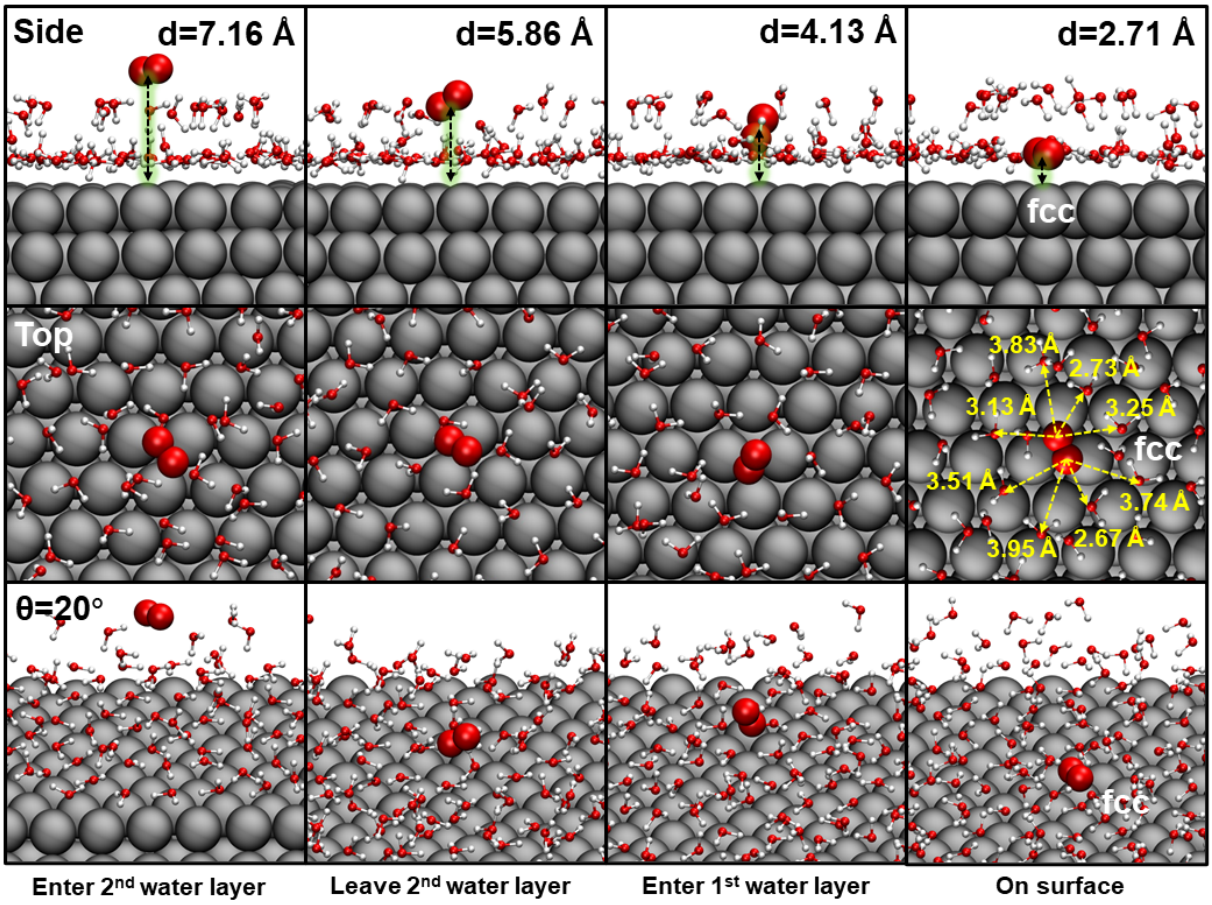

Figure 5.9. Side, top, and θ = 20° views of surface configuration for pure Pt(111) at different status during the steered molecular dynamics (SMD) simulations. The O_2 molecule is approaching the Pt(111) surface from the Z-direction with a speed of 0.03 Å/ns. The d values in the side views represent the distance from the O_2 molecule center to the Pt(111) surface atom. The evolutionary process indicates the O_2 molecule penetrating the water layers and finally adsorbing on the Pt(111) surface. It is notable that when eventually the O_2 molecule adsorbs on the Pt(111) surface, it tends to bind at the fcc site (top views), which is well acknowledged. Moreover, the adsorbed O_2 molecule is surrounded by densely hydrogen bonded adlayer water molecules with an average distance of 3.35 Å. The dense hydrogen bonded water network leads to higher free energy of O_2 penetration and adsorption.

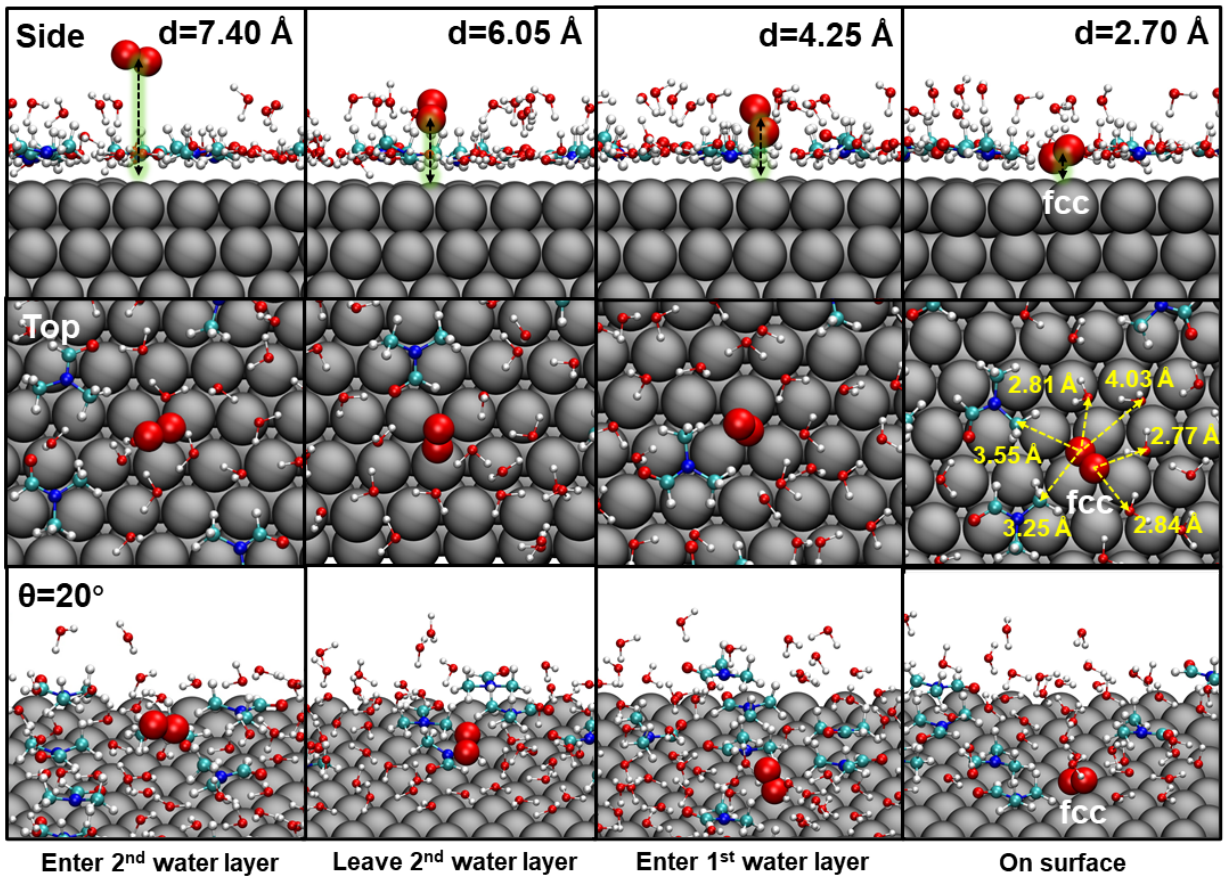

Figure 5.10. Side, top, and θ = 20° views of surface configuration for Pt(111) with 50% DMF coverage at different status during the SMD simulations. The O_2 molecule is approaching the Pt(111) surface from the Z-direction with a speed of 0.03 Å/ns. The d values in the side views represent the distance from the O_2 molecule center to the Pt(111) surface atom. The evolutionary process indicates the O_2 molecule penetrating the water layers and finally adsorbing on the Pt(111) surface. Herein, the DMF disrupts the dense water layers within the interfacial layer, especially the adlayer. The adsorbed O_2 molecule tends to bind at the fcc site (top views), which is also close to the methyl groups of DMF. The surrounding water molecules reduce to 6 with an average distance of 3.21 Å, and the H-bonding network is broken by DMF. This correlates to the lower free energy of O_2 penetration and adsorption. This stresses again the role of DMF can modulate the kinetics adsorption of O_2 and H_2O molecules, lowering the O_2 adsorption energy barrier and accelerating the electrolyte exchange dynamics.

The above experimental results and MD simulations analysis suggested that proper surface modification of the Pt can lead to enhanced local O_2 concentration and improved ORR activity. One should note that the surface modification approach works independently from other activity enhancement strategies such as strain effects and ligand effects. Therefore, all these effects can

cumulatively enhance the SA of Pt-alloy catalysts. Take a step further, we prepared the PtCuNi catalyst using a modified method reported previously[26] and applied the surface modification following the same procedure as Pt/C catalysts. High-angle annular dark-field scanning transmission electron microscopy (HAADF-STEM) showed that PtCuNi catalysts possessed mainly tetrahedral shapes with an average edge length of 5.8 ± 1.1 nm (Figure 5.11a, b). The lattice spacings were 0.217 nm based on the fast Fourier transform (FFT) diffraction pattern, corresponding to (111) facet (inset of Figure 5.11c) and energy dispersion X-ray spectroscopy (EDX) elemental analysis ($Pt_{58}Cu_{29}Ni_{13}$) (Figure 5.11d). The EDS elemental mapping results showed that PtCuNi catalysts possessed the Cu-rich core and PtNi shell (Figure 5.11e), consistent with our previous report[26]. For comparison, we also characterized surface-modified PtCuNi catalysts at 24 hours of modification that showed the most significant improvement. The tetrahedral morphology remained unchanged during the modification process (Figure 5.12a) with an average edge length of 5.9 ± 1.3 nm (Figure 5.12b), comparable to that of original PtCuNi catalysts. The (111) lattice spacing remained 0.217 nm according to the FFT diffraction pattern (inset of Figure 5.12d), suggesting no obvious lattice contraction or expansion. The composition remained essentially the same before ($Pt_{58}Cu_{29}Ni_{13}$) and after ($Pt_{57}Cu_{30}Ni_{13}$) modification (Figure 5.12c), and corresponding elemental distributions within PtCuNi (Figure 5.12e) did not show obvious change. Similar to Pt/C, the ECSA of surface-modified PtCuNi catalysts decreased from 70 m^2/g_{Pt} to 49 m^2/g_{Pt} after 24 hours of modification and further decreased to 36 m^2/g_{Pt} after 48 hours of modification (Fig. 4a and Figure 5.13a). As expected, XPS results for catalysts after the activation process showed that the concentration of N-containing species increased with modification time, consistent with the trend of surface DMF coverage (Figure 5.13b), whereas the 4f 7/2 peak of Pt didn't shift (Figure 5.14) and the increasing concentration of Pt^{2+} and Pt^{4+} after

activation may associate with more surface adsorbed O_2. We also compared the morphology, size, composition, and structures for catalysts after the activation process, which showed a nuanced difference for original PtCuNi catalysts and surface-modified PtCuNi catalysts (Figure 5.15, 16).

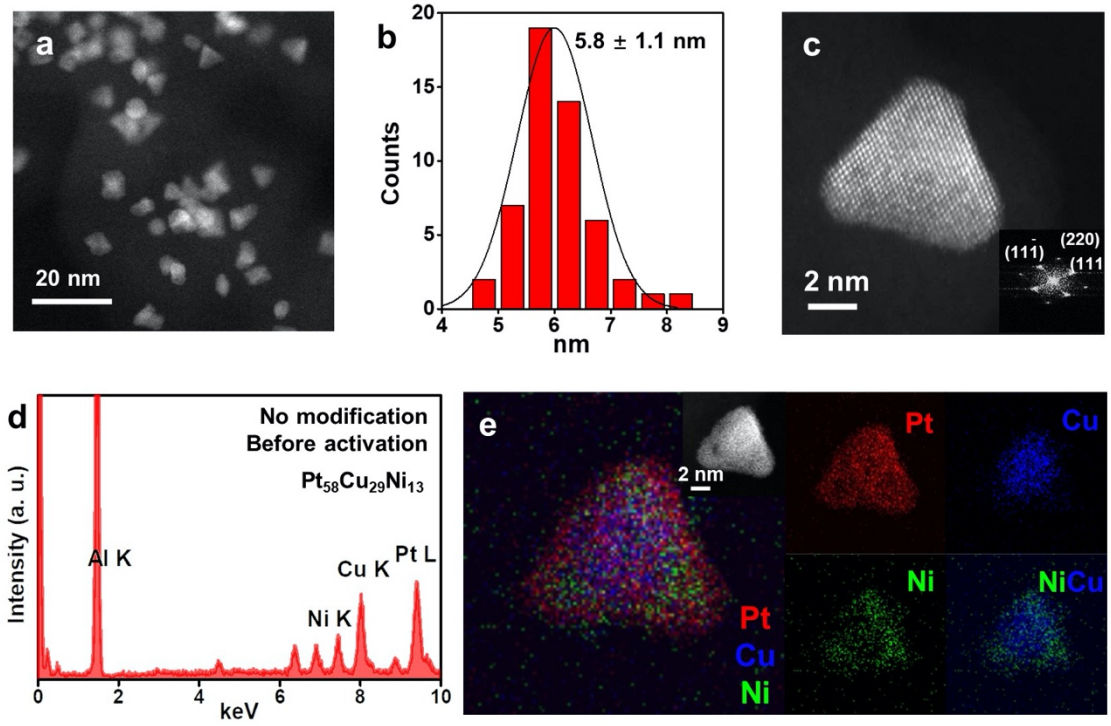

Figure 5.11. Characterizations of original as-prepared PtCuNi catalysts. (**a**) Low-magnification STEM image of original as-prepared PtCuNi catalysts loaded on carbon black. (**b**) Size distribution of original as-prepared PtCuNi catalysts measured according to the edge of tetrahedral shaped PtCuNi catalysts. (**c**) Atomic high-resolution HAADF-STEM image of as-prepared PtCuNi catalysts. (**d**) Representative EDX composition analysis of original as-prepared PtCuNi catalysts. (**e**) EDX mapping results of as-prepared PtCuNi catalysts, showing a Cu-rich core and PtNi shell.

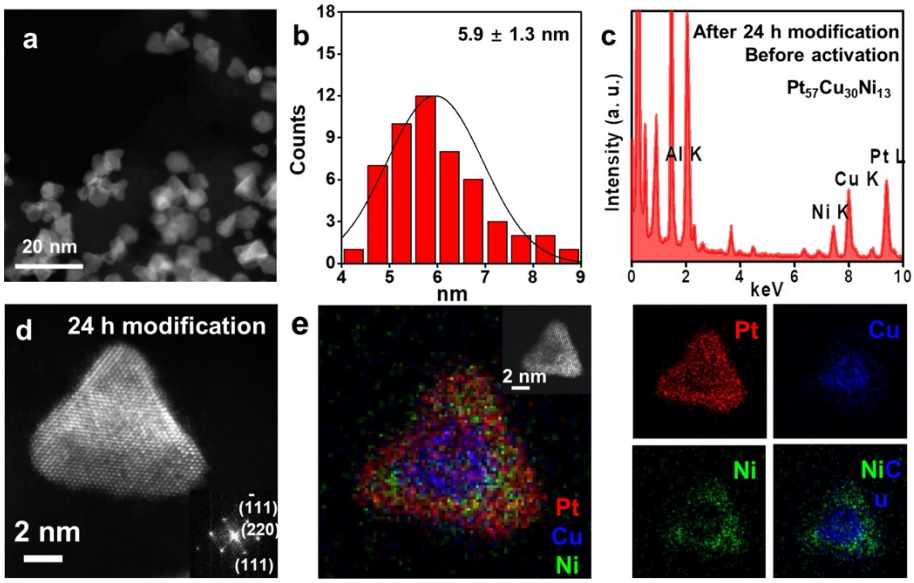

Figure 5.12. Characterizations of surface-modified PtCuNi catalysts modified for 24 hours in DMF. (**a**) Low-magnification STEM image of surface-modified PtCuNi catalysts loaded on carbon black. (**b**) Size distribution of surface-modified PtCuNi catalysts measured according to the edge of tetrahedral shaped PtCuNi catalysts. (**c**) Representative EDX composition analysis of surface-modified PtCuNi catalysts. (**d**) High-resolution atomic STEM image of surface-modified Petunia catalyst. (e) Representative EDX elemental mapping results of surface-modified PtCuNi catalysts, suggesting no obvious elemental distribution change.

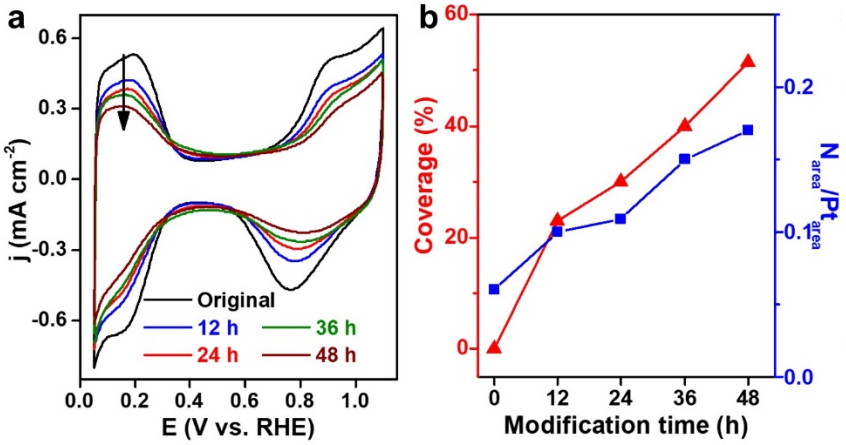

Figure 5.13. Electrochemical measurements of PtCuNi catalysts. (**a**) CV comparison of PtCuNi catalysts at different modification time: original (black), 12 hours modification time (blue), 36 hours modification time (green), 48 hours modification time (wine). (**b**) The relationship between surface DMF coverage (left Y-axis) or relative N/Pt ratio (right Y-axis, derived from XPS) and modification time.

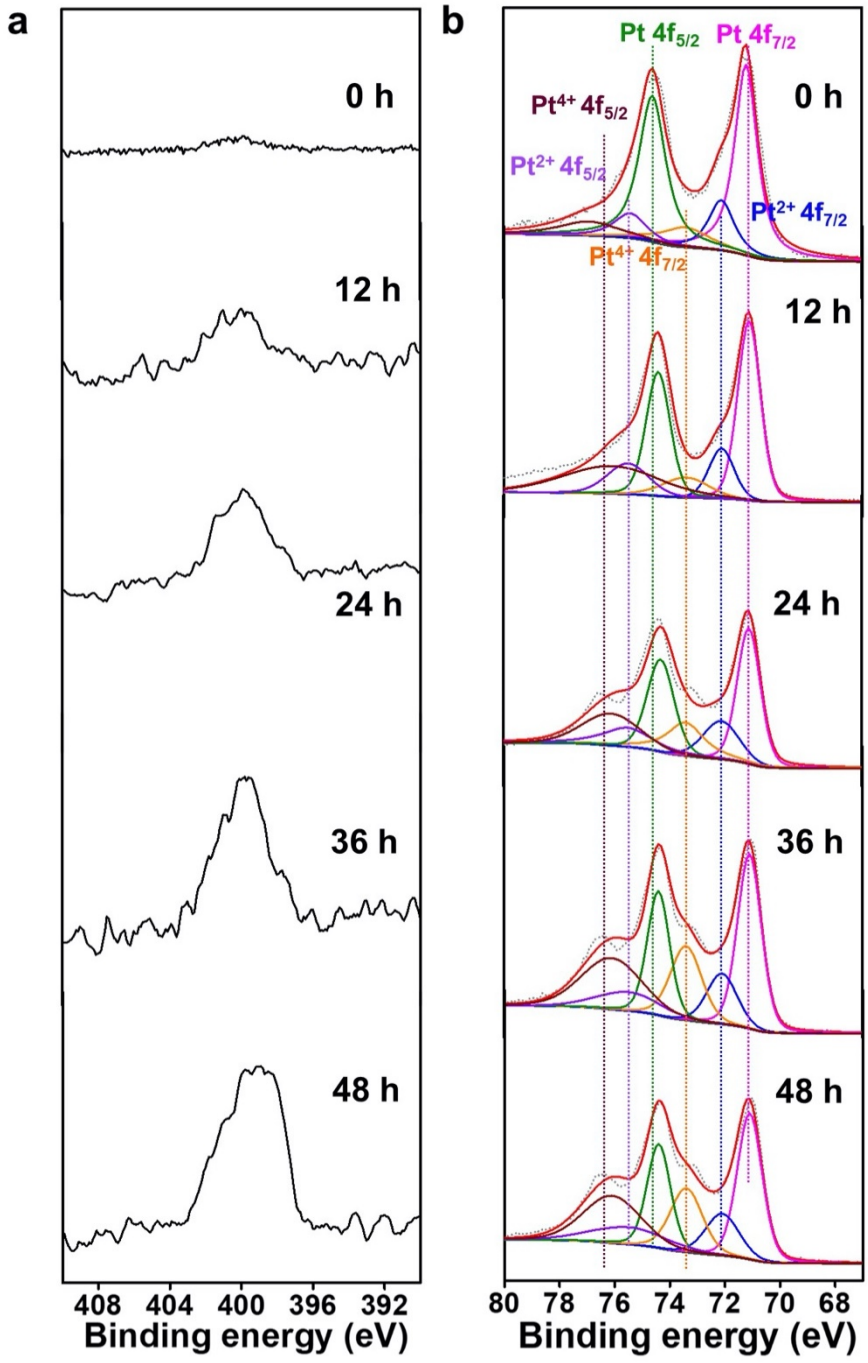

Figure 5.14. (**a**) XPS N 1s spectra of PtCuNi catalysts and (**b**) XPS Pt 4f spectra of PtCuNi catalysts at different modification time.

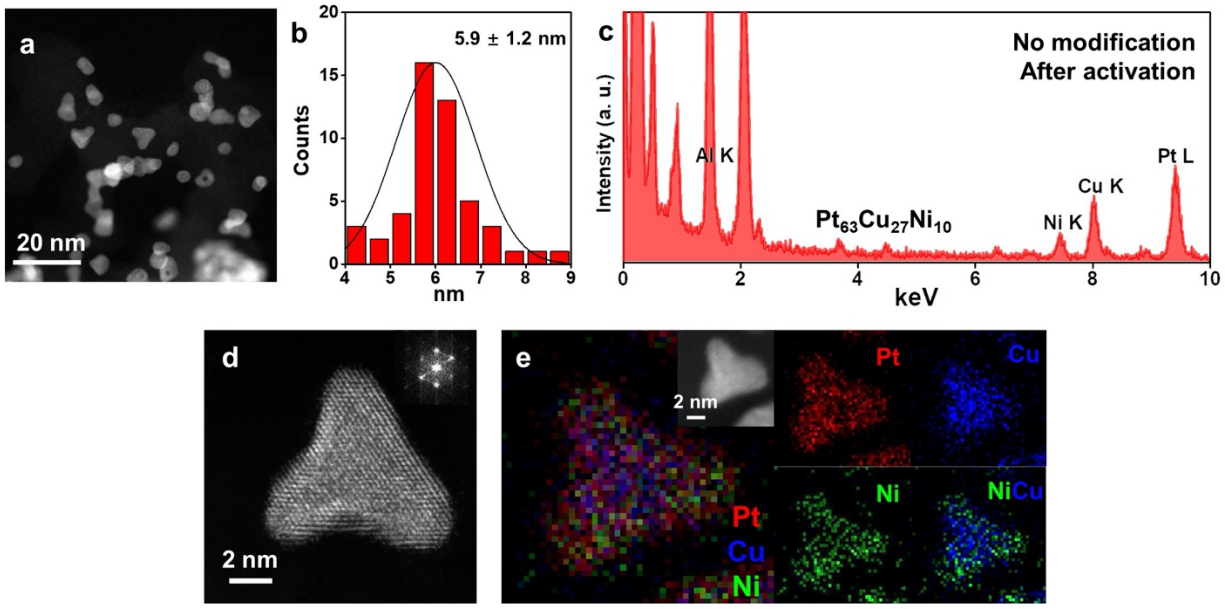

Figure 5.15. Characterizations of original PtCuNi catalysts after activation. (**a**) Low-magnification STEM image of original PtCuNi catalysts after activation. (**b**) Size distribution of original PtCuNi catalysts after activation measured according to the edge of tetrahedral shaped PtCuNi catalysts. (**c**) Representative EDX composition analysis of original PtCuNi catalysts after activation. (**d**) Atomic high-resolution HAADF-STEM image of original PtCuNi catalysts after activation. (**e**) EDX mapping results of original PtCuNi catalysts after activation.

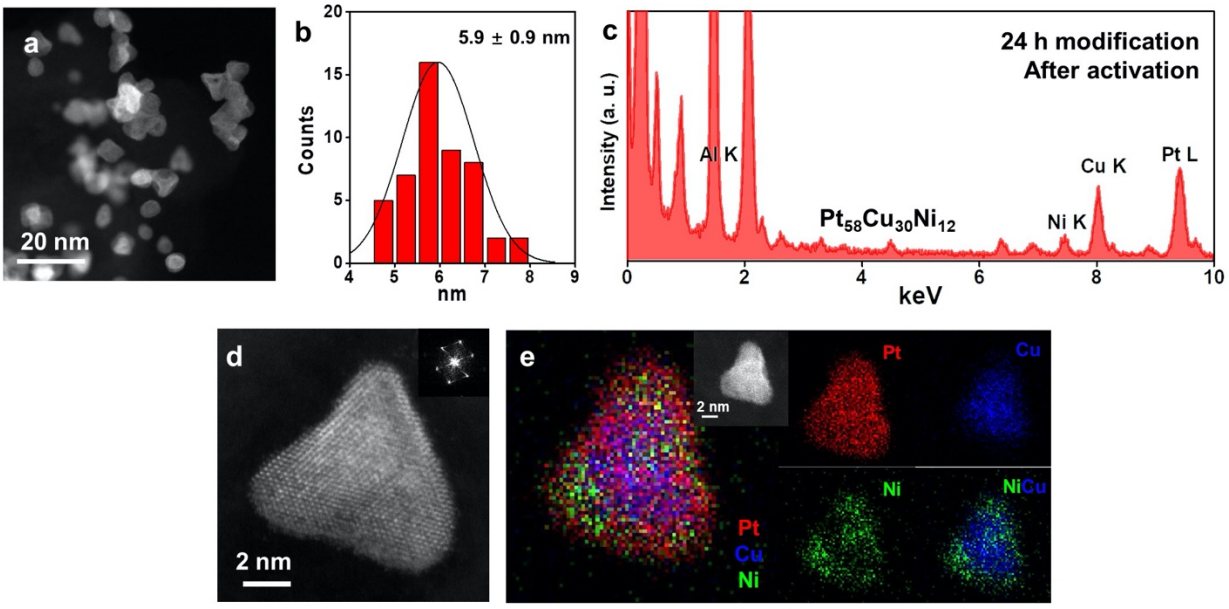

Figure 5.16. Characterizations of surface-modified PtCuNi catalysts after activation. (**a**) Low-magnification STEM image of surface-modified PtCuNi catalysts after activation. (**b**) Size

distribution of surface-modified PtCuNi catalysts after activation measured according to the edge of tetrahedral shaped PtCuNi catalysts. (**c**) Representative EDX composition analysis of surface-modified PtCuNi catalysts after activation. (**d**) Atomic high-resolution HAADF-STEM image of surface-modified PtCuNi catalysts after activation. (**e**) EDX mapping results of surface-modified PtCuNi catalysts after activation.

We further evaluated the ORR activity of surface-modified PtCuNi catalysts. Our experiments suggested an optimal modification time of 24 hours brings the best activity improvement for PtCuNi catalysts, which is the same for commercial Pt/C catalysts. Similarly, both the SA and MA increased and then declined with modification time (Figure 5.17a). The optimal surface-modified PtCuNi catalysts exhibited an unprecedented high SA of 21.8 ± 2.1 mA/cm^2 and an ultrahigh MA of 10.7 ± 1.1 A/mg$_{Pt}$ at 0.9 V versus RHE (Figure 5.17a), which are about 2.6 times and 1.9 times those of original PtCuNi catalysts (8.2 ± 0.4 mA/cm^2 and 5.7 ± 0.3 A/mg$_{Pt}$) and 45.4 and 46.5 times those of Pt/C catalysts (0.48 mA/cm^2 and 0.23 A/mg$_{Pt}$), respectively. The SA of our surface-modified PtCuNi catalysts outperforms all current state-of-the-art catalysts and nearly doubled the previous record (Figure 5.17b and Table 5. 1).

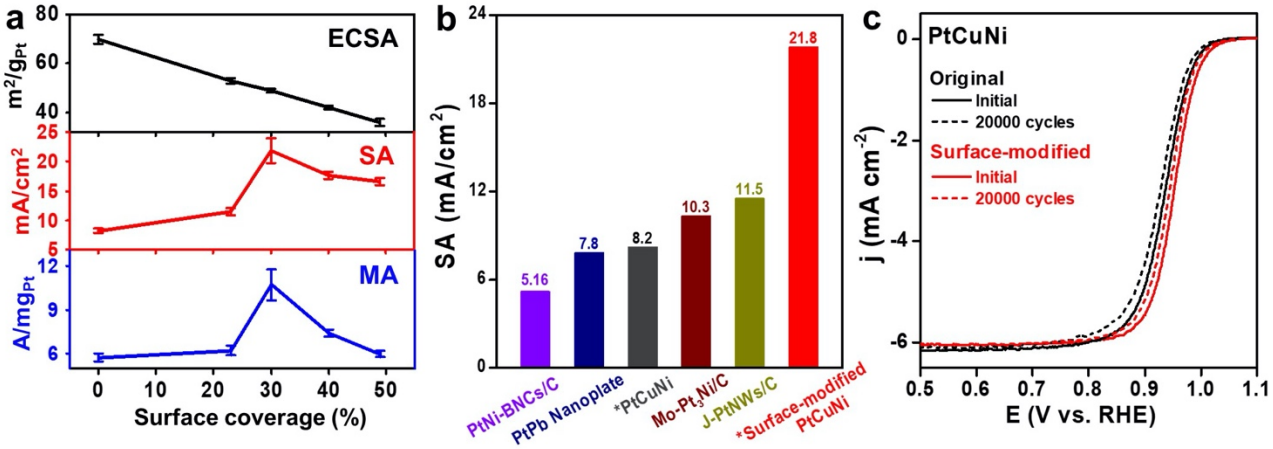

Figure 5.17. Performance of surface-modified PtCuNi catalysts. (**a**) The evolution of ECSA (black), SA (red), and MA (blue) with DMF surface coverage. (**b**) Comparison of SA for optimal surface-modified PtCuNi catalysts and state-of-the-art ORR catalysts. References: PtNi-BNCs/C[38], PtPt Nanoplate[39], Mo-Pt$_3$Ni/C[40], J-PtNWs[41]. *PtCuNi and *Surface-modified PtCuNi catalysts are from this work. (**c**) ORR stability LSV curves for original PtCuNi catalysts (black) and optimal

surface-modified PtCuNi catalysts (red) before (black solid line and red solid line) and after (black dashed line and red dashed line) 20,000 cycles.

We further carried out 20,000 cycles of accelerated degradation test (ADT) for optimal surface-modified PtCuNi catalysts and original PtCuNi catalysts and performed postmortem characterizations (Figures 5.18-20). After ADT, the surface-modified PtCuNi catalysts still showed a respectable SA and MA of 12.3 mA/cm^2 and 6.6 A/mg_{Pt}, respectively (Figures 5.17c and Table 5.1), exceeding the initial performance of original PtCuNi catalysts. Interestingly, despite similar size after ADT (Figure 5.20), the ECSA retentions of two group PtCuNi catalysts showed a dramatic difference (Figures 5.18). In specific, Surface-modified PtCuNi catalyst showed an ECSA retention of 123%, which was much higher than that of original PtCuNi catalysts (93%). This may associate with the partial stripping of the surface molecule (DMF) during long-term ADT cycling, exposing more available Pt surface. Indeed, a less extent of surface coverage can still provide considerable activity enhancement towards ORR, justifying their higher activity than original PtCuNi catalysts after ADT. Therefore, more cycles are required to strip surface molecules while the activity can be well retained above the initial activity of the original catalyst. We thus advocate that surface molecule can effectively extend the lifetime of catalysts.

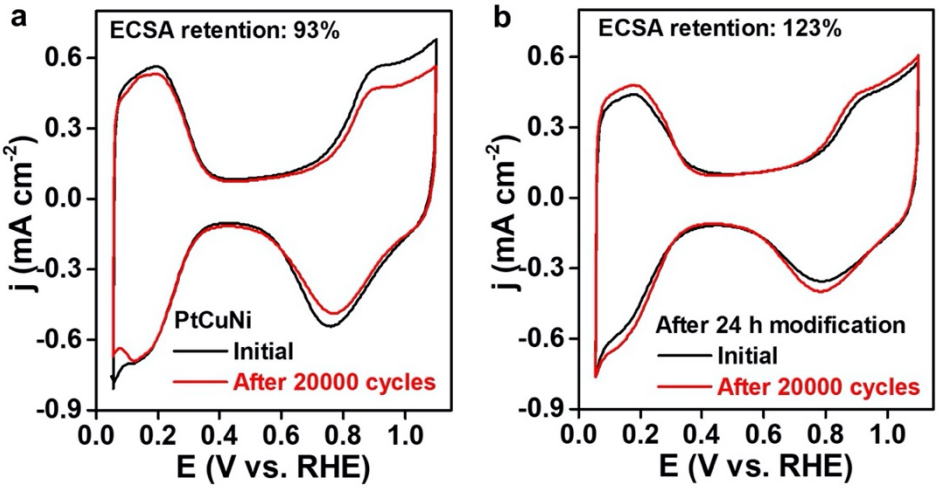

Figure 5.18 Comparison of ECSA change of original PtCuNi catalysts (left) and suface-modified PtCuNi catalysts (right). (**a**) CV comparison of original PtCuNi catalysts before (black) and after (red), showing 7% loss of ECSA after 20,000 cycles. (**b**) CV comparison of surface-modified PtCuNi catalysts before (black) and after (red), showing a 23% increase of ECSA after 20,000 cycles.

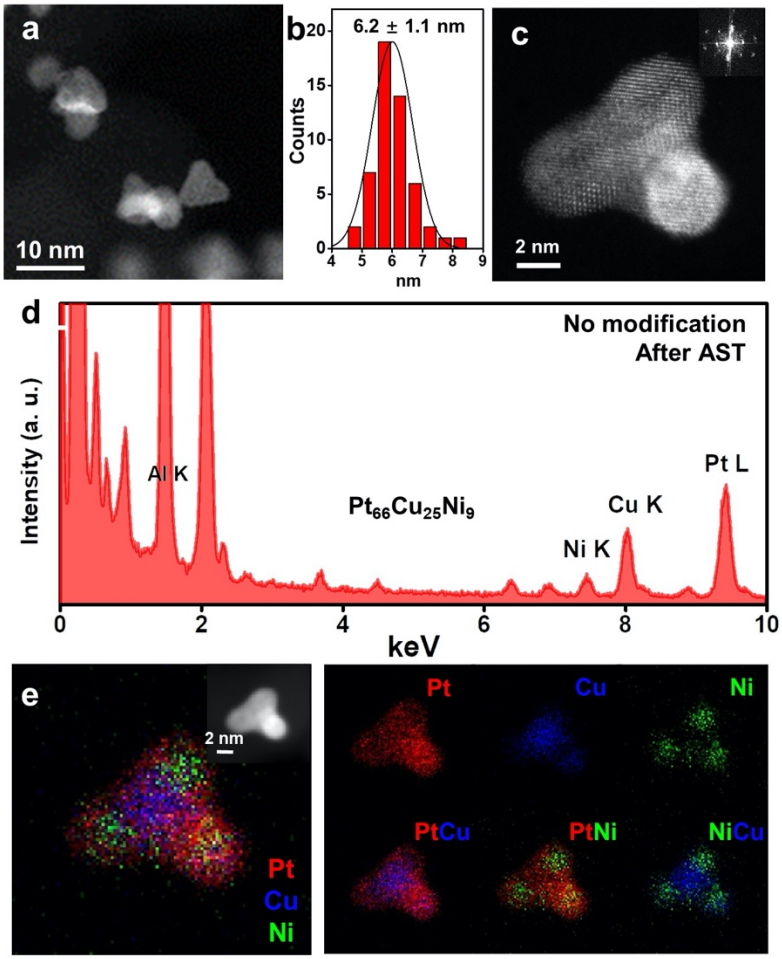

Figure 5.19 Characterizations of original PtCuNi catalysts after ADT. (**a**) Low-magnification STEM image of original PtCuNi catalysts after ADT. (**b**) Size distribution of original PtCuNi catalysts after ADT measured according to the edge of tetrahedral shaped PtCuNi catalysts. (**c**) Atomic high-resolution HAADF-STEM image of original PtCuNi catalysts after activation. (**d**) Representative EDX composition analysis of original PtCuNi catalysts after ADT. (**e**) EDX mapping results of original PtCuNi catalysts after activation.

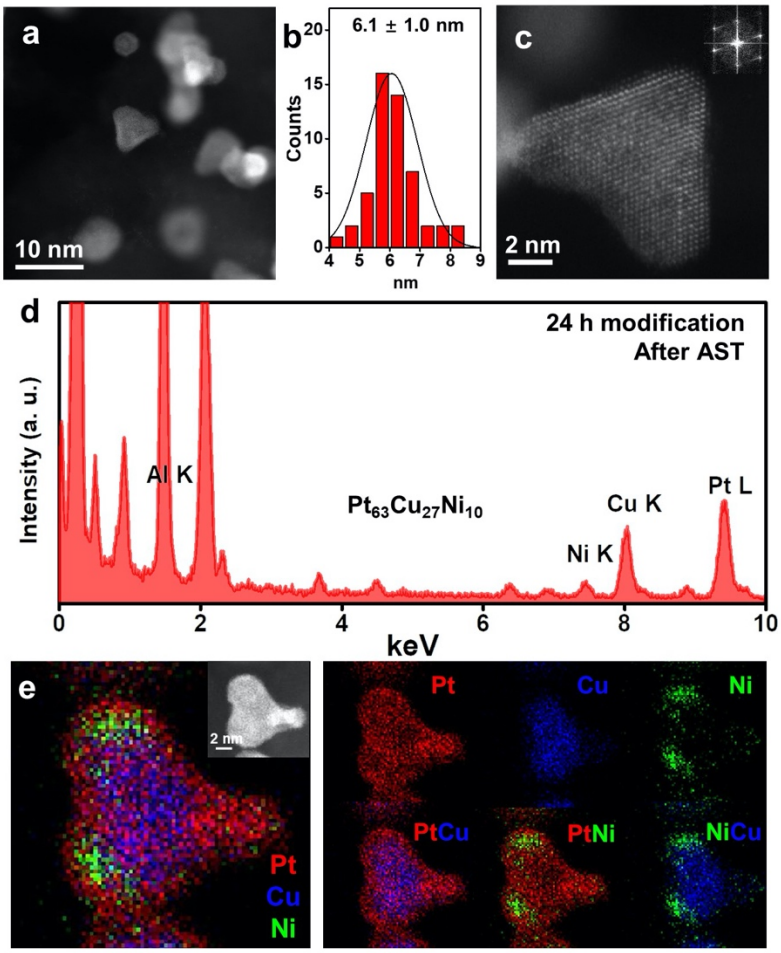

Figure 5.20 Characterizations of surface-modified PtCuNi catalysts after ADT. (**a**) Low-magnification STEM image of surface-modified PtCuNi catalysts after ADT. (**b**) Size distribution of surface-modified PtCuNi catalysts after ADT measured according to the edge of tetrahedral shaped PtCuNi catalysts. (**c**) Atomic high-resolution HAADF-STEM image of surface-modified PtCuNi catalysts after ADT. (**d**) Representative EDX composition analysis of surface-modified PtCuNi catalysts after ADT. (**e**) EDX mapping results of surface-modified PtCuNi catalysts after ADT.

Table 5.1 RDEs performance of surface-modified PtCuNi catalysts, in comparison to those in several representative works. BOL: beginning of life, EOL: end of life, NA, not applicable.

Catalyst	SA (mA/cm²)		MA (A/mg)		ECSA (m²/g)	ADT cycles
	BOL	ADT	BOL	ADT		
Surface-modified PtCuNi	**21.8**	**12.3**	**10.7**	**6.6**	**49**	**20,000**
As-prepared PtCuNi	8.2	5.3	5.7	4.1	70	20,000
Pt_3Ni nanoframe[42]	8.4*	NA	5.7	NA	67.2	10,000

PtNi-BNCs/C[38]	5.16	5.15*	3.52	3.47	68.2	50,000
fct-Pt-Co@Pt octahedron[43]	9.16	7.21	2.82	2.23	30.8	30,000
PtPb nanoplate[39]	7.8	7.0	4.3	3.97	55.0	50,000
PtNi/Ni–B/C[44]	9.05	NA	5.3	NA	59	5,000
J-PtNWs[41]	11.5	10.9*	13.6	12.0	118	6,000

5.4 Conclusion

In summary, we developed a facile, universal, and controllable surface modification approach using DMF to improve the activity and lifetime of ORR Pt-based electrocatalysts. By combining experimental results and MD simulations, we proposed that DMF can significantly increase interfacial O_2 concentration, average O_2 adsorption time, and facilitate water removal. The optimal surface-modified PtCuNi catalysts exhibited a record-high SA with an extended catalyst lifetime. This work provides a rational pathway to tailor the interfacial properties of catalysts and provides an in-depth understanding of catalyst-electrolyte interfaces.

5.5 References

1. Wu, J. & Yang, H. Platinum-based oxygen reduction electrocatalysts. *Acc. Chem. Res.* **46**, 1848-1857 (2013).

2. Zhao, Z. *et al.* Pt-based nanocrystal for electrocatalytic oxygen reduction. *Adv. Mater.* **31**, 1808115 (2019).

3. Stamenkovic, V. R. *et al.* Improved oxygen reduction activity on $Pt_3Ni(111)$ via increased surface site availability. *Science* **315**, 493 (2007).

4. Strasser, P. *et al.* Lattice-strain control of the activity in dealloyed core–shell fuel cell catalysts. *Nat. Chem.* **2**, 454-460 (2010).

5. Cui, C., Gan, L., Heggen, M., Rudi, S. & Strasser, P. Compositional segregation in shaped Pt alloy nanoparticles and their structural behaviour during electrocatalysis. *Nat. Mater.* **12**, 765-771 (2013).

6. Chung, D. Y. *et al.* Highly durable and active PtFe nanocatalyst for electrochemical oxygen reduction reaction. *J. Am. Chem. Soc.* **137**, 15478-15485 (2015).

7. Li, J. *et al.* Hard-magnet $L1_0$-CoPt nanoparticles advance fuel cell catalysis. *Joule* **3**, 124-135 (2019).

8. Han, B. *et al.* Record activity and stability of dealloyed bimetallic catalysts for proton exchange membrane fuel cells. *Energy Environ. Sci.* **8**, 258-266 (2015).

9. Nørskov, J. K. *et al.* Origin of the overpotential for oxygen reduction at a fuel-cell cathode. *J. Phys. Chem. B* **108**, 17886-17892 (2004).

10. Escudero-Escribano, M. *et al.* Tuning the activity of Pt alloy electrocatalysts by means of the lanthanide contraction. *Science* **352**, 73-76 (2016).

11. Stamenkovic, V. *et al.* Changing the activity of electrocatalysts for oxygen reduction by tuning the surface electronic structure. *Angew. Chem. Int. Ed.* **45**, 2897-2901 (2006).

12. Debe, M. K. Electrocatalyst approaches and challenges for automotive fuel cells. *Nature* **486**, 43-51 (2012).

13. Allen, J. B. & Larry, R. F. *Electrochemical methods fundamentals and applications*. (John Wiley & Sons, 2001).

14. Benn, E., Uvegi, H. & Erlebacher, J. Characterization of nanoporous metal-ionic liquid composites for the electrochemical oxygen reduction reaction. *J. Electrochem. Soc.* **162**, H759-H766 (2015).

15. Snyder, J., Fujita, T., Chen, M. W. & Erlebacher, J. Oxygen reduction in nanoporous metal–ionic liquid composite electrocatalysts. *Nat. Mater.* **9**, 904-907 (2010).

16. Favero, S., Stephens, I. E. L. & Titirici, M. M. Engineering the electrochemical interface of oxygen reduction electrocatalysts with ionic liquids: a review. *Adv. Energy Sustainability Res.* **2**, 2000062 (2021).

17. Gonella, G. *et al.* Water at charged interfaces. *Nat. Rev. Chem.* **5**, 466-485 (2021).

18. Steinmann, S. N. & Seh, Z. W. Understanding electrified interfaces. *Nat. Rev. Mater.* **6**, 289-291 (2021).

19. Subbaraman, R. *et al.* Trends in activity for the water electrolyser reactions on 3d M(Ni,Co,Fe,Mn) hydr(oxy)oxide catalysts. *Nat. Mater.* **11**, 550-557 (2012).

20. Intikhab, S. *et al.* Caffeinated interfaces enhance alkaline hydrogen electrocatalysis. *ACS Catal.* **10**, 6798-6802 (2020).

21. Chen, G. *et al.* Interfacial electronic effects control the reaction selectivity of platinum catalysts. *Nat. Mater.* **15**, 564-569 (2016).

22. Strmcnik, D. *et al.* The role of non-covalent interactions in electrocatalytic fuel-cell reactions on platinum. *Nature Chemistry* **1**, 466-472 (2009).

23. Lu, L. *et al.* Ligand-mediated bifunctional catalysis for enhanced oxygen reduction and methanol oxidation tolerance in fuel cells. *J. Mater. Chem. A* **6**, 18884-18890 (2018).

24. Zorko, M. *et al.* Improved rate for the oxygen reduction reaction in a sulfuric acid electrolyte using a Pt(111) surface modified with melamine. *ACS Appl. Mater. Interfaces* **13**, 3369-3376 (2021).

25. Kumeda, T., Hoshi, N. & Nakamura, M. Effect of Hydrophobic Cations on the Inhibitors for the Oxygen Reduction Reaction on Anions and Ionomers Adsorbed on Single-Crystal Pt Electrodes. *ACS Appl. Mater. Interfaces* **13**, 15866-15871 (2021).

26. Huang, J. *et al.* PtCuNi tetrahedra catalysts with tailored surfaces for efficient alcohol oxidation. *Nano Lett.* **19**, 5431-5436 (2019).

27. Dassault Systèmes BIOVIA, Materials Studio, v7.0.200, San Diego: Dassault Systèmes, 2013.

28. Phillips, J. C. *et al.* Scalable molecular dynamics with NAMD. *J. Comput. Chem.* **26**, 1781-1802 (2005).

29. Heinz, H., Lin, T.-J., Kishore Mishra, R. & Emami, F. S. Thermodynamically consistent force fields for the assembly of inorganic, organic, and biological nanostructures: The INTERFACE Force Field. *Langmuir* **29**, 1754-1765 (2013).

30. Heinz, H., Vaia, R. A., Farmer, B. L. & Naik, R. R. Accurate simulation of surfaces and interfaces of face-centered cubic metals using 12−6 and 9−6 Lennard-Jones potentials. *J. Phys. Chem. C* **112**, 17281-17290 (2008).

31. Zhu, E. *et al.* Enhancement of oxygen reduction reaction activity by grain boundaries in platinum nanostructures. *Nano Res.* **13**, 3310-3314 (2020).

32. Michaud-Agrawal, N., Denning, E. J., Woolf, T. B. & Beckstein, O. MDAnalysis: A toolkit for the analysis of molecular dynamics simulations. *J. Comput. Chem.* **32**, 2319-2327 (2011).

33. Richard J. Gowersk, M. L., Jonathan Barnoud, Tyler J. E. Reddy, Manuel N. Melo, Sean L. Seyler, Jan Domański, David L. Dotson, Sébastien Buchoux, Ian M. Kenney, Oliver Beckstein. MDAnalysis: A Python Package for the Rapid Analysis of Molecular Dynamics Simulations. *in Proceedings of the 15th Python in Science Conference. (SciPy Austin, TX, 2016), vol. 98.* (2016).

34. Plimpton, S. Fast parallel algorithms for short-range molecular dynamics. *J. Comput. Phys.* **117**, 1-19 (1995).

35. Fuchigami, T., Inagi, S. & Atobe, M. *Fundamentals and applications of organic electrochemistry: synthesis, materials, devices*. (2015).

36. Pegis, M. L., Wise, C. F., Martin, D. J. & Mayer, J. M. Oxygen reduction by homogeneous molecular catalysts and electrocatalysts. *Chem. Rev.* **118**, 2340-2391 (2018).

37. Wang, J. *et al.* Selective CO_2 electrochemical reduction enabled by a tricomponent copolymer modifier on a copper surface. *J. Am. Chem. Soc.* **143**, 2857-2865 (2021).

38. Tian, X. *et al.* Engineering bunched Pt-Ni alloy nanocages for efficient oxygen reduction in practical fuel cells. *Science* **366**, 850 (2019).

39. Bu, L. *et al.* Biaxially strained PtPb/Pt core/shell nanoplate boosts oxygen reduction catalysis. *Science* **354**, 1410 (2016).

40. Huang, X. *et al.* High-performance transition metal–doped Pt_3Ni octahedra for oxygen reduction reaction. *Science* **348**, 1230 (2015).

41. Li, M. *et al.* Ultrafine jagged platinum nanowires enable ultrahigh mass activity for the oxygen reduction reaction. *Science* **354**, 1414 (2016).

42. Chen, C. *et al.* Highly crystalline multimetallic nanoframes with three-dimensional electrocatalytic surfaces. *Science* **343**, 1339 (2014).

43. Xie, M. *et al.* Pt–Co@Pt octahedraln nanocrystals: enhancing their activity and durability toward oxygen reduction with an intermetallic core and an ultrathin shell. *J. Am. Chem. Soc.* **143**, 8509-8518 (2021).

44. He, D. *et al.* Amorphous nickel boride membrane on a platinum–nickel alloy surface for enhanced oxygen reduction reaction. *Nat. Commun.* **7**, 12362 (2016).

Chapter 6. Conclusion and Perspective

During my Ph.D. experience, I successfully design high-performance nanocatalysts for electrocatalytic reactions, including sd-Pt-alloy, tetra-PtCuNi alloy, PtCoNWs, etc. Based on these catalysts, by combining advanced characterization (XAS) and computational simulations, I successfully mapped out the experimental Sabatier plot for predictive design of highly active and stable Pt-alloy catalysts. Take a step further, I incorporated the above highly promising Pt-alloy catalysts into practical fuel cells, showing excellent performance. In specific, PtCoNWs showed a record-high MA and ultrahigh Pt utilization. Last but not the least, in addition to catalysts design, I found that tailoring the interfacial configuration can change the behavior and concentration of surface species, which can also lead to activity enhancement.

In the future, I will mainly focus on the following topics:

1. Because the ORR barrier or overpotential highly correlates with the scaling relation, it is highly desirable to break this scaling relation. For example, dual-site catalysis may offer a huge potential by splitting two rate-determining-steps into two different sites, therefore lowering the overall potential.
2. The interfacial configuration, especially in the practical fuel cell, is the center to improve the microkinetic of ORR. This part is equally important to the catalysts, yet rarely investigated. Therefore, more efforts are needed to understand the interfacial status in practical devices.
3. To understand the reaction or degradation process in a practical fuel cell, it is highly recommended to perform in-situ characterizations. For example, in-situ TEM can be a great tool to understand the degradation mechanism in fuel cell with elevated temperature and potential cycling in a certain amount of water/air.